POLITECNICO DI TORINO

Collegio di Ingegneria Meccanica, Aerospaziale e dell'Autoveicolo

Master of Science Course in Aerospace Engineering

Master of Science Thesis

Optimal Control of a Solar Sail for an Interplanetary Mission to an Asteroid

Politecnico di Torino

Supervisor:
Prof. Lorenzo Casalino

Candidate:
Elena Faustini

Luglio 2025

Abstract

Solar sailing is a non-traditional propulsion system that is attracting growing interest due to its various benefits compared with traditional chemical propulsion. A solar sail generates thrust through the momentum exchange resulting from the interaction between the sail surface and the incident solar radiation. This propulsion method provides continuous thrust without requiring any propellant consumption. These characteristics make solar sailing a viable option for long-duration missions. This thesis focuses on orbit optimization for an interplanetary mission targeting an asteroid, carried out with a solar sail-propelled CubeSat. The study of asteroids is a topic of interest in various fields. The ancient origin of these celestial bodies makes them an essential source of information on the history and formation of our Solar System, the origin of the Moon and the development of life on our planet. The various types of asteroids offer a great reservoir of rare materials, making them an interesting location for space mining. Regarding Near-Earth Asteroid (NEA), planetary defence is necessary against Potentially Hazardous Asteroids (PHA). The compact size and low mass of a CubeSat make it a good candidate for solar sail propulsion.

Trajectory optimization, for the heliocentric phase of the mission, is performed using an indirect mathematical method. The motion equations of the sail are obtained from the two-body problem, including the contribution of solar radiation pressure. The optimal control theory is applied to formulate the problem and the Pontryagin's Maximum Principle provides the optimal sail orientation at each point of the trajectory. The formulation of the problem results in a boundary value problem, which is solved using an indirect Newton-like mathematical method.

Numerical analyses are carried out for different asteroids demonstrating the feasibility of the mission.

Contents

List of Figures

List of Tables

List of Acronims

NASA National Aeronautics and Space Administration

JPL Jet Propulsion Laboratory

GRC Glenn Research Center

ISAS Institute of Space and Astronautical Science

IKAROS Interplanetary Kite-craft Accelerated by Radiation of the Sun

MSFC Marshall Space Flight Center

JAXA Japan Aerospace Exploration Agency

NEA Near-Earth Asteroid

SLS Space Launch System

ACS3 Advanced Composite Solar Sail System

COTS Commercial Off The Shelf

NLP Non Linear Programming

BVP Boundary Value Problem

ESA European Space Agency

IAU International Astronomical Union

PHA Potentially Hazardous Asteroids

MOID Minimum Orbit Intersection Distance

RAAN Right Ascension of the Ascending Node

BCE Before Common Era

UTC Coordinated Universal Time

JD Julian Day

MJD Modified Julian Day

TNO Trans Neptunian Objects

NEAR Near-Earth Asteroid Rendezvous

OSIRIS-REx Origins, Spectral Interpretation, Resource Identification, Security, Regolith Explorer

DART Double Asteroid Redirection Test

Chapter 1

Introduction

The growing interest in deep space exploration is leading the space industry to explore and research non-traditional propulsion systems. The limitations of traditional chemical propulsion, which depends on fuel consumption, have led to the development of alternative technologies. Among these, solar sailing represents an interesting option for long-duration missions.

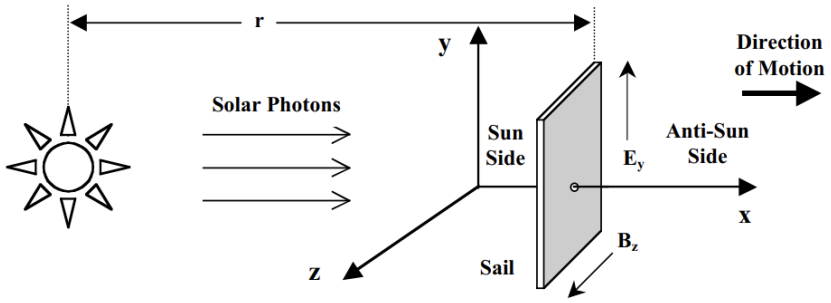

Figure 1.1: Solar sail model [1].

A solar sail is a large reflective surface of thin material, supported by a suitable structure, designed to interact with sunlight in order to generate thrust. Light is an electromagnetic radiation and is composed of particles called photons. A photon is an elementary particle, a quantum of the electromagnetic field, which has no mass and travels through space carrying momentum. When photons encounter a solar sail they they strike and reflect off it, as the sail surface is made of by a mirror-like material. The interaction between the sail and the particles results in a momentum transfer that pushes the sail, producing thrust. This continuous thrust can propel a spacecraft without the need for fuel, as illustrated in Figure 1.1. The resulting acceleration is small, but continuous, enabling missions that would otherwise be impractical with traditional propulsion. Assuming the sail is positioned directly facing the Sun, the sail will be pushed away (x-axis in figure). A solar sail can move in other directions by changing its orientation relative to the Sun. The physics underlying solar sail propulsion introduces new challenges in the trajectory optimization process compared to traditional methods.

This thesis focuses on the development of a code for the optimization of solar sail trajectories using an indirect method. Following a brief introduction to the concept of solar sail propulsion and the mission case study, the mathematical formulation of the indirect optimization approach is presented and the governing equations of motion for solar sail dynamics are derived. The implementation of the optimization algorithm is then discussed, followed by a presentation and analysis of the results.

1.1 History of solar sailing and key missions

The idea of utilizing something similar to a boat sail for propulsion in space dates back to 1610, when the German astronomer Johannes Kepler, in a letter addressed to Galileo Galilei, suggested to ”provide ships or sails adapted to the heavenly breezes”. This idea was inspired by the observation of comet tails being displaced by what he thought was a solar ”breeze” [2]. More than two centuries later, in 1865, Kepler’s idea gained a theoretical foundation when James Clerk Maxwell published his theory of electromagnetic fields and radiation. Maxwell demonstrated that photons, the fundamental constituents of sunlight, can carry energy and momentum which could be transferred to other objects, exerting a measurable pressure. The physics of this phenomenon was provided by Maxwell’s equations [3]. Subsequently, Konstantin Tsiolkovsky proposed the application of solar radiation pressure for spacecraft propulsion. In 1924, Maxwell’s theory was practically applied when Tsiolkovsky and Tsander wrote of ”using tremendous mirrors of very thin sheets” and ”using the pressure of sunlight to attain cosmic velocities” [4]. Several years passed, until 1964, for this technology to be named ”solar sailing”; the term was coined by Arthur C. Clarke, who proposed it in his science fiction story Sunjammer (The Wind From the Sun) [5]. In 1960 and in 1964, during Echo missions, two Mylar-coated balloons were launched into orbit by NASA to test how communications signals could be bounced across the country. The large, lightweight balloons were moved, allowing the measurement of the effects of solar pressure for the first time [3] [6].

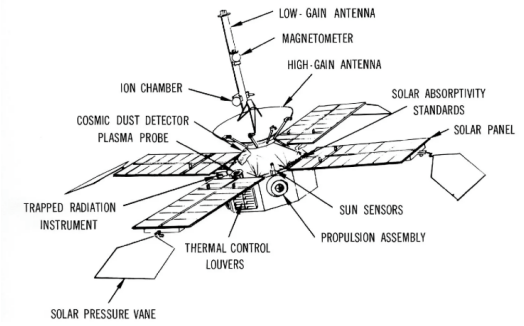

Figure 1.2: A diagram of early Mariner Mars spacecraft [7].

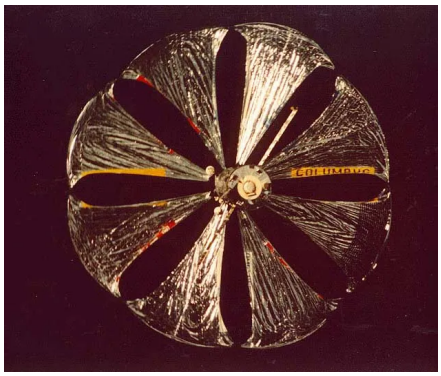

Figure 1.3: The Znamya 2 mirror-solar sail, deployed [8].

The first practical applications came with the Mariner 4 and Mariner 10 missions. Mariner 4 was equipped with four solar vanes that used sunlight pressure to stabilize the spacecraft Figure 1.2. In 1974, NASA used sailing techniques to manage the attitude control of Mariner 10. The orientation of the solar power panels relative to the Sun was controlled by ground operators, who were able to correct the spacecraft’s orientation [1].

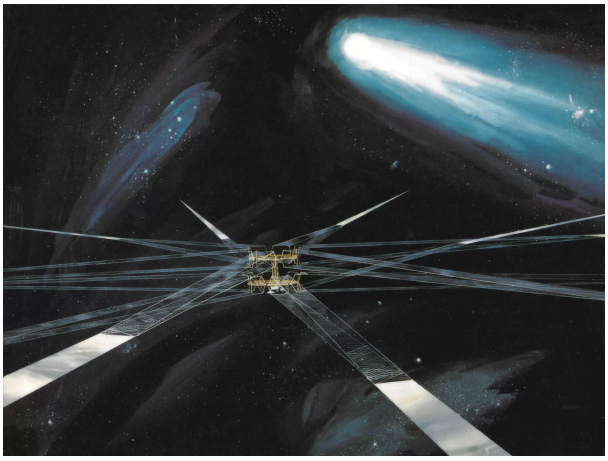

Figure 1.4: Heliogyro configuration concept, approaching the Halley's comet [3].

In 1975, NASA designed a solar sail that was supposed to rendezvous with the Halley's comet in 1986. The project, led by Dr. Louis Friedman and based on an idea by Jerome Wright, was not completed in time to achieve the rendezvous, but demonstrated the feasibility of the solar sailing technique for spacecraft propulsion. The sail was designed with a unique configuration, called heliogyro [Figure 1.4]: two ceiling fans stacked on top of each other, each equipped with six blades. As the fan spun, they provided the sail with increased stability [3]. In 1993, the first successful solar sail deployment was conducted by the Russian Space Agency. The sail, a 20-meter-diameter spinning mirror called Znamya 2 [Figure 1.3], aimed to beam solar power to the ground and was deployed from the end of the Russian Progress spacecraft . The mission verified the possibility of deploying the sail under the action of centrifugal forces and proved the feasibility of on-orbit deployment for large-scale flat structures. The project was discontinued in 1999, when the sail of the subsequent mission, Znamya 2.5, failed to deploy properly [6]. Between 2001 and 2005, NASA began working on solar sails and developed two 20 m x 20 m solar sail systems at Glenn Research Center (GRC) Space Power Facility [9]. The sails were the largest constructed by NASA and were tested on the ground in vacuum conditions, Figure 1.5.

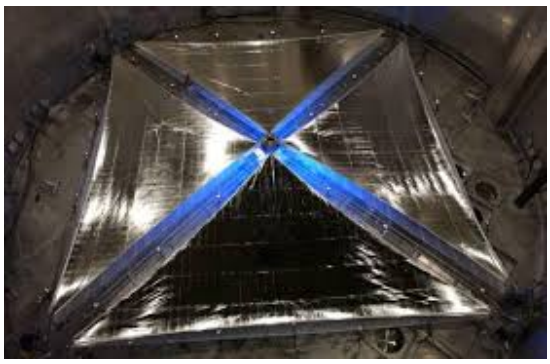

Figure 1.5: Solar sails tested at NASA's Plumbrook Station, deployed using rigid mechanical booms [10].

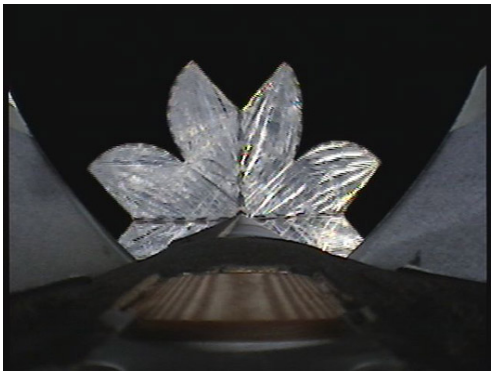

Figure 1.6: The deployment of clover type film taken by a camera onboard S-310 rocket [11].

In 2004, the Japanese Institute of Space and Astronautical Science (ISAS) successfully deployed two solar sail prototypes from a sounding rocket Figure 1.6. The objective of the experiment was to test the deployment mechanism, but not the propulsion capability [12].

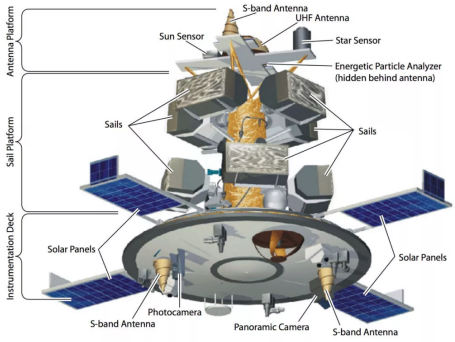

Figure 1.7: Cosmos 1 spacecraft [13].

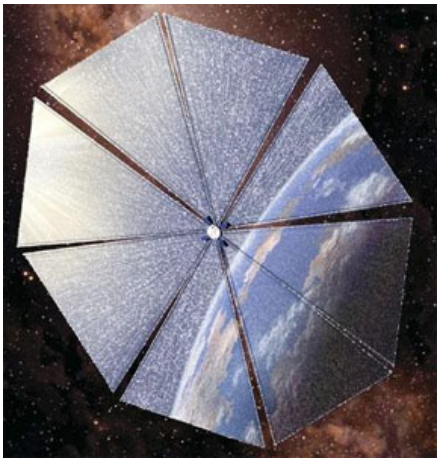

Figure 1.8: Cosmos 1 deployed sail [14].

Meanwhile the Planetary Society, founded in 1980 by Carl Sagan, Bruce Murray and Louis Friedman, began working with the Russian Academy of Science on the mission Cosmos 1, hoping to conduct the first solar sail flight. "Cosmos 1 was a fully developed solar sail spacecraft intended to fly only under the influence of solar pressure for control of the spacecraft's orbit" said Friedman, director of the Planet Society [12]. The design consisted in eight triangular solar sails deployed and held rigid by inflatable booms. The launch took place in 2005, on a Russian Volna Rocket, but failed to reach orbit.

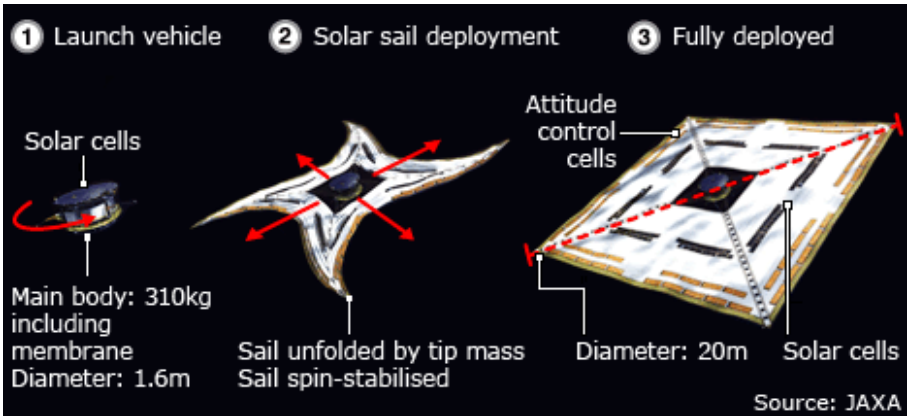

Figure 1.9: IKAROS solar sail deployment. Credit: JAXA

In 2010, JAXA (Japanese Aerospace Exploration Agency) launched IKAROS (Interplanetary Kite-craft Accelerated by Radiation of the Sun), which became the world's first solar sail spacecraft fully propelled by sunlight and the first to succeed in solar sail flight [15]. The mission's goal was to deploy and control the sail, determining minute orbit perturbations caused by light pressure; measurements were made by the AKATSUKI probe. The sail was a 192 m^2 square surface of polyimide sheet, 0.0075 mm thick, weighing 10 g/m^2, Figure 1.9. IKAROS travelled to Venus for six months, before embarking a three-year journey to the far side of the Sun. That same year, the NanoSail-D2 (following the failure of the fist NanoSail-D launch) was launched, the first solar sail deployed by NASA. The mission aimed to test the solar sail deployment technology and successfully demonstrated that the drag produced by a sail could be a viable means for deorbiting dead satellites and space debris. The sail was a 10 m^2 sheet made of aluminum and plastic and weighed 4.5 kg [16]. Meanwhile, in 2009, the Planetary

Society began developing the Light Sail, which was successfully launched in 2015 on Atlas V. The design featured a 32 m^2 mylar sail deployed in four triangular segments, carrying a 3U CubeSat. The purpose of the test was to allow a full checkout of the satellite's systems in advance of LightSail-2. LightSail-2 was launched in 2019 on the Falcon Heavy rocket, the mission lasted nearly three-and-a-half years demonstrating that small spacecraft can carry, deploy, and utilize relatively large solar sails for propulsion [14].

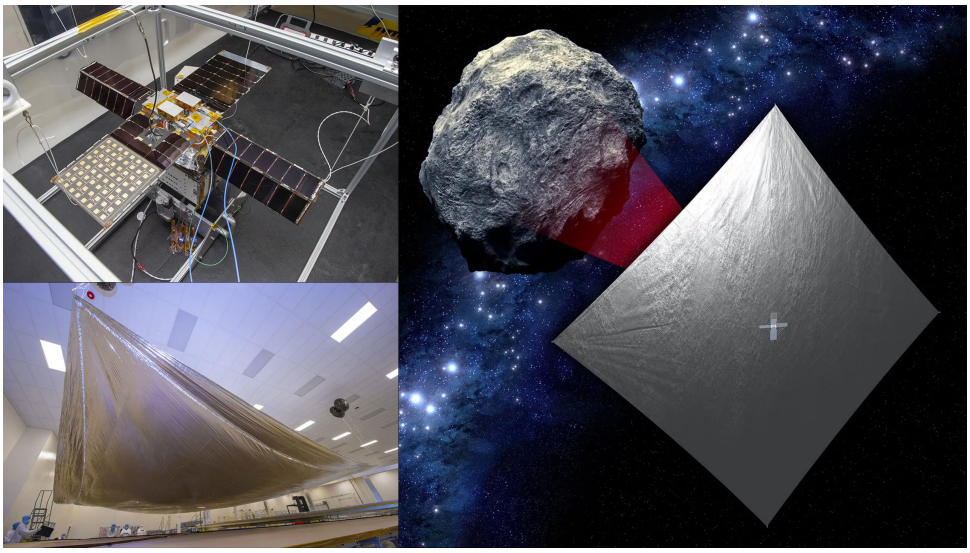

Figure 1.10: NEA Scout is composed of a small CubeSat (top left) and a thin, aluminum-coated solar sail (bottom left). The sail will use sunlight to propel the CubeSat to a small asteroid (as depicted in an illustration, right) [17].

In 2022, the mission NEA Scout developed by NASA's Marshall Space Flight Center (MSFC) and the Jet Propulsion Laboratory (Jet Propulsion Laboratory (JPL)) was launched. The mission was supposed to take a small CubeSat propelled by a solar sail to a near Earth asteroid. The 83 m^2 aluminized polyimide solar sail, launched to the Moon on Artemis I, was to deploy upon reaching the moon, spiral out of lunar orbit and travel to a near-Earth asteroid to perform a slow flyby, capturing images of the surface. Unfortunately, NASA lost contact with NEA Scout after the separation from Space Launch System (SLS) [18]. In 2024, the Advanced Composite Solar Sail System (ACS3) mission was launched. The mission featured a 12U CubeSat propelled by a quadratic 80 m^2 solar sail of polyethylene naphthalate film coated on one side with aluminum for reflectivity and on the other side with chromium to increase thermal emissivity, held by a carbon fibre reinforced polymer boom system. The mission served as a technology demonstration of NASA's deployable composite boom technology in a solar sailing application [19]. The spacecraft confirmed to be successfully operational after launch.

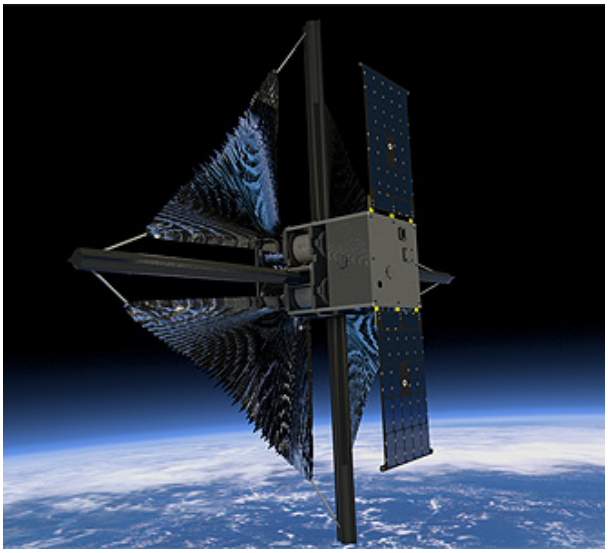

Figure 1.11: ACS3 solar sail during deployment [20].

1.2 Solar sails shapes

Solar sails are usually categorised by their shape and support structures. The first differentiation that can be made is between rigid and non-rigid sails. Rigid sails require a supporting structure to maintain their deployment, non-rigid sails only rely on centrifugal force-induced tensions. In the rigid solar design, the shape is maintained by connecting all edges to rigid structural support spars. There are three proposed designs for rigid solar sails, which are the clipper type, quad sailer type, and butterfly type. The structure support helps to reduce membrane flexibility, scales well and is suitable for a broad spectrum of attitude control strategies.

Figure 1.12: Clipper or square design [21].

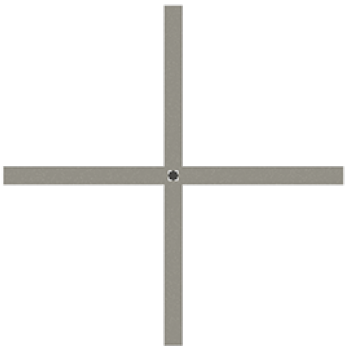

Figure 1.13: Heliogyro design [21].

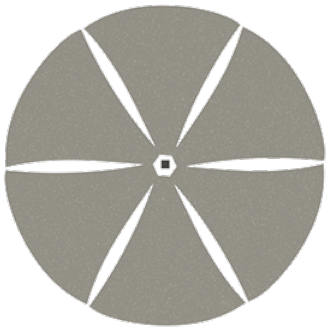

Figure 1.14: Spinning disk design [21].

The most popular design is the clipper or square sail, as it necessitates a lower number of structural elements (four instead of eight) compared with the quad sailer design and a larger surface area compared with the butterfly type. It consists of four sections attached to four structural elements as seen in Figure 1.12 [22]. Another advantage of this configuration is that there are no hot spots on the spacecraft because the sail protects the spacecraft from the sun's thermal heat. Non-rigid sails are also referred to as spin sails, as they rely on centrifugal force to maintain their shape. The heliogyro design was proposed by JPL in 1970s for the rendezvous

mission with the Halley's comet, see section 1.1. The shape resembles the rotor blades of a helicopter, with symmetrical strips arranged around a central hub Figure 1.13. Each blade can be rotated to manage attitude control. This design is advantageous as it is easy to store and deploy, but in order to have comparable surface area to the other configurations it needs to have very long blades. The spinning disk sail, also developed by JPL, consists of a hub from which a large sheet of sail membrane is deployed, Figure 1.14. A spinning disk solar sail was successfully deployed during the IKAROS mission, see section 1.1. The small gaps between sail masks helps maximize the amount of surface area similar to the square sail design [22][23].

1.3 Materials

Solar sails need to have a large surface area, with dimensions ranging from tens of metres to kilometres, therefore the candidate materials should be strong and exhibit minimal sagging or stretching. In order to provide a good thrust to mass ratio the sail material needs to be ultra-lightweight, with a density of a few g/m^2. The sail will be deployed in space, so the material should be capable of being folded or compressed until deployed and should be resistant to ionizing radiation, as it will operate in a harsh radiative environment, encountering galactic and solar particles (electrons and protons), x-rays, ultraviolet light, and magnetically trapped charged particles [1]. A selection of suitable materials chosen for their relevance, availability, and manufacturability is reported on Table 1.1, with their physical characteristics:

Table 1.1: Summary of different samples, including base polymer, thickness, and coating details.

Sample Description	**Base Polymer**	**Base Thickness** $[\mu m]$	**Front Coating Thickness** $[nm]$	**Front Coating Element**	**Back Coating Thickness** $[nm]$	**Back Coating Element**
Aluminized Mylar	Mylar	3.0	50	Al	50	Al
Aluminized Mylar With Chromium	Mylar	0.9	50	Al	20	Cr
Aluminized Kapton	Kapton	8.0	30	Al	30	Al
Aluminized CP1	CP1	3.0	50	Al	None	None

1.4 Advantages and disadvantages of solar sailing

Solar sailing is a propulsion system that relies on the momentum exchange, generated by the interaction between sunlight and sail material, to produce thrust. Unlike chemical propulsion systems, which rely on fuel, sunlight is an inexhaustible source of energy. Using light as the

source of energy enables the generation of continuous small thrust and infinite specific impulse, as the spacecraft is able to accelerate as long as sunlight is available, ultimately achieving velocities that are unattainable with rocket-propelled spacecrafts [24]. Beyond enabling continuous propulsion, the elimination of fuel dependency makes long-duration missions, where carrying sufficient fuel would be impractical, more feasible. One of the problem of chemical propulsion is the limitation of maximum payload capacity due to fuel weight and fuel management and storage system. Eliminating these aspects significantly reduces the spacecraft's weight and complexity. This translates into economic advantages, as the absence of a propulsion system lowers mission costs in terms of launch, operations, manufacturing, and maintenance [24]. Despite its advantages, in many cases solar sailing is not a suitable option. These spacecraft exhibit very low initial acceleration, which makes this method unsuitable for missions with time constraints or that require rapid departure. Solar sailing is heavily dependent on sunlight availability; therefore, its effectiveness diminishes as the spacecraft moves away from the sun. While in some mission it is possible to acquire the necessary thrust before moving moving beyond effective solar range, in other cases different propulsion systems are a better option. Moreover, although the absence of conventional propulsion systems offers several benefit, the design of solar sail introduces structural challenges. To ensure sufficient thrust, the sail needs to have a large surface area, as the force exerted by solar radiation on 1 m^2 sail is on the order of millinewtons. Deploying and maintaining a sail of this size requires accurate planning of the supporting structure and deployment mechanisms. In addition, the thin materials the sail is made of are vulnerable to damage from micrometeoroids and space debris. Regarding manoeuvrability, the spacecraft's ability to change direction is strictly limited by the direction of incoming sunlight and, while the solar sail thrust can be oriented changing the control angles, solar sails are less precise and have slower response times compared to fuel-based systems. Finally, in terms of sustainability, solar sailing represents an environmentally friendly solution, as it does not produce harmful byproducts and does not necessitate resource-intensive fuel production.

1.5 Applications of Solar Sail Propulsion

As stated in the previous paragraph, the solar sailing technique allows for missions that would be difficult for traditional propulsion systems. Solar sail-propelled spacecraft would be able to maintain highly non-Keplerian orbits, which are extensions of the classic two-body and three-body problems of orbital mechanics [25]. These orbits have a wide application range including Earth observation, planetary science, and space-based geoengineering [24]. An example would be the Geostorm mission, which aims to use a non-Keplerian orbit, near the L1 Lagrangian point, for Solar observations and early warning for impending coronal mass ejections [26]. Solar sailing is also a suitable method for active space debris removal. By leveraging the drag produced by a solar sail, it is possible to deorbit small spacecraft flying in low orbits, as demonstrated during the Nanosail-D mission [16] and the RemoveDEBRIS mission [27]. In the case of high orbits, solar radiation pressure can be used to transfer space debris into cemetery orbits [28]. Additionally, by employing the sail acceleration as a balancing force, it is possible to perform pole sitter missions, where the spacecraft will be balanced on top of the Earth's pole, with interesting applications for scientific observation missions and communication purposes [29]. Another promising field of application, which has recently been researched, is solar sail formation flight, especially for deep space [24]. The continuous thrust capability of solar sails makes them a valuable option for missions of flybys and rendezvous of small celestial bodies.

NASA Marshall Space Flight Center performed an assessment of the feasibility of using a near-term solar sail propulsion system to visit six NEA with a single solar sail-propelled spacecraft [30]. In 1986 a rendezvous mission with the Halley's comet was proposed by NASA [3]. A solar sail-based comet chaser has also been proposed, where the solar sail would be placed in a co-orbit with a comet [31].Solar sailing also holds significant potential for interplanetary missions. For example, a solar sail with a large payload mass fraction and a characteristic acceleration of 0.25 mm/s^2 could deliver the payload to Mercury in 3.5 years, while a solar sail with doubled performance would take only 1.5 years [32]. In 1999, NASA proposed the concept of an interstellar probe mission. The mission would require a 500-800 m diameter sail, with a 1 g/m^2 areal density [31]. Using a 100-km-class sail, unfurled at less than 0.2 AU, it could be possible to complete a trip to the nearest star in under a thousand years [31]. Solar sailing techniques are also suitable for attitude control, as demonstrated during the Mariner 4 and Mariner 10 missions 1.1.

1.6 CubeSat

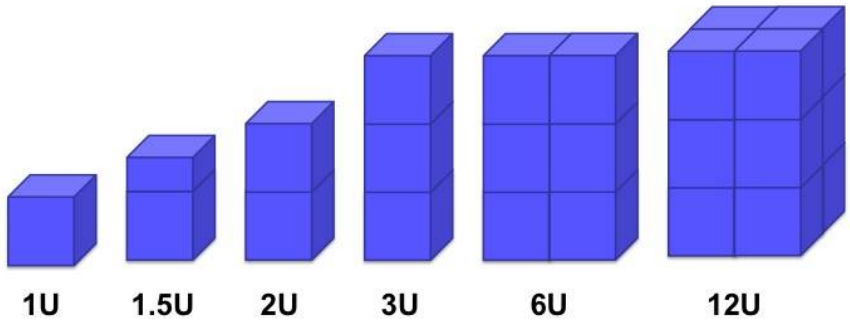

Figure 1.15: Standard sizes of CubeSats [33].

CubeSats are a class of nanosatellites weighing between 1 and 10 kilograms, which conform to a specific standard for size and form. By stacking multiple CubeSat units, different sizes are obtained. A CubeSat unit (1U) is a cube of 10 cm per side that weighs less than 2 kg. The different sizes, ranging from 1U to 12U, are illustrated in Figure 1.15. They are usually built using Commercial Off The Shelf (COTS) components for electronics and structural elements. The reduced dimensions and the use of standard components make this type of satellite more cost-effective than traditional satellites. The idea was originally proposed at California Polytechnic State University at San Luis Obispo (Cal Poly) and Stanford University as a practical way to learn satellite design without having to incur the substantial cost of a traditional satellite. This solution is now used outside the educational context, enabling cost-effective missions [33].

For the mission studied in this thesis, the satellite selected for attachment to the solar sail is a CubeSat. CubeSats are excellent candidates for solar sail missions due to their compact size, modularity, and low cost.

Chapter 2

Science Objective

Asteroids are minor celestial bodies, made up of rocky, icy, or metallic materials, originated during the early formation of the Solar System, approximately 4.6 billion years ago [34].

The first asteroid discovery is dated 1801 by the astronomer Giuseppe Piazzi. The asteroid was named Ceres, after the ancient Roman grain goddess and patron goddess of Sicily. The term 'asteroid', which comes from the Greek word "starlike", was later suggested by Charles Burney Jr. to Herschel, who proposed it to the Royal Society.

Asteroids have a composition similar to that of terrestrial planets; however, they are too small to be classified as such. Their size varies significantly, ranging from 1-metre rocks to bodies of thousands of kilometres in diameter, which can be classified as dwarf planets. All asteroids orbit the Sun in elliptical orbits and move in the same direction as the major planets. The majority of asteroids is characterized by an irregular shape. This is due to their small size, as these bodies experience the domination of the rock's compressive strength over the gravitational pressure. On the other hand, the largest asteroids experience gravity domination over material strength and their external forms are relatively close to a spherical shape.

As the population of asteroids is extremely extensive, asteroids are assigned numbers as well as names. The numbers are assigned consecutively after accurate orbital elements have been determined. The names can be selected by asteroid discoverers and are submitted to the International Astronomical Union (IAU) for approval.

2.1 Asteroid Locations

2.1.1 The Main Belt

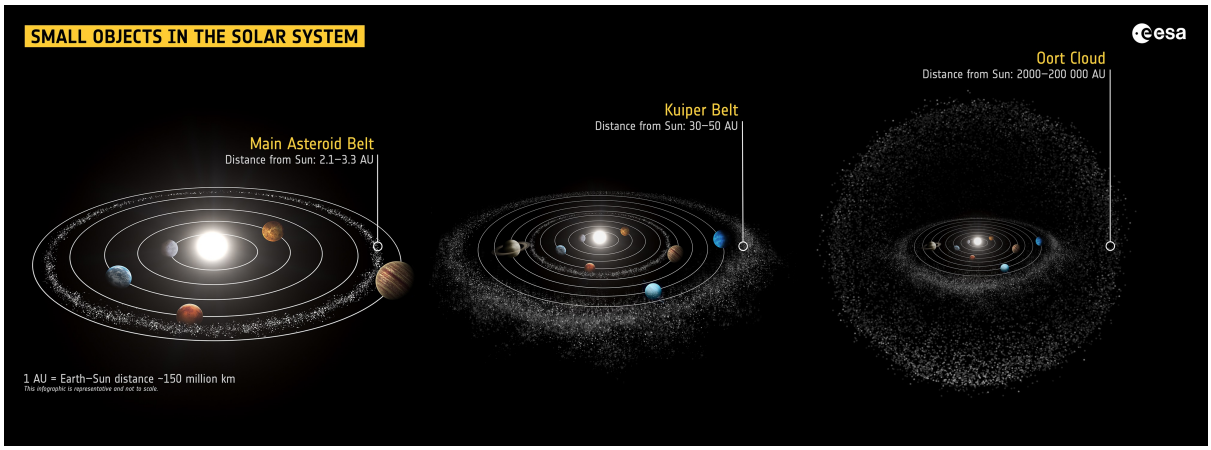

Figure 2.1: Asteroids position [35].

The Main Asteroid Belt is the region of the inner Solar system, where the majority of asteroids is located. This area is situated between the orbits of Mars and Jupiter, at a distance of 2.1-3.3 AU from the Sun, as can be observed in Figure 2.1.

The great density of bodies in this area is justified by the hypothesis that, during the formation of the Solar System, the gravitational influence of Jupiter prevented the formation of planetary bodies, causing the collision and fragmentation of the material [36].
The mass of the material in this area is estimated to be around 3% of the mass of the Moon. The Main Belt contains tens of thousands of objects of various sizes and compositions. The largest bodies located in this region are Ceres, Vesta, Pallas e Igea.

The Main Belt can be divided into two regions: the inner and outer belt. The inner belt, centred at 2.8 AU from the Sun, contains silicate-rich or S-type asteroids. The outer belt, centred at 3.2 AU, contains asteroids rich in carbon or C-type asteroids.

Asteroids can also be grouped into 'families'. Families of asteroids are clusters of bodies that share a similar orbit. Each family is named after the asteroid with the lower number, which was the fist discovered of the group. The three largest families in the Main Asteroid Belt are named Eos, Koronis, and Themis.

2.1.2 Kirkwood Gaps

The asteroids located between Mars and Jupiter are not distributed uniformly, but there are relatively empty areas called the Kirkwood gaps. The Kirkwood gaps are due to mean-motion resonances with Jupiter's orbital period. Such a gravitational resonance causes the asteroid to experience a gravitational force in a fixed direction whenever it is in the same relative position with respect to Jupiter. Repeated applications of that force eventually change the mean distance of that asteroid—and others in similar orbits—thus creating a gap in the distribution. Between the Kirkwood gaps, there are some mean-motion resonances areas, that, instead of dispersing asteroids, tend to collect them. These areas are the location of some asteroid clusters, listed in Table 2.1.

Table 2.1: Cluster of Asteroids in orbital resonances with Jupiter.

Asteroid Cluster	Distance [AU]	Resonance
Hungarians	1.78	5:1
Cybeles	3.58	7:4
Hildas	3.97	3:2
Thule	4.29	4:3
Trojans	5.20	1:1

2.1.3 Trojan Asteroids

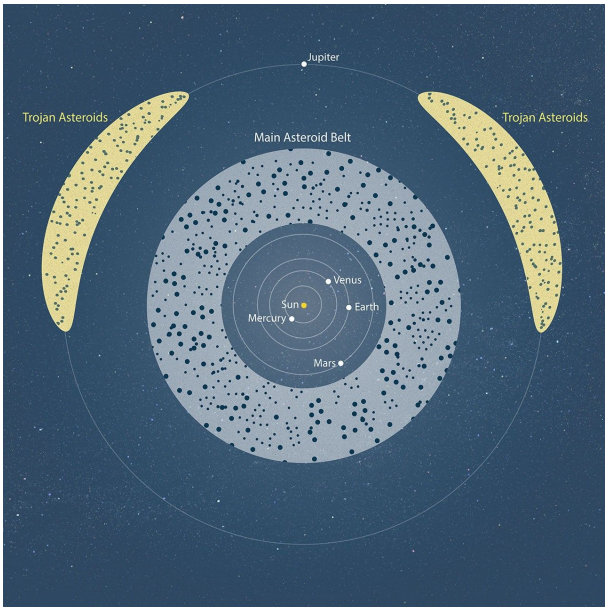

Figure 2.2: Trojans asteroids location [37].

Beyond the clusters of asteroids in orbital resonance with Jupiter, the Trojans cluster is the second largest reservoir in the inner solar system. The Trojans are located near Jupiter's L4 and L5 Lagrange points, which can be found at 60 degrees ahead and 60 degrees behind Jupiter in its solar orbit, as illustrated in Figure 2.2. However, the gravitational influence of bodies, primarily Saturn, perturbs the system and leads to a destabilization of those equilibrium points. As a consequence of these perturbations, the Trojan asteroids are observed 40° ahead of Jupiter and 70° behind it in its orbit. Orbiting in these equilibrium points ensures that these bodies do not collide with the planet.

2.1.4 Near Earth Asteroids

The small fraction of the asteroid population, whose orbits come into proximity with Earth are classified as NEA. NEA have a perihelion distance q less than 1.3 AU and can be classified based on their orbital characteristics. The farthest class is the Amor asteroids, named after

asteroid Amor, these are Earth-approaching NEAs with orbits exterior to Earth's but interior to Mars'. Because of strong gravitational perturbations produced by their close approaches to Earth, the orbital elements of all Earth-approaching asteroids change appreciably on timescales as short as years or decades. Asteroids that actually cross Earth's orbital path are known as Earth-crossers. This body represents a hazard for Earth's security, as they could impact on the planet, among this there are the Apollos and Atens. The Apollos have a semi-major axis larger than Earth's, they cross Earth's orbit when near the closest points to the Sun in their own orbits. The Apollos are named after asteroid Apollo. The Atens asteroids cross Earth's orbit when near the farthest points from the Sun of their orbits, as they are characterized by semi-major axes smaller than Earth's.They are named after asteroid Apollo. The Atiras asteroid, named after asteroid Atira, have an orbit entirely inside that of Earth, thus do not cross Earth's orbit [38]. NEAs categories are listed in Table 2.3, where q is the perihelion distance, Q the aphelion distance, and a the semi-major axis [39]. Finally, the PHA are asteroids with an Earth

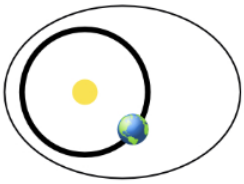

Figure 2.3: Amors [39].

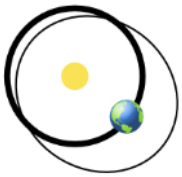

Figure 2.4: Apollos [39].

Figure 2.5: Atens [39].

Figure 2.6: Atiras [39].

Table 2.2: Classification of NEAs based on orbital characteristics.

Name	**Semi-Major Axis**	**Perihelion/aphelion distance**
Atens	$a < 1.0$ AU	$Q > 0.983$ AU
Apollos	$a > 1.0$ AU	$q < 1.017$ AU
Amors	$a > 1.0$ AU	$q = 1.017$–1.3 AU
Atiras	$a < 1.0$ AU	—

Minimum Orbit Intersection Distance (MOID) of 0.05 AU or less and an absolute magnitude (H) of 22.0 or less.

2.1.5 Centaurs

The Centaurs are a group of asteroids located between Jupiter and Neptune. Their orbits are quite elliptic, as their perihelion is located near the orbit of Jupiter and the aphelion near the orbit of Neptune.

The largest body of this cluster, Chiron, was discovered in 1977 and it measures approximately 100 km in diameter. The origin of the Centaurs is attributed to the perturbation of cometary nuclei that migrated into this region from the Kuiper Belt.

2.1.6 Trans-Neptunian Objects

Objects situated beyond Neptune's orbit are called Trans Neptunian Objects (TNO)s. They are situated in the Kuiper Belt and the Oort Cloud, as illustrated in Figure 2.1.

The Kuiper Belt is located between 30 and 50 AU from the Sun. The objects within this area are considered to be cometary nuclei. The largest bodies discovered in the Kuiper Belt are Eris and Pluto, with estimated diameters of approximately 2400 km and 1800 km, respectively. Both are classified as dwarf planets. This region is considered the source of the majority of comets that enter the inner Solar System.

The Oort Cloud is a shell of icy objects believed to surround the entire Solar System. This region can be further divided into a spherical outer Oort Cloud with a radius of some 20000–200000 AU and a doughnut-shaped inner Oort Cloud with a radius of 2000–20000 AU. The Oort Cloud is thought to contain billions of comets and is considered a major reservoir of long-period comets.

2.2 Composition

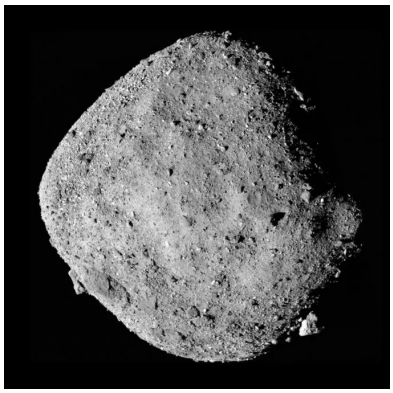

Figure 2.7: Asteroid Bennu, C-type [40].

Figure 2.8: Asteroid 433 Eros, S-type [41].

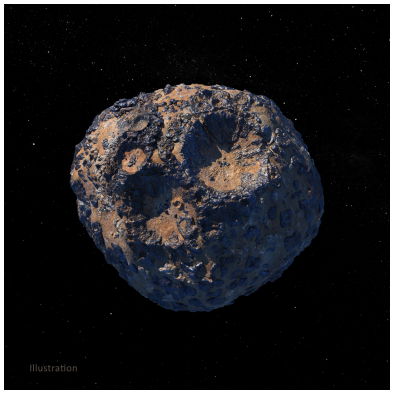

Figure 2.9: Asteroid Psyche concept, M-type [42].

Asteroids can be classified according to their chemical composition, based on observed colour, spectral reflectance, and albedo (i.e., surface reflectivity) [43]. Although there are multiple types of asteroids, the most common compositions can be grouped into three main taxonomic classes: C-type, S-type, and M-type. The chemical composition of an asteroid is typically correlated with its position in the Solar System.

C-type asteroids, or carbonaceous asteroids, are the most abundant, accounting for nearly 80% of asteroids located on the outer edge of the Main Asteroid Belt. They are rich in carbon molecules and are composed of clay and silicate rocks. Their composition is very similar to that of the carbonaceous chondrite meteorites. C-type asteroids appear of a dark reddish colour, as can be seen by observing the asteroid Bennu [Figure 2.7], which belongs to this class.

S-type, or "stony" asteroids, make up about 17% of the total asteroid population. They consist of nickel-iron mixed with iron- and magnesium-silicates, and are typically found in the inner regions of the asteroid belt. A notable siliceous asteroid is Eros [Figure 2.8], the first discovered and second-largest near-Earth asteroid.

M-type asteroids, or metallic asteroids, are mostly made up of nickel-iron [36]. Their composition varies depending on how far from the Sun they formed. In some cases, they possess

an iron core, formed as a result of exposure to high temperatures. The heat causes the iron to melt and subsequently to sink to the centre. Among metallic asteroids, Psyche [Figure 2.9] can be mentioned [44].
The characteristics of the taxonomic classes are summarized in Table 2.3.

Table 2.3: Classification of asteroids by spectral type, albedo, frequency, and composition.

Type	**Description**	**Albedo**	**Percentage**	**Composition**
C-type	Dark, reddish asteroids; the most common spectral class	< 0.10	$> 75\%$	Similar to carbonaceous chondrites; chemically similar to the Sun minus volatiles
S-type	Brighter asteroids; second most common type	0.10–0.22	$\sim 17\%$	Nickel-iron mixed with iron- and magnesium-silicates
M-type	Moderately bright asteroids; less abundant	0.10–0.18		Primarily composed of pure nickel-iron

2.3 Reasons for visiting asteroids

Mission towards asteroids are justified by the numerous benefits that the study of these bodies can offer.
Asteroids originated during the early formation of the Solar system, approximately 4.6 billion years ago. Their ancient origin makes them a valuable source of information for the investigation of the Solar system. In fact, studying the location and the distribution of the different types of asteroids guarantees an important insight into the formation and development of the Solar System. The origin of the Moon itself is believed to have been caused by an asteroid impact on our planet. The giant-impact hypotheses is, in fact, one of the most plausible hypothesis advanced on the Moon's formation. The giant-impact hypothesis theorizes that the formation of the satellite is the consequence of the collision between a planetary body named Theia and Earth, dated approximately 4.5 billion years ago. The debris generated by the impact is thought to have coalesced to form Earth's natural satellite. Various theories also suggest that asteroid impacts on Earth played a crucial role in delivering chemical components necessary for the development of life forms. These impacts also delivered greenhouse gases, such as nitrogen, carbon dioxide, and others, enhancing Earth's overall habitability. For this reason, the investigation of asteroids is considered a fundamental step to understand the origin of life on Earth. Evidence also suggests that water may have been delivered to Earth by icy asteroid-like impacts. Considering this theory, the study of the origin of water on Earth is closely linked to the study of asteroids.
Besides the scientific research mentioned before, visiting asteroids has a great value for human colonization. Asteroids represent potential sites for human colonization, particularly those located within the Main Asteroid Belt. They are also great reservoirs of valuable resources and chemical components that are rare on Earth, making them of interest for future space mining initiatives.

Visiting asteroids it is also important from a planetary defense perspective. A small number of NEA is classified as potentially hazardous objects, the trajectory of these bodies comes at a small distance from Earth and could impact our planet, creating substantial damage. Monitoring their trajectories and developing effective mitigation strategies is essential to reduce the risk of catastrophic impacts. [45]

2.4 Missions

The first mission to traverse the asteroid belt was *Pioneer 10*, launched in 1972. Although the mission performed only a transfer through the region, the successful passage opened the way for future exploration missions within the asteroid belt [46]. The first asteroid study was conducted by the *Galileo probe*, which succeeded in capturing images of the asteroids Gaspra [47] and Ida [48], during its flybys of these two bodies on its way to Jupiter. The first rendezvous with a NEA was achieved by the *Near-Earth Asteroid Rendezvous (NEAR) Shoemaker* mission in 1997. The spacecraft performed close flybys of several asteroids, including 253-Mathilde, which became the first carbonaceous Main Belt asteroid to be approached [49]. Following this phase, it targeted asteroid 433-Eros, a Mars-crosser and the largest near-Earth celestial body [50]. In 1999, NASA's *Deep Space I* performed a partially successful flyby of asteroid 9969-Braille at a distance of 26 km. Although the mission failed to capture detailed images, it retrieved valuable information about the asteroid [51]. One year later, the probe *Cassini–Huygens* successfully performed a distant flyby of the Main Belt asteroid 2685-Masursky [52]. Later in that same year, NASA's mission *Stardust*, on its way to collect dust samples from the comet Wild2's coma, travelled close to the asteroid 5535-Annefrank [53]. The *Hayabusa* mission represented the first attempt to return a sample from an asteroid to Earth. The target of the mission was asteroid 25143-Itokawa, a member of the Apollo group of near-Earth asteroids [54]. In 2006, an image of 132524-APL, a small S-type asteroid located in the Main Asteroid Belt, was taken by NASA's *New Horizons* probe [55]. In 2004, the European space probe *Rosetta* was launched. The probe, during its voyage towards Comet Churyumov-Gerasimenko, performed flybys of two asteroids, 21-Lutetia, an M-class asteroid, and 2867-Steins [56]. Steins was the first E-class asteroid to be visited by a spacecraft. Rosetta became the first spacecraft to orbit the nucleus of a comet. Launched in 2007, NASA's *Dawn* mission had the ambitious goal of exploring two of the largest bodies in the main asteroid belt, Ceres and Vesta [57]. The mission aimed both to test the capabilities of ion propulsion systems and to gain insights into the early processes of Solar System formation. Vesta, a rocky object, was confirmed to be a protoplanet with an iron core. Ceres, an icy body, revealed bright patches of salt on its surface and evidence of a subsurface frozen ocean. Following the first *Hayabusa* mission, a second asteroid rock sample-return mission, *Hayabusa2*, was launched in 2014. The spacecraft targeted asteroid 162173 Ryugu, a C-type carbon-rich asteroid, and was equipped with a suite of instruments for remote sensing and sample collection. The mission provided valuable insights into the composition and structure of carbon rich asteroids [58]. In 2016, NASA's Origins, Spectral Interpretation, Resource Identification, Security, Regolith Explorer (OSIRIS-REx) mission was launched toward the asteroid 101955 Bennu, a carbonaceous body with a diameter of approximately 490 m. The mission successfully collected around 60 g of surface material [59]. In 2021, NASA launched the *Lucy* mission, a twelve-year journey aimed at visiting ten different asteroids.To date, the spacecraft has completed a flyby of asteroid 152830 Dinkinesh. In 2025, it is scheduled to encounter asteroid 52246 Donaldjohanson, followed by a series of flybys through the Trojan asteroid population. These include 3548 Eurybates and its satellite, 15094

Polymele, 11351 Leucus, and 21900 Orus. The mission will then continue toward the L5 Trojan cloud, where in 2033 it will explore the binary system composed of asteroid 617 Patroclus and its natural satellite, Menoetius [60]. The spacecraft of the Double Asteroid Redirection Test (DART) program, a collaboration between NASA and Johns Hopkins Applied Physics Laboratory, was launched in 2021. The primary objective of the program was to test a defense strategy against near-Earth object threats by evaluating the capability of a spacecraft impact to alter an asteroid's trajectory. The target was Dimorphos, a small natural satellite orbiting the asteroid Didymos. The spacecraft successfully collided with Dimorphos in 2022, reducing its orbital period by 32 minutes [61]. As part of the mission, the Italian Space Agency contributed *LICIACube*, a CubeSat that separated from the main spacecraft prior to impact and was able to capture images of the collision and its aftermath [62].

2.5 Target asteroids

For the purpose of this thesis, three Near-Earth asteroids have been selected as the target bodies for the mission.

2.5.1 2000 SG344

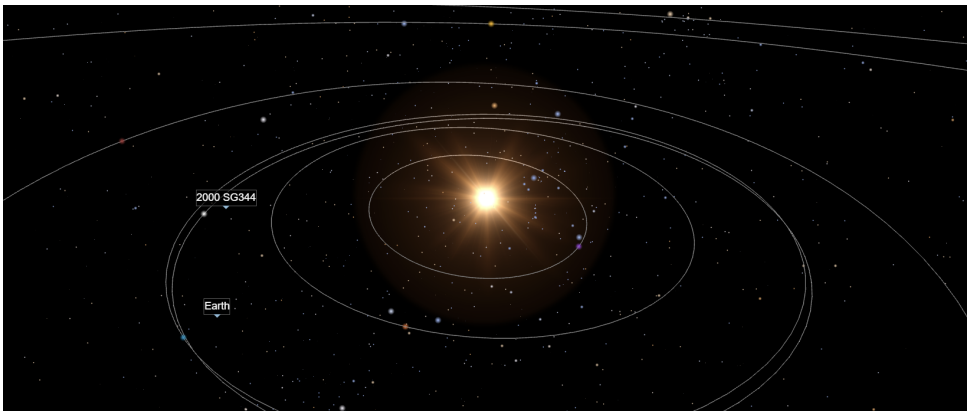

Figure 2.10: 2000 SG344 orbit [63].

2000 SG344 is a small asteroid, with an estimated diameter of 0.055 km, first observed in 2000. It has been classified as a NEA by NASA JPL, but it is not considered potentially hazardous. Based on its orbital parameters, it belongs to the Atens. Its orbit is shown in Figure 2.10 and its orbital elements are displayed in Table 2.4.

Table 2.4: Orbital elements of 2000 SG344

2000 SG344	
Orbital Element	**Value**
Semi-major axis a [AU]	0.9774397
Eccentricity e	0.06695788
Inclination i [deg]	0.11220
Argument of periapsis ω [deg]	275.34682
Right Ascension of Ascending Node Ω [deg]	191.91229
Mean anomaly M [deg]	35.6801073

2.5.2 2014 QN266

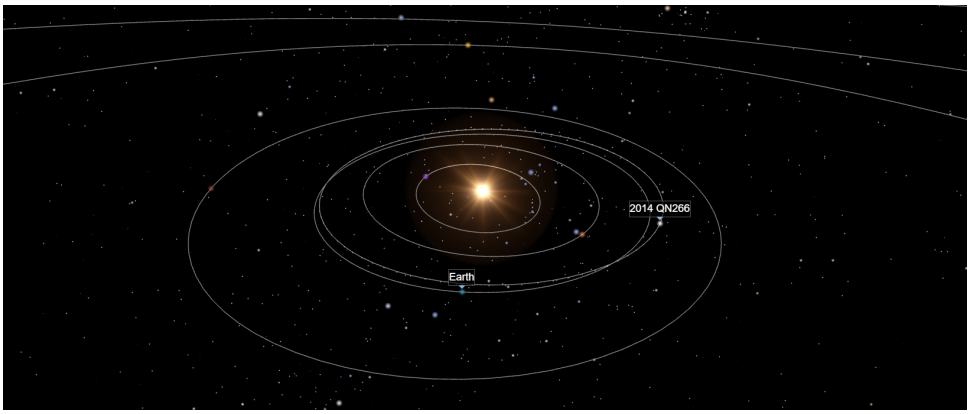

Figure 2.11: 2014 QN266 orbit [63].

2014 QN266 is an Apollo-class Asteroid classified as a NEA by NASA JPL and it is not considered a potentially hazardous object. Its dimension is very small, as it measures between 0.010 and 0.043 kilometres in diameter. Its orbit is shown in Figure 2.11 and its orbital elements are displayed in Table 2.5.

Table 2.5: Orbital elements of 2014 QN266

2014 QN266	
Orbital Element	**Value**
Semi-major axis a [AU]	1.0526284
Eccentricity e	0.09231390
Inclination i [deg]	0.48842
Argument of periapsis ω [deg]	61.61526
Right Ascension of Ascending Node Ω [deg]	171.11193
Mean anomaly M [deg]	211.2672992

2.5.3 2020 PJ6

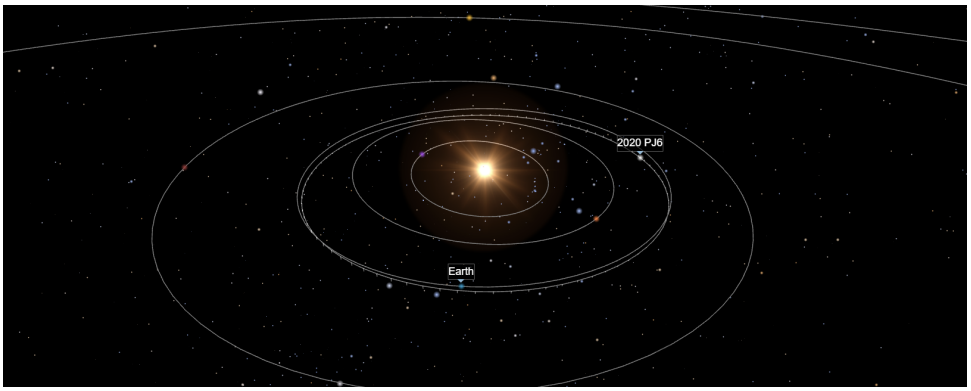

Figure 2.12: 2020 PJ6 orbit [63].

The third target asteroid is 2020 PJ6. This asteroid belongs to the Aten group. Its size ranges from 0.013 to 0.059 kilometres in diameter, which classifies it as a small asteroid. As the other target asteroid aforementioned, it is a NEA, but not a hazardous object. Its orbit is shown in Figure 2.12 and its orbital elements are listed in Table 2.6.

Table 2.6: Orbital elements of 2020 PJ6

2020 PJ6	
Orbital Element	**Value**
Semi-major axis a [AU]	0.9651751
Eccentricity e	0.09786949
Inclination i [deg]	0.81270
Argument of periapsis ω [deg]	312.41663
Right Ascension of Ascending Node Ω [deg]	141.66163
Mean anomaly M [deg]	160.5638083

Chapter 3

Trajectory Optimization

Orbit optimization is a fundamental topic in aerospace engineering, with applications ranging from interplanetary mission design to Earth observation and satellite station-keeping. An optimization problem consists of finding the control law that maximizes or minimizes a certain performance index, while satisfying physical and operational constraints. Considering the significant impact factors such as fuel consumption, payload mass, and transfer time have on both the design and cost of the mission, the performance index is often related to one of these factors. The mass of a solar sail-propelled spacecraft does not depend on the embarked fuel, which means minimizing the transfer period is usually the primary goal of trajectory optimization for this specific case. The resolution of an optimization problem cannot be achieved with an analytical method, as an explicit solution can be found for a limited number of simplified cases, which are not generally of practical interest. In most situations, it is necessary to employ a numerical method or an approximate solution.

3.1 Direct and Indirect Optimization Methods

Numerical optimization methods can be classified as direct or indirect. Direct optimization methods are based on discretization of the trajectory and the control parameters are described by an elevated number of variables. Optimization is performed using Non Linear Programming (NLP) techniques.

Direct methods are typically simpler to implement, compared to indirect methods. However, the solutions they produce tend to be less accurate. Indirect methods are based on the theoretical foundation of variational calculus and determine the control variables of the problem by solving a Boundary Value Problem (BVP). These methods have a good theoretical content, meaning the method is mathematically well-founded and offers desirable properties, such as high numerical precision. Additionally, they require a lower number of parameters, which guarantees a lower calculation time. Despite their advantages, indirect methods are characterised by convergence difficulty and lower robustness, compared with direct methods. For the optimization problem addressed in this thesis the most appropriate approach is the application of optimal control theory, which is an indirect numerical method.

3.2 Variational Calculus

In order to present the numerical approach of optimal control theory, a brief introduction to variational calculus is provided. Variational calculus is a branch of mathematical analysis that

deals with finding functions or curves that optimize a certain value J, finding its maximum or minimum, usually expressed as a functional integral. The function needs to satisfy the differential equations that describe the problem and the boundary conditions. The differential equations that describe the evolution of the system between the initial and final point, for a general system, are, usually, in the form:

$$\dot{\boldsymbol{x}} = \frac{\mathrm{d}\boldsymbol{x}}{\mathrm{d}t} = \boldsymbol{f}(\boldsymbol{x}, \boldsymbol{u}, t) \tag{3.1}$$

Where $\boldsymbol{x}$ is the state variable vector, the time t is the independent variable, and $\boldsymbol{u}$ is the control variable. The boundary conditions can be expressed as:

$$\boldsymbol{\chi}(\boldsymbol{x}(t_0), \boldsymbol{x}(t_f), t_0, t_f) = 0 \tag{3.2}$$

The functional J can be defined according to Mayer's or Lagrange's formulation. The Mayer's formulation depends on the values of the variables at the endpoints of the curve and can be written in the form:

$$J = \varphi(\boldsymbol{x}(t_0), \boldsymbol{x}(t_f), t_0, t_f) \tag{3.3}$$

Lagrange's formulation is defined as an integral between the endpoints of the curve:

$$J = \int_{t_0}^{t_f} \varphi(\boldsymbol{x}, \dot{\boldsymbol{x}}, t)\mathrm{d}t \tag{3.4}$$

The solution of the problem is found using the Euler-Lagrange equation, which is a necessary condition for $J(y)$ to be a maximum or minimum:

$$\frac{\partial}{\partial t}\left(\frac{\partial \varphi}{\partial \dot{\boldsymbol{x}}}\right) - \frac{\partial \varphi}{\partial \boldsymbol{x}} = 0 \tag{3.5}$$

3.3 Optimal Control Theory for Orbit Optimization

In the context of orbit optimization, the problem is formulated by dividing the entire trajectory into distinct phases or arcs, within which variables remain continuous. Each j-th arc is defined by its initial time ($t_{(j-1)_+}$) and final time (t_{j_-}), where + denotes the value assumed by the time immediately after the point, and - immediately before it. The phase is described by its corresponding differential equation, expressed in the same form as in Equation 3.1. The values assumed by the state variable at the endpoints are indicated as $\boldsymbol{x}_{(j-1)_+}$ and $\boldsymbol{x}_{j_-}$, following the same notation used for time. Each arc is governed by a homogeneous control law. The boundary conditions are imposed at the endpoints of each phase, allowing for the consideration of flybys or constraints on the dynamic and thermal loads. The conditions are of mixed type, as they are applied to both dependent and independent variables. Boundary conditions are usually non-linear and are defined at the endpoint of each arc, formulated as in Equation 3.2:

$$\boldsymbol{\chi}(\boldsymbol{x}_{(j-1)_+}, \boldsymbol{x}_{j_-}, t_{(j-1)_+}, t_{j_-}) = 0 \qquad\qquad j = 1, ..., n \tag{3.6}$$

This method enables the consideration of variable discontinuities, which can be ascribed to impulsive manoeuvres, flybys, or the detachment of depleted rocket stages. It is important to note that boundary conditions can also be applied to the control variables contained in vector $\boldsymbol{u}$. The functional is written in its most general form, encompassing both the Mayer and Lagrange

formulations; when $\varphi = 0$, the pure Mayer formulation is obtained, when $\Phi = 0$ the pure Lagrange formulation is found:

$$J = \varphi(\boldsymbol{x}_{(j-1)_+}, \boldsymbol{x}_{j_-}, t_{(j-1)_+}, t_{j_-}) + \sum_j \int_{t_{(j-1)_+}}^{t_{j_-}} \Phi(\boldsymbol{x}(t), \boldsymbol{u}(t), t)\mathrm{d}t \qquad j = 1, ..., n \tag{3.7}$$

J depends on the values taken by the variables and time at the endpoints of each phase, accounting for both internal and external boundaries, this represents the contribution of the Mayer formulation. The second term, representing the contribution of the Lagrange formulation, is the integral over the entire trajectory, which is a function of time and values assumed by the state and control variables at each point. Equation 3.7 is then rewritten using Lagrange multipliers to incorporate the differential equations and boundary conditions, resulting in the implemented functional:

$$J^* = \varphi + \boldsymbol{\mu}^T \boldsymbol{\chi} + \sum_j \int_{t_{(j-1)_+}}^{t_{j_-}} \boldsymbol{\lambda}^T (\boldsymbol{f} - \dot{\boldsymbol{x}})\mathrm{d}t \qquad j = 1, ..., n \tag{3.8}$$

Where $\boldsymbol{\lambda}$ represents the adjoint variables, associated with the state equations, and $\boldsymbol{\mu}$ corresponds to the auxiliary constants associated with the boundary conditions. It is observed that when the boundary conditions and the differential equations are satisfied, the functional J and the implemented functional J^* are equal. Equation 3.8 is integrated by parts to eliminate the dependence on $\dot{\boldsymbol{x}}$:

$$J^* = \varphi + \boldsymbol{\mu}^T \boldsymbol{\chi} + \sum_j \left(\boldsymbol{\lambda}^T_{(j-1)_+} \boldsymbol{x}_{(j-1)_+} - \boldsymbol{\lambda}^T_{j_-} \boldsymbol{x}_{j_-}\right) + \sum_j \int_{t_{(j-1)_+}}^{t_{j_-}} \left(\Phi + \boldsymbol{\lambda}^T \boldsymbol{f} - \dot{\boldsymbol{\lambda}}^T \boldsymbol{x}\right) \mathrm{d}t$$
$$j = 1, \ldots, n \tag{3.9}$$

To determine the optimal value, J^* is differentiated as follows:

$$\begin{aligned}
\delta J^* = &\left(-H_{(j-1)_+} + \frac{\partial \varphi}{\partial t_{(j-1)_+}} + \boldsymbol{\mu}^T \frac{\partial \boldsymbol{\chi}}{\partial t_{(j-1)_+}}\right) \delta t_{(j-1)_+} + \\
&+ \left(H_{j_-} + \frac{\partial \varphi}{\partial t_{j_-}} + \boldsymbol{\mu}^T \frac{\partial \boldsymbol{\chi}}{\partial t_{j_-}}\right) \delta t_{j_-} + \\
&+ \left(\boldsymbol{\lambda}^T_{(j-1)_+} \frac{\partial \varphi}{\partial \boldsymbol{x}_{(j-1)_+}} + \boldsymbol{\mu}^T \frac{\partial \boldsymbol{\chi}}{\partial \boldsymbol{x}_{(j-1)_+}}\right) \delta \boldsymbol{x}_{(j-1)_+} + \\
&+ \left(-\boldsymbol{\lambda}^T_{j_-} + \frac{\partial \varphi}{\partial \boldsymbol{x}_{j_-}} + \boldsymbol{\mu}^T \frac{\partial \boldsymbol{\chi}}{\partial \boldsymbol{x}_{j_-}}\right) \delta \boldsymbol{x}_{j_-} + \\
&+ \sum_j \int_{t_{(j-1)_+}}^{t_{j_-}} \left(\left(\frac{\partial H}{\partial \boldsymbol{x}} + \dot{\boldsymbol{\lambda}}^T\right) \delta \boldsymbol{x} + \frac{\partial H}{\partial \boldsymbol{u}} \delta \boldsymbol{u}\right) \mathrm{d}t \qquad j = 1, \ldots, n
\end{aligned} \tag{3.10}$$

Where $\delta \boldsymbol{x}, \delta \boldsymbol{u}, \delta \boldsymbol{x}_{(\boldsymbol{j-1})_+}, \delta \boldsymbol{x}_{\boldsymbol{j}_-}, \delta t_{(j-1)_+}, \delta t_{j_-}$ are arbitrary variations and H is the system's Hamiltonian and is defined as:

$$H = \Phi + \boldsymbol{\lambda}^T \boldsymbol{f} \tag{3.11}$$

The necessary condition to guarantee the optimal value, a maximum or minimum, of J^* is that the functional is stationary. This condition is satisfied when its first variation vanishes identically for all permissible arbitrary variations, while fulfilling the boundary conditions and the governing differential equations. This is accomplished through the adjoint variables ($\boldsymbol{\lambda}$) and constants ($\boldsymbol{\mu}$) previously introduced, which, when properly chosen, enable the nullification

of each coefficient of the arbitrary variations in Equation 3.10. This results in the first variation of the functional being equal to zero $\delta J^* = 0$, ensuring the stationary property of the functional J^*. Consequently, by equating, in the integral, the coefficient of $\delta \boldsymbol{x}$ to zero at each point of the trajectory, the differential equations for the Euler-Lagrange adjoint variable are obtained:

$$\frac{\mathrm{d}\boldsymbol{\lambda}}{\mathrm{d}t} = -\left(\frac{\partial H}{\partial \boldsymbol{x}}\right)^T \tag{3.12}$$

By repeating this process for the coefficient of $\delta \boldsymbol{u}$, the algebraic control equations are obtained:

$$\left(\frac{\partial H}{\partial \boldsymbol{u}}\right)^T = 0 \tag{3.13}$$

It is worth noting that the control laws and boundary conditions remain unchanged whether the objective is to find a maximum or minimum of J.

When deriving the control law, particular attention must be given to the constraints imposed on the control variables, which must belong to a certain admissibility domain, defined by the given constraints. In this case the optimal value must be determined in accordance with Pontryagin's Maximum Principle, which states that the control value that optimizes the trajectory in each point is the one that, while being in the admissibility domain, maximizes the Hamiltonian H, when seeking the maximum of J, or minimizes it, when searching for the minimum. After solving Equation 3.13 two cases may arise: either the obtained value belongs to the admissibility domain or it does not. In the first scenario, the control is said to be locally unconstrained, as the constraint does not affect that point, and the solution corresponds to the value obtained from Equation 3.13. In the second scenario, the optimal value falls outside the admissibility domain, and the maximum or minimum permissible value is attained at the boundaries of the domain.

Another consideration must be made in the particular case where the Hamiltonian is linear with respect to one of the constrained controls. In this situation, the control does not appear explicitly in Equation 3.13 and thus cannot be determined. If the control coefficient in Equation 3.11 is non-zero, H is maximised when the control value is maximum, if the coefficient is positive and when the control value is minimum, if the coefficient is negative, assuming we are seeking to maximize J. The values are reversed when searching for the minimum of J. In the opposite case, if the control coefficient is zero over a defined time interval, it becomes necessary to impose the vanishing of all successive derivatives of the coefficient with respect to time, until the control explicitly appears in one of them. The optimal control is then determined by setting this last derivative equal to zero. It has been proven that the required order of differentiation is always even [64] and half of this order is used to denote the order of the singular arc. The remaining boundary conditions are the optimal conditions. They are expressed in terms of the j-th boundary, referring either to the upper bound of the $(j-1)-th$ subinterval or to the lower bound of the $j-th$ subinterval. By setting to zero in order the variations $\delta \boldsymbol{x}_{j_-}, \delta \boldsymbol{x}_{j_+}, \delta t_{j_-}, \delta t_{j_+}$ of Equation 3.10, the following conditions are obtained:

$$-\boldsymbol{\lambda}_{j_-}^T + \frac{\partial \varphi}{\partial \boldsymbol{x}_{j_-}} + \boldsymbol{\mu}^T \left[\frac{\partial \boldsymbol{\chi}}{\partial \boldsymbol{x}_{j_-}}\right] = 0 \qquad j = 1, ..., n \tag{3.14}$$

$$\boldsymbol{\lambda}_{j_+}^T + \frac{\partial \varphi}{\partial \boldsymbol{x}_{j_+}} + \boldsymbol{\mu}^T \left[\frac{\partial \boldsymbol{\chi}}{\partial \boldsymbol{x}_{j_+}}\right] = 0 \qquad j = 0, ..., n-1 \tag{3.15}$$

$$H_{j_-} + \frac{\partial \varphi}{\partial t_{j_-}} + \boldsymbol{\mu}^T \left[\frac{\partial \boldsymbol{\chi}}{\partial t_{j_-}}\right] = 0 \qquad j = 1, ..., n \tag{3.16}$$

$$-H_{j_+} + \frac{\partial \varphi}{\partial t_{j_+}} + \boldsymbol{\mu}^T \left[\frac{\partial \boldsymbol{\chi}}{\partial t_{j_+}} \right] = 0 \qquad\qquad j = 0, ..., n-1 \tag{3.17}$$

Equations 3.14 and 3.16 are not defined at the beginning of the trajectory where $j = 0$, while Equations 3.15 and 3.17 are not valid at the end of the trajectory where $j = n$. By eliminating the auxiliary constants $\boldsymbol{\mu}$ from Equations 3.14 to 3.17 the optimal boundary conditions can be written as:

$$\boldsymbol{\sigma}(\boldsymbol{x}_{(j-1)_+}, \boldsymbol{x}_{j_-}, \boldsymbol{\lambda}_{(j-1)_+}, \boldsymbol{\lambda}_{j_-}, t_{(j-1)_+}, t_{j_-}) = 0 \tag{3.18}$$

Equation 3.18 together with the assigned boundary conditions in Equation 3.6 completes the differential system, given by Equations 3.1 and 3.12. Equations 3.14 and 3.15 provide the optimal conditions imposed on the adjoint variable λ_x, when its corresponding state variable x is subject to specific boundary conditions. Different cases are possible. If the state variable x is explicitly prescribed at the initial time, the vector $\boldsymbol{\chi}$ of the assigned boundary conditions will include the equation $x_0 - a = 0$, where a is a known constant. In this case, on the corresponding adjoint variable λ_{x_0} no specific optimal condition will be imposed. If the initial value of the state variable x_0 is neither specified in the function φ nor in the assigned boundary conditions $\boldsymbol{\chi}$, its corresponding adjoint variable will be equal to zero $\lambda_{x_0} = 0$. The same principle applies when x is assigned at the final time or if it is not defined. If the state variable is continuous and not assigned at an internal point, $\boldsymbol{\chi}$ will include the equation $x_{j+} = x_{j-}$, and the corresponding adjoint variable will also be continuous $\lambda_{x_{j+}} = \lambda_{x_{j-}}$. Finally, if the state variable is continuous and assigned to an internal point, $\boldsymbol{\chi}$ will include the equation $x_{j+} = x_{j-} = a$. In this case the corresponding adjoint variable will exhibit a "free" discontinuity, meaning that the value of $\lambda_{x_{j+}}$ is independent of the value of $\lambda_{x_{j-}}$ and will be determined through the optimization process. Regarding Equations 3.16 and 3.17, if the Hamiltonian H is not an explicit function of time, they can, in some cases, introduce additional optimal boundary conditions. The possible situations are explained. When the initial time t_0 does not appear explicitly either in the boundary conditions $\boldsymbol{\chi}$ or in the function φ, the Hamiltonian at the initial time is zero, $H_0 = 0$. The same holds for the final time. When an intermediate time instant t_j does not explicitly appear in the function φ, the only boundary condition involving that time instant in $\boldsymbol{\chi}$ is the requirement of temporal continuity, in other words $t_{j_+} = t_{j_-}$. This implies that the Hamiltonian H remains continuous in j $H_{j_+} = H_{j_-}$. Instead, when the time t_j is explicitly assigned in $\boldsymbol{\chi}$, the equations $t_{j_+} = t_{j_-} = a$ will appear, and the Hamiltonian will exhibit a free discontinuity.

3.4 Boundary Value Problem

After the problem formulation has been addressed, the indirect optimization method used to solve it is described in this paragraph. In the previous section, the problem was formulated as follows: the problem is described by the differential Equations 3.2 and 3.12, the control variables are determined by Equation 3.13, the imposed boundary conditions are given by (3.6) and Equations 3.18 determine the optimal boundary condition. Both the differential equations and the boundary conditions are strictly dependent on the type of orbits involved in the transfer. Since not all initial values of the variables are known, the problem is classified as a BVP and must be solved using a numerical method. The indirect optimization method consists in applying optimal control theory to the system of differential equations. Optimal control theory formulates the optimization problem as a mathematical problem subject to differential and algebraic boundary conditions. The solution is obtained by determining appropriate initial values for the unknown variables, such that, when integrating the system of differential equations, all

imposed and optimal boundary conditions are satisfied. The problem exhibits specific characteristics. The integration interval is divided into subintervals, within which the differential equations may have different expressions. The duration of each subinterval is generally unknown. The boundary conditions can be non-linear and can be referred to both internal and external boundaries of the intervals. The variables can be discontinuous at internal boundaries and their value after a discontinuity point can be unknown. Given the characteristics of the problem, the main challenge in applying an indirect optimization technique lies in solving the BVP. The solution techniques must have the same characteristics as the problem itself. In this case, the solution is obtained by reducing the BVP to a sequence of initial value problems, which are brought to convergence using Newton's method. One of the listed peculiarities of the problem is the unknown duration of each interval. To address this issue, the time variable t is replaced, for the purpose of integration, with a new variable ε, defined in the $j-th$ subinterval:

$$\varepsilon = j - 1 + \frac{t - t_{j-1}}{t_j - t_{j-1}} = j - 1 + \frac{t - t_{j-1}}{\tau_j} \tag{3.19}$$

Where τ_j is the duration of the subinterval. Using this approach, the internal and external boundaries become fixed and correspond to consecutive integer values of the new variable ε. By referring to Equations 3.1, and 3.12 and rewriting the control variable using Equation 3.13, a differential problem in state and adjoint variables is obtained. The variables are no longer distinguished, and are represented as $\boldsymbol{y} = (\boldsymbol{x}, \boldsymbol{\lambda})$:

$$\frac{\mathrm{d}\boldsymbol{y}}{\mathrm{d}t} = \boldsymbol{f}^*(\boldsymbol{y}, t) \tag{3.20}$$

It is noted that the problem also includes constant parameters, such as the duration of the subintervals or the values of variables defined after a discontinuity point. To account for these constant parameters, a new vector $\boldsymbol{z}$ is defined. The vector containing both the state and adjoint variables, along with the constant parameters $\boldsymbol{c}$, is defined as $\boldsymbol{z} = (\boldsymbol{y}, \boldsymbol{c})$. By changing the independent variable, the system of differential equations becomes:

$$\frac{\mathrm{d}\boldsymbol{z}}{\mathrm{d}\varepsilon} = \boldsymbol{f}(\boldsymbol{z}, \varepsilon) \tag{3.21}$$

By explicitly expressing the right-hand side of Equations 3.21, for the state and adjoint variables the equation results:

$$\frac{\mathrm{d}\boldsymbol{y}}{\mathrm{d}\varepsilon} = \tau_j \frac{\mathrm{d}\boldsymbol{y}}{\mathrm{d}t} \tag{3.22}$$

For the constant parameters stand:

$$\frac{\mathrm{d}\boldsymbol{c}}{\mathrm{d}\varepsilon} = 0 \tag{3.23}$$

The boundary conditions are defined without distinguishing between imposed and optimal conditions, using the vector:

$$\boldsymbol{\Psi}(\boldsymbol{s}) = 0 \tag{3.24}$$

Where $\boldsymbol{s}$ is a vector that contains the values assumed by the variable at each endpoint of the subintervals, indicated by $\varepsilon = 0, 1, ..., n$, and the unknown parameters:

$$\boldsymbol{s} = (\boldsymbol{y}_0, \boldsymbol{y}_1, ..., \boldsymbol{y}_n, \boldsymbol{c}) \tag{3.25}$$

As previously mentioned, some of the initial values of the variables are unknown, and the solution of the problem consists of determining, through an iterative process, the values they must take to satisfy Equation 3.24.

3.5 Iterative Process

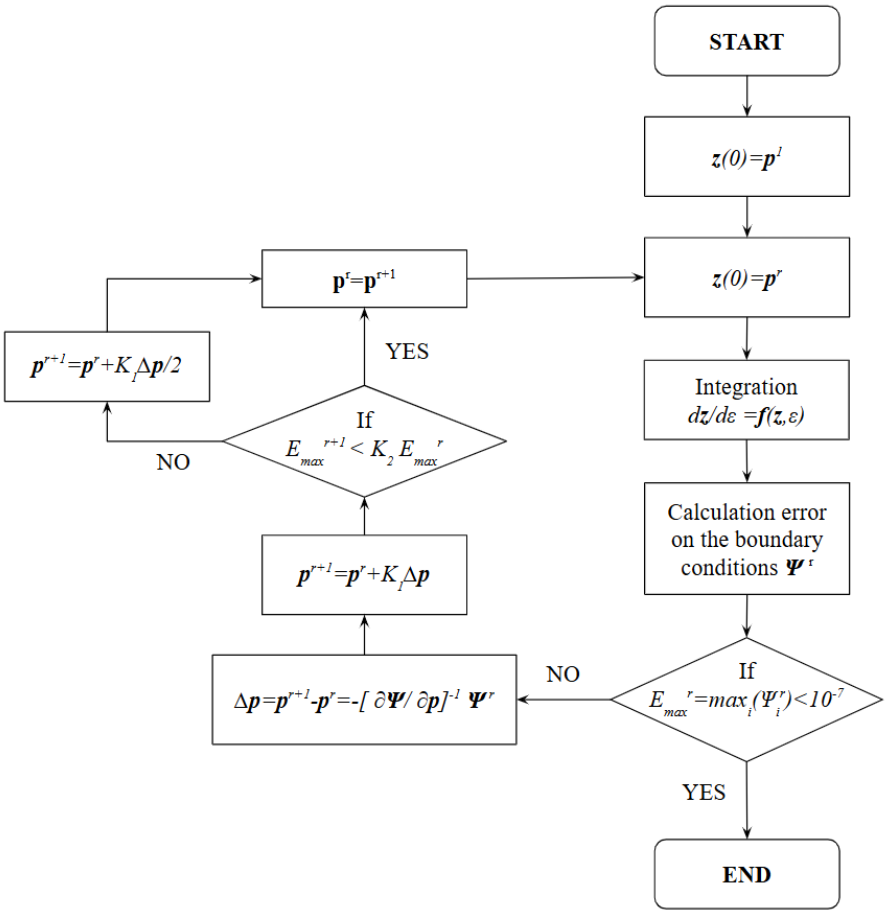

Figure 3.1: Flow diagram of the iterative process

The following section describes the iterative process, briefly illustrated in the flow diagram in Figure 3.1, under the assumption that none of the initial values are known. The $r-th$ iteration consists of integrating Equations 3.21 using as initial values those obtained from the $(r-1)-th$ iteration, i.e. by solving the equation:

$$\boldsymbol{z}(0) = \boldsymbol{p}^r \tag{3.26}$$

The same process is repeated along the entire trajectory, accounting for any discontinuities at the internal endpoints. Obviously, since the results from the previous iteration are not yet available during the first iteration, the values of $\boldsymbol{p}^1$ are arbitrarily chosen. After each iteration, the values of the state variables at each internal endpoint are determined and, after the integration, the errors in the boundary conditions $\boldsymbol{\Psi}^r$ are calculated. At each iteration, the variation $\Delta\boldsymbol{p}$ causes the error in the boundary conditions to vary by an amount that, accounting only for the first-order terms, is:

$$\Delta\boldsymbol{\Psi} = \left[\frac{\partial\boldsymbol{\Psi}}{\partial\boldsymbol{p}}\right]\Delta\boldsymbol{p} \tag{3.27}$$

The objective is to nullify the error in the boundary conditions, meaning that the desired variation of the error should be $\Delta\boldsymbol{\Psi} = -\boldsymbol{\Psi}^r$. This is achieved by correcting the initial values of a

quantity:

$$\Delta \boldsymbol{p} = \boldsymbol{p}^{r+1} - \boldsymbol{p}^{r} = -\left[\frac{\partial \boldsymbol{\Psi}}{\partial \boldsymbol{p}}\right]^{-1} \boldsymbol{\Psi}^{r} \tag{3.28}$$

This process is repeated until the boundary conditions of Equation 3.24 are satisfied within the desired precision. The matrix $[\partial \boldsymbol{\Psi}/\partial \boldsymbol{p}]$ is calculated as a matrix product:

$$\left[\frac{\partial \boldsymbol{\Psi}}{\partial \boldsymbol{p}}\right] = \left[\frac{\partial \boldsymbol{\Psi}}{\partial \boldsymbol{s}}\right] \left[\frac{\partial \boldsymbol{s}}{\partial \boldsymbol{p}}\right] \tag{3.29}$$

Where the first matrix $[\partial \boldsymbol{\Psi}/\partial \boldsymbol{s}]$ is obtained by differentiating the boundary conditions with respect to the quantities that appear in them. The second matrix $[\partial \boldsymbol{s}/\partial \boldsymbol{p}]$ contains the derivatives of the variable values at the boundaries with respect to the initial values, i.e. the values assumed at the endpoints by the matrix:

$$\left[\frac{\partial \boldsymbol{z}}{\partial \boldsymbol{p}}\right] = [\boldsymbol{g}(\varepsilon)] \tag{3.30}$$

The second matrix $[\partial \boldsymbol{s}/\partial \boldsymbol{p}]$ is obtained by integrating the system of differential equations derived from differentiating the principal system of Equation (3.21), with respect to the initial values:

$$[\dot{\boldsymbol{g}}] = \frac{\mathrm{d}}{\mathrm{d}\varepsilon}\left[\frac{\partial \boldsymbol{z}}{\partial \boldsymbol{p}}\right] = \left[\frac{\partial}{\partial \boldsymbol{p}}\left(\frac{\partial \boldsymbol{z}}{\partial \varepsilon}\right)\right] = \left[\frac{\partial \boldsymbol{f}}{\partial \boldsymbol{p}}\right] \tag{3.31}$$

Where the dot $\dot{}$ now indicates the differentiation with respect to the new independent variable ε. By explicitly calculating the Jacobian of the main system of Equation 3.21, the equation is rewritten as:

$$[\dot{\boldsymbol{g}}] = \left[\frac{\partial \boldsymbol{f}}{\partial \boldsymbol{z}}\right] \left[\frac{\partial \boldsymbol{z}}{\partial \boldsymbol{p}}\right] = \left[\frac{\partial \boldsymbol{f}}{\partial \boldsymbol{z}}\right] [\boldsymbol{g}] \tag{3.32}$$

The initial values for the homogeneous system in Equation 3.32 are obtained by differentiating Equation 3.26, resulting in the identity matrix:

$$[\boldsymbol{g}(0)] = \left[\frac{\partial \boldsymbol{z}(0)}{\partial \boldsymbol{p}}\right] = [\boldsymbol{I}] \tag{3.33}$$

It is worth noting that this method is capable of managing variable discontinuities. In fact, assuming there is a discontinuity at point i, it is sufficient to update the vectors $\boldsymbol{z}$ and $\boldsymbol{g}$ using the relation $\boldsymbol{h}$, which links the values of the variables before and after the discontinuity. The new values are written as:

$$\boldsymbol{z}_{i+} = \boldsymbol{h}(\boldsymbol{z}_{i-}) \tag{3.34}$$

$$[\boldsymbol{g}_{i+}] = \left[\frac{\partial \boldsymbol{h}}{\partial \boldsymbol{z}}\right] [\boldsymbol{g}_{i-}] \tag{3.35}$$

The definition of the function $\boldsymbol{h}$ is the reason why it is not necessary to distinguish between the vectors $\boldsymbol{y}_{i_+}$ and $\boldsymbol{y}_{i_-}$ when defining the vector $\boldsymbol{s}$, since each is a function of the other, through $\boldsymbol{h}$, and of $\boldsymbol{c}$. The problem has been presented in its most general form, assuming all the initial values of the variables are unknown. However, in most cases, some initial values are known. In this case, the problem is simplified, as the vector $\boldsymbol{p}$ is reduced to include only the unknown components of the vector $\boldsymbol{z}(0)$, and the vector $\boldsymbol{\Psi}$ is restricted to only the boundary conditions that are not explicitly defined at the initial time.

In the previous part the matrix $[\partial \boldsymbol{\Psi}/\partial \boldsymbol{p}]$ was calculated as a product of two matrices, however it can also be calculated numerically. The $i-th$ row is obtained by varying the $i-th$

component of the vector $\boldsymbol{p}$ by a small quantity Δp, typically on the order of $10^{-6} \div 10^{-7}$, while keeping the others fixed. Then, Equations 3.21 are integrated. Through this process, the variations of the boundary conditions $\Delta\boldsymbol{\Psi}(\Delta p)$ are obtained and, by linearizing the equations, the corresponding row is calculated as $\Delta\boldsymbol{\Psi}^T/\Delta p$. This approach, in some cases, allows for a simpler and faster resolution of the BVP, but it does not always guarantee convergence. The reason is that determining the matrix $[\partial\boldsymbol{\Psi}/\partial\boldsymbol{p}]$ using this approach yields a less accurate solution, compared to the first method, and, given the high numerical sensitivity of the problem, the numerical approximations introduced by the second approach can compromise convergence. A similar procedure could also be used to compute the Jacobian and the matrix $[\partial\boldsymbol{\Psi}/\partial\boldsymbol{s}]$, but the analytical formulation is preferred. The integrations of the differential equations, both for the main system of Equations 3.21 and the homogeneous system of Equations 3.32, are performed using a step-by-step numerical method with variable order, based on Adams formulas, as described by Shampine and Gordon [65]. The linearization introduced for the computation of the correction $\Delta\boldsymbol{p}$ in Equation 3.28 could introduce errors that could compromise convergence, causing the error in the boundary conditions to increase with each iteration, instead of decreasing. To avoid this phenomenon, some improvements can be introduced in the procedure. To prevent the correction from causing the iteration to diverge from the correct solution, the step Δp is modified such that the actual step is a fraction of Δp:

$$\boldsymbol{p}^{r+1} = \boldsymbol{p}^r + K_1\Delta\boldsymbol{p} \tag{3.36}$$

Where $K_1 = 0.1 \div 1$, the values are empirically determined during code testing, based on the distance between the initial solution and the searched solution. After computing the new vector of initial values $\boldsymbol{p}^{r+1}$ using Equation 3.36, the equations of motion are integrated and the maximum error in the boundary conditions is evaluated. The maximum error in the current iteration E^{r+1}_{max} is compared with the one of the previous iteration E^r_{max}. If the current error is smaller than a multiple of the previous error, i.e. $E^{r+1}_{max} < K_2 E^r_{max}$, the iterative process continues. A suitable choice for the coefficient K_2 is within the range $2 \div 3$. This value must be greater than 1, as the error in the boundary conditions may increase during the first iterations. In the other case, if the current error exceeds a multiple of the previous error, the next iteration is performed by bisecting the correction $\Delta\boldsymbol{p}$:

$$\boldsymbol{p}^{r+1} = \boldsymbol{p}^r + K_1\Delta\boldsymbol{p}/2 \tag{3.37}$$

When the iteration is completed, the current error is evaluated once again and, if necessary, the bisection process is repeated. In the implemented code, the maximum number of iterations has been set to 5. If the code does not converge before this limit is exceeded, then the chosen trial solution is not capable of achieving convergence [66].

Chapter 4

Theoretical Background: Flight Mechanics

The following chapter introduces some space flight concepts, which will be referenced in the next chapter, chapter 5, where the sail motion equations will be derived. Special emphasis is given to the reference frames, both spatial and temporal, to the two-body problem, which provides the theoretical basis on which the motion equations are formulated, and to the orbital parameters.

4.1 Reference frames

In order to properly describe the various problem vectors, it is necessary to define the reference frames in which they are represented. A reference frame is defined as an ordered set of three mutually orthogonal unit vectors. It is defined by specifying its origin, fundamental plane, which contains the x- and y-axes, and the direction and orientation of its axes. Within the reference frame, a coordinate system is employed to locate points in space.

Reference frames can be classified as inertial or non-inertial frames. Inertial reference frames do not rotate with respect to the stars and have a non-accelerating origin. Non-inertial reference frames experience a certain acceleration, resulting in relative accelerations between the bodies within the system.

This section provides a description of the different reference frames employed.

4.1.1 The Heliocentric-Ecliptic Reference frame

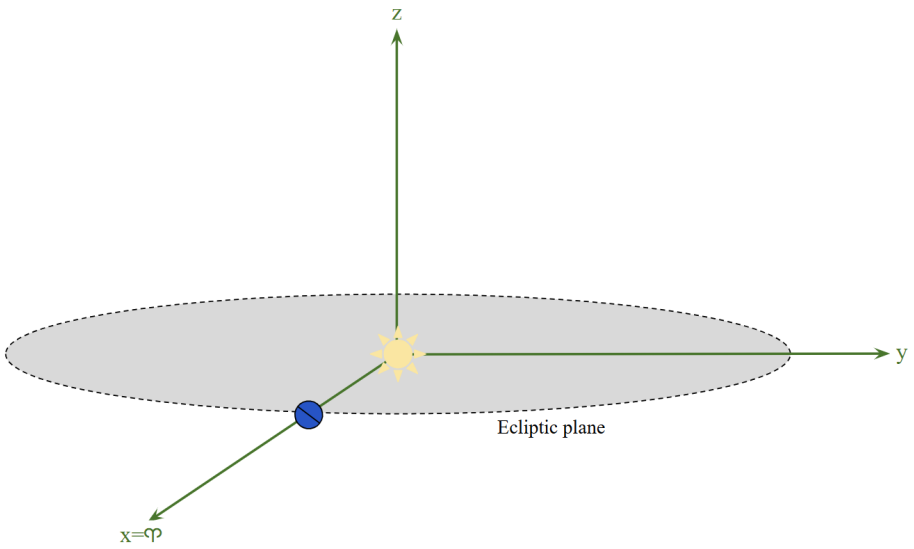

Figure 4.1: Heliocentric-Ecliptic Reference frame

The Heliocentric-Ecliptic reference frame [Figure 4.1] is centred on the Sun and based on the Ecliptic Plane, which is the orbital plane of the Earth. The frame is defined by three axes. The x-axis and y-axis are located on the fundamental Plane of the Ecliptic. The x-axis is defined by the intersection of the Ecliptic and Equatorial planes during the vernal equinox. The z-axis is normal to the Ecliptic Plane and is oriented toward the hemisphere in which the Pole Star is located. The y-axis completes the right-handed triad. The Heliocentric-Ecliptic reference frame is quasi-inertial, because it is fixed with respect to the fixed stars except for the precession of the equinoxes. The precession of the equinoxes is a perturbation that causes the line of equinoxes to be slightly non-aligned with the line of the apsides. This perturbation causes the line of apsides to rotate, describing a cone, with a period of approximately 26000 years and pointing from the Pole Star to the star Vega. This phenomenon is caused by the gravitation influence exerted on Earth by other celestial bodies, in particular the effect of the luni-solar attraction and planetary attraction. The rotation of the line of apsides causes the sidereal year to be longer than the solar year. The sidereal and solar years are respectively the time required for Earth to return to the same position relative to the fixed stars and the Sun. The sidereal year is completed with a 360-degree rotation around the Sun and it lasts 365 days, 6 hours, 9 minutes and 9 seconds. The solar year is completed with a rotation of 359.986 degrees and its duration is 365 days, 5 hours, 48 minutes and 46 seconds. For the purposes of this thesis, that takes into account a mission lasting a few years, the perturbation period results sufficiently long, that Heliocentric-Ecliptic reference frame can be approximated as inertial.

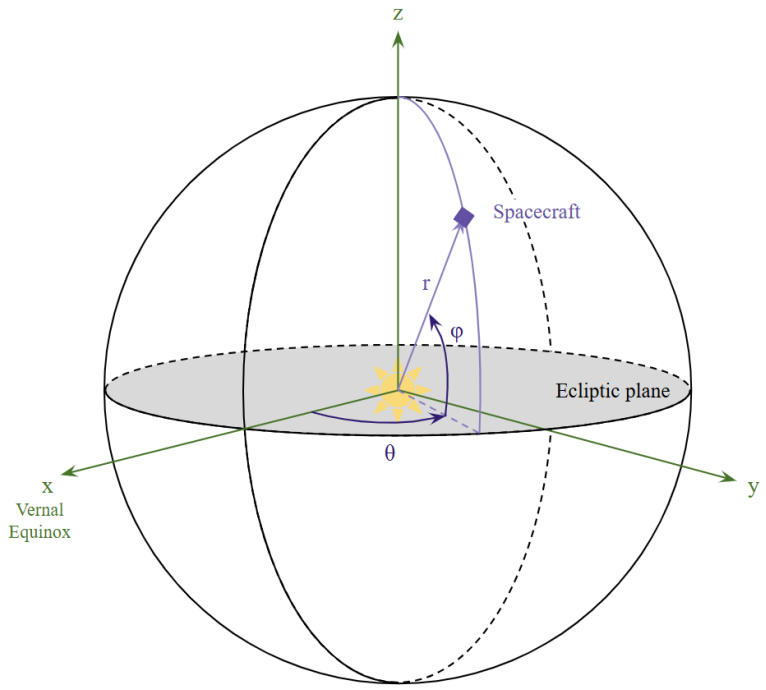

Figure 4.2: Spherical coordinates for the Heliocentric-Ecliptic Reference frame

Within the Heliocentric-Ecliptic reference frame, the position of the spacecraft can be described using a system of spherical coordinates, as illustrated in Figure 4.2. Spherical coordinates define the position of a given point in three-dimensional space by using one distance and two angles, which in this case are the heliocentric distance r, the heliocentric ecliptic longitude ϑ and latitude φ. The position coordinate vector is then expressed as:

$$\boldsymbol{r} = \begin{bmatrix} r \\ \vartheta \\ \varphi \end{bmatrix} \tag{4.1}$$

This reference frame proves to be the most suitable option when formulating the motion equations. Within an inertial frame, drag and Coriolis accelerations are absent, which significantly simplifies the definition of the Jacobian when solving the BVP. Furthermore, this reference frame guarantees a direct correspondence between the auxiliary variables associated with the velocity components and the elements of the primer vector.

4.1.2 The Perifocal-Heliocentric Reference Frame

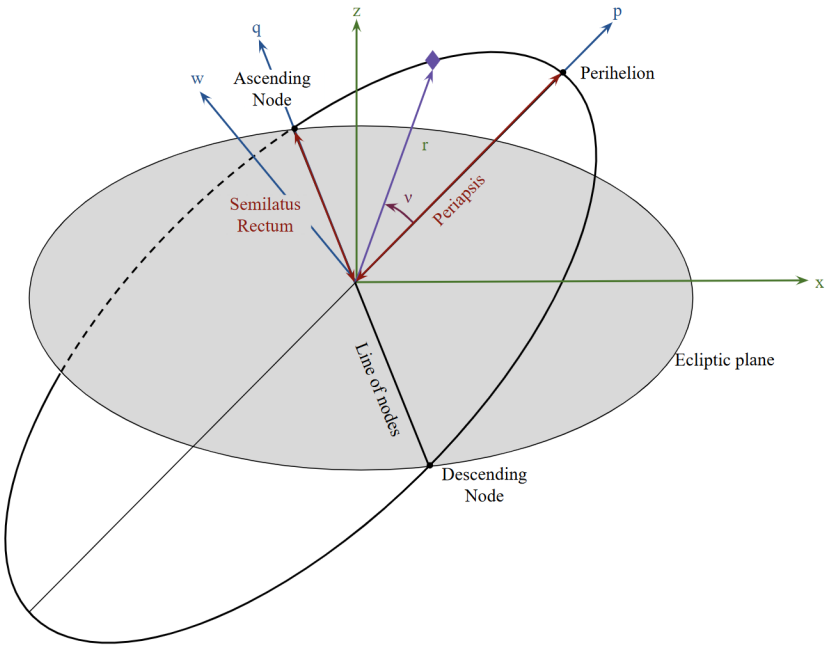

Figure 4.3: Perifocal Reference Frame

The Perifocal-Heliocentric Reference Frame is a Sun-centred system defined with respect to the orbital plane of the satellite. The orbital plane is defined by two vectors $\boldsymbol{p}$ and $\boldsymbol{q}$. $\boldsymbol{p}$ is the axis pointing toward the periapsis and $\boldsymbol{q}$ is the axis 90 ahead of $\boldsymbol{p}$ in the direction of satellite motion. The right-handed triad is completed by the w axis, which is normal to the orbital plane and aligned with the orbital angular momentum vector. The system is illustrated in Figure 4.3. This reference frame is used to define the orbital elements.

4.1.3 Local Reference Frame

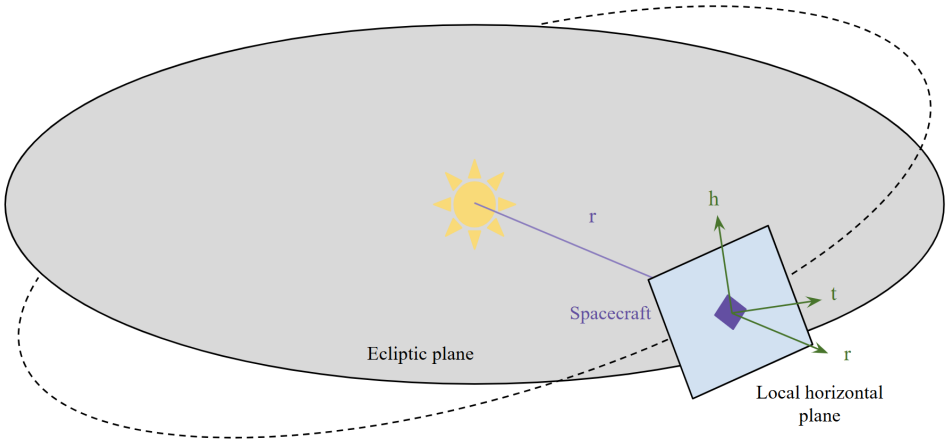

Figure 4.4: Local reference frame

The velocity components are defined in a local reference system, centred on the spacecraft and based on the local horizontal plane, as illustrated in Figure 4.4. The velocity coordinates are given by the vector:

$$\boldsymbol{V} = \begin{bmatrix} u \\ v \\ w \end{bmatrix} \tag{4.2}$$

Where u is the coordinate in the radial direction, v in the eastward direction and w in the northern direction. The choice of this reference frame for the velocity coordinates is motivated by the simpler relationship it provides between relative and absolute velocities.

4.2 Time System

In order to express the position of celestial bodies as a function of time, a temporal reference system must also be defined. The most commonly used time system for astronomical applications is the Julian Day (JD). The JD is a continuous date-counting system that facilitates conversions between different calendar systems used across various historical epochs. Its formulation is based on the Julian Period, which is the least common multiple of three traditional cycles:

- 15 years of the Indiction cycle, a Roman fiscal period used for tax assessment;
- 19 years of the Metonic cycle, after which the phases of the Moon recur on the same days of the solar year;
- 28 years of the solar cycle, the period after which the days of the week repeat on the same calendar dates in the Julian calendar.

The Julian Period, thus, is equal to:

$$\text{Julian Period} = 15 \cdot 19 \cdot 28 = 7980\, years \tag{4.3}$$

The JD count begins on January 1, 4713 Before Common Era (BCE), at 12:00 Coordinated Universal Time (UTC). It can be calculated from a date expressed in day/month/year (D/M/Y) format of the Gregorian Calendar, using the following formula:

$$a = fl\left[\frac{14 - M}{12}\right] \tag{4.4}$$

$$y = Y + 4800 - a \tag{4.5}$$

$$m = M + 12 \cdot a - 3 \tag{4.6}$$

$$J_D = D + fl\left[\frac{153 \cdot m + 2}{5}\right] + 365 \cdot y + fl\left[\frac{y}{4}\right] - fl\left[\frac{y}{100}\right] + fl\left[\frac{y}{400}\right] - 32045 \tag{4.7}$$

Where fl is a function that rounds the value to the nearest integer. For the Julian Calendar the formula is:

$$J_D = D + fl\left[\frac{153 \cdot m + 2}{5}\right] + 365 \cdot y + fl\left[\frac{y}{4}\right] - 32083 \tag{4.8}$$

An alternative time system is the Modified Julian Day (MJD), in this case the days count starts from November 16, 1858 CE, at 00:00 UTC. The MJD is obtained by subtracting 2,400,000.5 days from the corresponding JD value:

$$MJD = JD - 2400000.5 \tag{4.9}$$

It is also possible to account for the time of day by adding the fractional part of the day, to obtain the Julian Date. The time of the day can be calculated by knowing the angle between the Earth-Sun direction and the Greenwich Meridian. The angle is given by:

$$t = \frac{day}{365.2425 \cdot 100} \tag{4.10}$$

$$\alpha = \alpha_{G_0} + \omega_{\oplus} \cdot day + 0,0003875 \cdot t^2 \tag{4.11}$$

Where $\alpha_{G_0} = 280.40601837$ is the angle at J2000, corresponding to January 1, 2000 CE, at 00:00 UTC, $\omega_{\oplus} = 7.29 \cdot 10^{-5}\, rad/s = 360.9856473/s$ is Earth's angular velocity and day represents the number of JD since J2000. For this thesis, the time is evaluated by counting the JD starting from J2000 and is non-dimensionalised as explained in section 5.4.

4.3 Two Body problem

The equations of motion, in their general form, are derived from the two-body problem. The two-body problem describes the motion of the spacecraft in space, simplifying the N-body problem through three assumptions:

- Two celestial bodies are considered to influence the motion, with one body, in this case the Sun, having a significantly greater mass than the other, which is the spacecraft. This assumption implies that $M_1 >> m_2$.
- The bodies are considered to be spherically symmetric, allowing them to be modelled as point masses.
- The system is assumed to be isolated, with no external forces acting upon it other than the gravitational forces exerted by the two bodies under consideration.

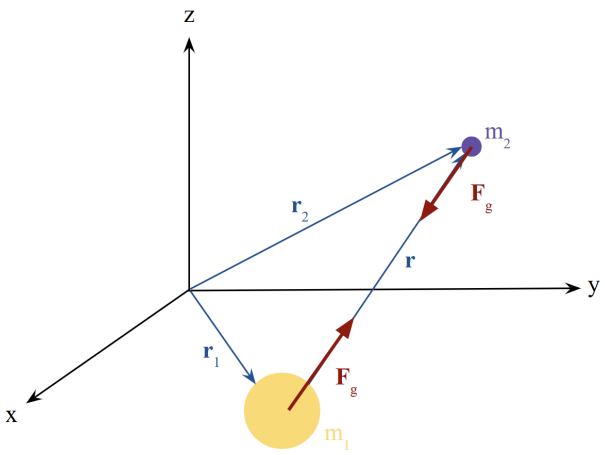

Figure 4.5: Two body problem

Under these assumptions, and by applying Newton's law of dynamics, it is possible to derive the expression for the acceleration of the second body relative to the first body, given by:

$$\ddot{\boldsymbol{r}} + \frac{\mu}{r^3}\boldsymbol{r} = 0 \tag{4.12}$$

Where $\ddot{\boldsymbol{r}}$ is the acceleration vector, μ is the gravitational parameter of the central body, $\boldsymbol{r}$ represents the position vector of the second body relative to the first and r is the magnitude of $\boldsymbol{r}$. The vectors can be observed in Figure 4.5. The gravitational parameter is given by the product of the gravitational constant $G = 6,67430 \cdot 10^{-11} \frac{Nm^2}{kg^2}$ and the mass of the body. For the Sun the gravitational parameter equals $\mu_\odot = GM_\odot = 1,32712440018 \cdot 10^{11} km^3 s^{-2}$. It is important to emphasize that, when using the two body problem to formulate the equations of motion, the model does not account for perturbations due to the presence of other celestial bodies or the deviations of the bodies from perfect spherical symmetry. Starting from the two-body problem formulation (Equation 4.12), the equation for the specific mechanical energy can be derived:

$$\mathcal{E} = \frac{V^2}{2} - \frac{\mu}{r} \tag{4.13}$$

The specific mechanical energy is the sum of the kinetic energy (first term) and the potential energy (second term). The gravitational field is conservative and the specific mechanical energy is a constant of motion, thus its value remains constant throughout the orbit. Another constant of motion that can be derived from the two-body problem is the angular momentum, which is given by:

$$\boldsymbol{h} = \boldsymbol{r} \times \boldsymbol{V} \tag{4.14}$$

This implies that the motion of the body is confined to a plane, known as the orbital plane. The solution to the two-body problem results in the equation:

$$r = \frac{h^2/\mu}{1 + \left(\frac{B}{\mu}\right) \cos \nu} \tag{4.15}$$

Where B is an integration constant. This equation represents a conic section centred on the primary body, which is located at one of the two foci. The conic equation is:

$$r = \frac{p}{1 + e \cos \nu} \tag{4.16}$$

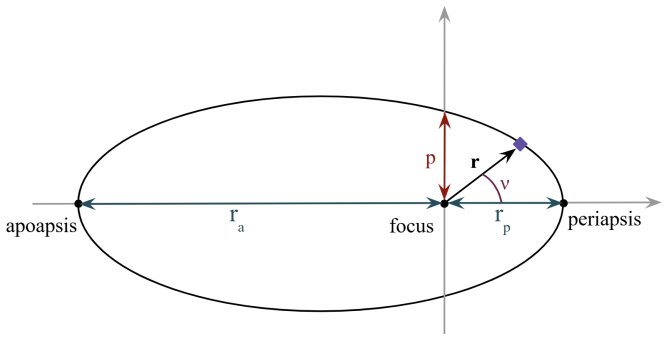

Figure 4.6: Conic section representation

Where r is the distance from the focus, p is the semilatus rectum, e is the eccentricity and ν is the true anomaly. The true anomaly is the angle between the direction of periapsis and the point considered. The eccentricity is the measure of the orbit's deviation from a perfect circle ($e = 0$ for circular orbits). Four types of conic sections can be identified. Their characteristics are listed in Table 4.1.

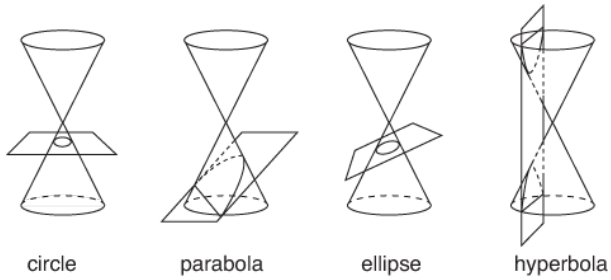

Figure 4.7: Enter Caption

Table 4.1: Classification of conic orbits based on eccentricity and energy

Orbit Type	**Eccentricity** e	**Specific Mechanical Energy** $\mathcal{E}$
Circular	$e = 0$	$\mathcal{E} < 0$
Elliptical	$0 < e < 1$	$\mathcal{E} < 0$
Parabolic	$e = 1$	$\mathcal{E} = 0$
Hyperbolic	$e > 1$	$\mathcal{E} > 0$

A conic section is defined as the locus of points for which the distance from the focus is proportional to the perpendicular distance from the directrix. This proportionality is expressed by the eccentricity, which can be written as:

$$e = \frac{c}{a} = \frac{r_a - r_p}{r_a + r_p} \tag{4.17}$$

Where c is the distance between the focus and the centre of the conic section, r_a is the distance between the focus and the apoapsis, and r_p is the distance between the focus and the periapsis. The semi-major axis is given by:

$$a = \frac{r_p + r_a}{2} \tag{4.18}$$

The semilatus rectum can be expressed as:

$$p = a(1 - e^2) \tag{4.19}$$

By comparing Equation 4.16 and Equation 4.15, the specific mechanical energy can also be expressed as:

$$\mathcal{E} = -\frac{\mu}{2a} \tag{4.20}$$

4.4 Cosmic velocities

The characteristic velocities can be derived from the conservation of mechanical energy, which is defined in Equation 4.13 and Equation 4.20.

Circular velocity

The circular velocity is the value that allows a satellite to orbit the central body in a circular orbit. In a circular orbit, the distance of the satellite from the focus is constant and equals to the radius of the circumference, thus $r = a$. Under these conditions, the circular velocity can be derived as:

$$\frac{v_c^2}{2} - \frac{\mu}{r} = -\frac{\mu}{2r} \rightarrow v_c = \sqrt{\frac{\mu}{r}} \tag{4.21}$$

Escape velocity

The escape velocity is defined as the minimum velocity required for a satellite to escape the gravitational influence of the central body it is orbiting. That is the velocity necessary to transition the satellite from a bound orbit to an open trajectory ($a \rightarrow \infty$, $v_\infty \rightarrow 0$). Under these conditions, the escape velocity is given by:

$$\frac{v_e^2}{2} - \frac{\mu}{r} = \frac{v_\infty^2}{2} - \frac{\mu}{r_\infty} = 0 \rightarrow v_e = \sqrt{\frac{2\mu}{r}} = \sqrt{2} v_c \tag{4.22}$$

Hyperbolic excess velocity

The hyperbolic excess velocity is the residual velocity that a satellite retains after performing an escape maneuver and following a hyperbolic trajectory ($r \rightarrow \infty$). It represents the satellite's velocity relative to the central body when it is at an infinite distance, where the gravitational influence of the body becomes negligible. It can be derived as:

$$-\frac{\mu}{2a} = \frac{v_\infty^2}{2} - \frac{\mu}{r} = \frac{v_\infty^2}{2} \rightarrow v_\infty = \sqrt{-\frac{\mu}{a}} \tag{4.23}$$

4.5 Equations of Dynamic

The equations of motion are derived from the two-body problem and are given by:

$$\frac{\mathrm{d}\boldsymbol{r}}{\mathrm{d}t} = \boldsymbol{V} \tag{4.24}$$

$$\frac{\mathrm{d}\boldsymbol{V}}{\mathrm{d}t} = \boldsymbol{g} + \frac{\boldsymbol{T}}{m} + \frac{\boldsymbol{D}}{m} + \frac{\boldsymbol{L}}{m} \tag{4.25}$$

$$\frac{\mathrm{d}m}{\mathrm{d}t} = -\frac{T}{c} \tag{4.26}$$

Where V is the velocity, T is the thrust, D and L are the aerodynamic forces, and m is the mass. The aerodynamic forces are considered only in cases where an atmosphere is present.

4.6 Orbital Parameters

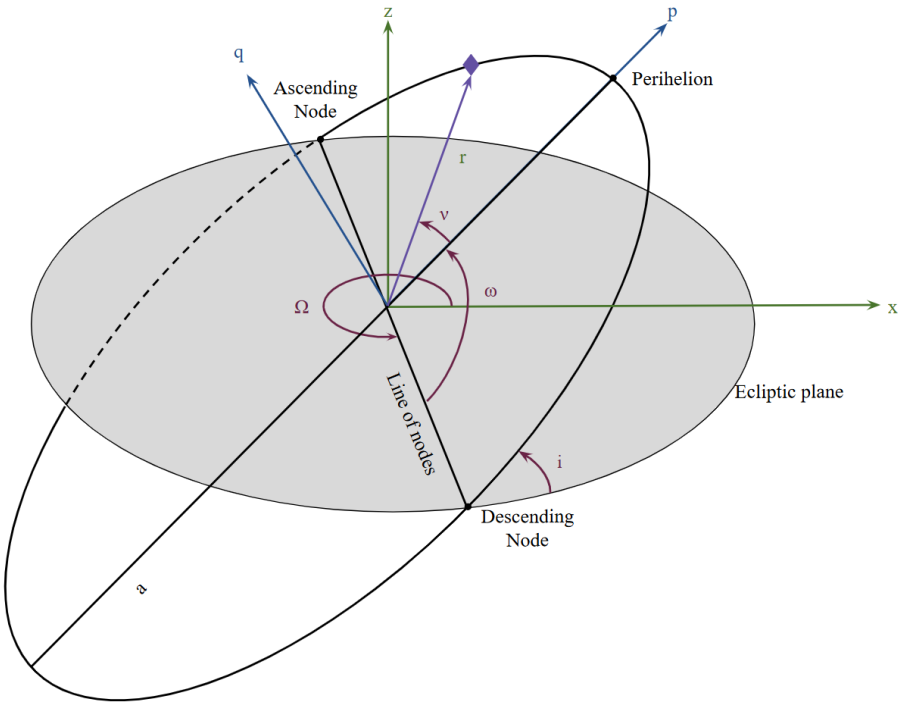

Figure 4.8: Orbital elements

Table 4.2: Classical orbital elements

Symbol	Name	Definition
a	Semi-major axis	Half of the longest diameter of the ellipse; determines the size of the orbit
e	Eccentricity	Measure of the orbit's deviation from a perfect circle ($e = 0$ for circular orbits)
i	Inclination	Angle between the orbital plane and the reference plane
Ω	Right Ascension of the Ascending Node (RAAN)	Angle from the reference direction (usually the vernal equinox) to the ascending node
ω	Argument of periapsis	Angle between the ascending node and the periapsis, measured in the orbital plane
ν	True anomaly	Angle between the direction of periapsis and the current position of the body along its orbit

Orbital elements, or Keplerian orbital parameters, are a set of values that determine the position of a body in space as it moves along a specific orbit. A minimum of six elements is required to

uniquely define the position in time. These parameters are defined with respect to the perifocal reference frame, as introduced in subsection 4.1.2. The classical orbital elements are listed in Table 4.2 and illustrated in Figure 4.8.

The semi-major axis a and the eccentricity e define the size and shape of the orbit. The inclination i, the RAAN Ω, and the argument of periapsis ω define the orientation of the orbit with respect to the reference frame. The true anomaly ν specifies the position of the body along the orbit. Under the assumptions of the two-body problem, where orbital perturbations are neglected, all the elements, except for the true anomaly, remain constant over time.
Although classical orbital elements are widely used, they may exhibit singularities when applied to certain types of orbits. In particular, singularities occur in the following cases:

- When the orbit lies on the fundamental plane the line of nodes cannot be defined, consequently the RAAN becomes undefined;
- When the orbit is circular, i.e., the eccentricity is zero $e = 0$, the line of apsides is not defined; the argument of periapsis becomes undefined;
- When both $i = 0$ and $e = 0$, the Ω, ω and ν are not distinguishable. In this case they can be combined to obtain the true longitude.

For this thesis the set or orbital elements employed in the code is:

- semi-major axis a;
- eccentricity e;
- argument of periapsis plus RAAN $\Omega + \omega$;
- time of passage from the periapsis t_p;
- inclination i;
- RAAN Ω.

While the asteroids are presented with a set of orbital parameters which are:

- semi-major axis a;
- eccentricity e;
- inclination i;
- argument of periapsis ω;
- RAAN Ω;
- mean anomaly M.

The mean anomaly M is defined as the angle measured between the direction of the periapsis and the position of a fictitious body moving along a circular orbit (with the same semi-major axis as the true orbit) reached in the same time as the body on the true elliptical orbit. The mean anomaly can be calculated as:

$$M = n(t - \tau) = E - e \cdot \sin E \tag{4.27}$$

Where E is the eccentric anomaly, $n = \sqrt{\mu/a^3}$ is the mean motion, t is the time, and τ is time of periapsis passage.

4.7 Interplanetary Missions: Patch Conics

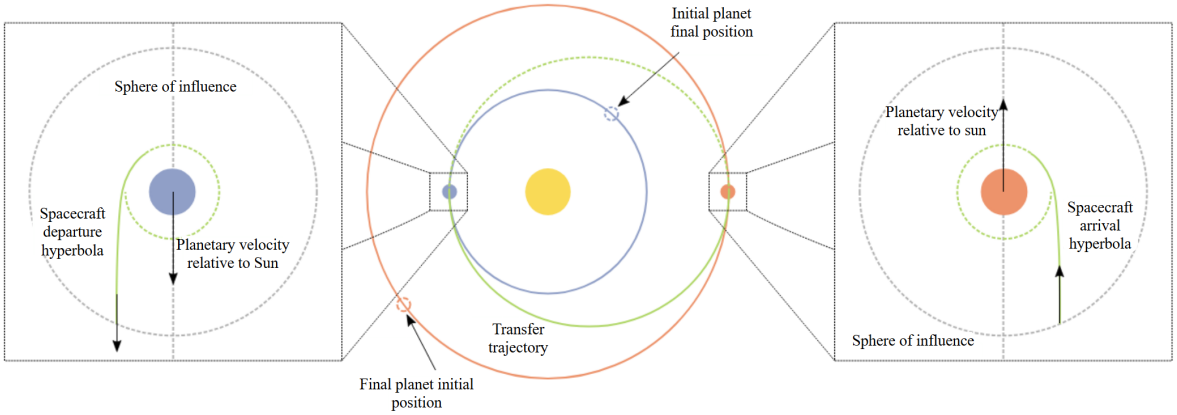

Figure 4.9: Patch conics diagram

An interplanetary mission is a transfer between two celestial bodies. The analysis of this problem requires accounting for gravitational influence of the three bodies involved: the departure body, the arrival body, and the spacecraft. This configuration makes the analysis of this type of problem complex. In order to simplify the study, it is possible to utilize the patch conics method to obtain a preliminary solution. This approach allows to divide the trajectory into three phases according to the sphere in which the spacecraft is located. A gravitational sphere of influence is a region of space where the error committed by neglecting the gravitational force of the Sun is smaller compared with neglecting the gravitational force exerted by the local body. This implies that inside a sphere of influence it is possible to neglect the gravitational forces exert by external celestial bodies. Following this reasoning, the interplanetary trajectory can be divided into three phases, illustrated in Figure 4.9:

- **Escape from the departure body**: the spacecraft follows a hyperbolic escape trajectory;
- **Heliocentric phase**: the spacecraft follows a interplanetary transfer trajectory between the departure and arrival bodies;
- **Arrival at the arrival planet**: the spacecraft approaches the arrival body on a hyperbolic trajectory.

This thesis focuses on the study of the trajectory during the heliocentric phase, considering the two-body problem of the spacecraft orbiting the Sun. The spacecraft departs from Earth and arrives at the designated asteroid.

Chapter 5

Solar Sail Equations

In this chapter, the equations of motion previously introduced in their general form will be derived for the specific case of a solar sail propelled spacecraft.

5.1 Motion Equations of the Sail

The equations of motion for the solar sail are derived by substituting the solar sail acceleration terms into the dynamic equations formulated for the two-body problem (Equation 4.24 ÷ 4.26) in the previous chapter. When using solar sailing, the thrust is entirely generated by the interaction of the solar radiation pressure with the sail surface. As a result, the thrust term T, typically associated with chemical or electric propulsion systems, is equal to zero. Additionally, since no propellant is consumed, the time variation of the spacecraft's mass is also equal to zero. Finally, as the considered mission is an interplanetary trajectory, aerodynamic forces can be neglected due to the absence of a significant atmosphere.
As introduced in chapter 1, solar sailing is a propulsion method that exploits the momentum transfer from solar radiation to produce thrust. When considering the two-body problem dynamic, solar radiation pressure is, usually, treated as a perturbing force. To model the motion of a solar sail propelled spacecraft, the acceleration produced by this force must be incorporated into the general two-body problem equation 4.12. The resulting formula is:

$$\ddot{\boldsymbol{r}} = -\frac{\mu}{r^3}\boldsymbol{r} + \boldsymbol{a}_p \tag{5.1}$$

Where $\boldsymbol{a}_p$ is the acceleration exerted by solar pressure, and it is given by:

$$\boldsymbol{a}_p = p\frac{S}{m} \tag{5.2}$$

Where p is the solar radiation pressure at a distance of 1 AU from the Sun, which is equal to $p_1 = 4.55682\,N/km^2$, S is the surface area exposed to the radiation, and m is the mass of the spacecraft. The new set of motion equations is given by:

$$\frac{\mathrm{d}\boldsymbol{r}}{\mathrm{d}t} = \boldsymbol{V} \tag{5.3}$$

$$\frac{\mathrm{d}\boldsymbol{V}}{\mathrm{d}t} = \boldsymbol{g} + \boldsymbol{a}_p \tag{5.4}$$

$$\frac{\mathrm{d}m}{\mathrm{d}t} = 0 \tag{5.5}$$

5.2 Solar sail orientation angles

In order to analyze how the acceleration induced by the solar radiation pressure contributes to the thrust in the three-dimensional space, it is necessary to define the orientation angles of the sail. The sail under consideration is assumed to be flat and its position can be described with two angles. These angle are defined with respect to the Ecliptic Plane, as illustrated in Figure 5.1:

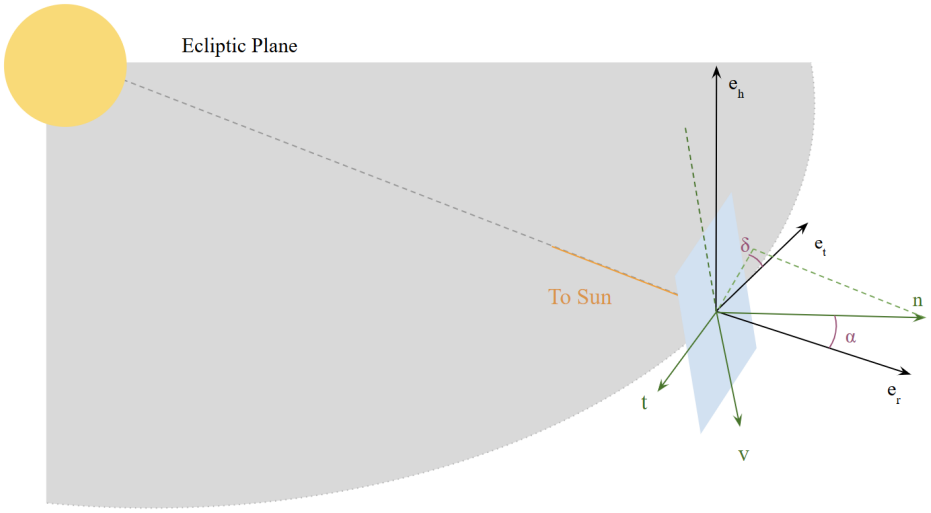

Figure 5.1: Solar sail orientation angles

- The **cone angle** α is defined as the angle between the normal to the sail and the direction of the Sun.
- The **clock angle** δ is the angle between the plane defined by the position vector and the normal to the sail and the reference plane of the Ecliptic.

The angles are considered positive when rotated in accordance with the Earth's motion on the Ecliptic Plane, which is counterclockwise. The admissible values of α and δ range from $-\pi/2$ to $\pi/2$.

5.3 Optical properties of the sail

A solar sail consists of a large reflective surface of light material. When solar radiation interacts with the sail, it generates thrust as a result of momentum transfer. The magnitude and direction of the generated thrust strongly depend on the sail's optical properties and the characteristics of the incident radiation flux. The incident momentum flux, associated with the radiation, is defined as the power flux divided by the speed of light, and is usually referred to as solar radiation pressure. When the incident radiation encounters the sail surface, the energy carried by the radiation is conserved and distributed among three components: a portion is transmitted through the sail, another is absorbed and re-emitted from both sides and the remaining part is reflected.

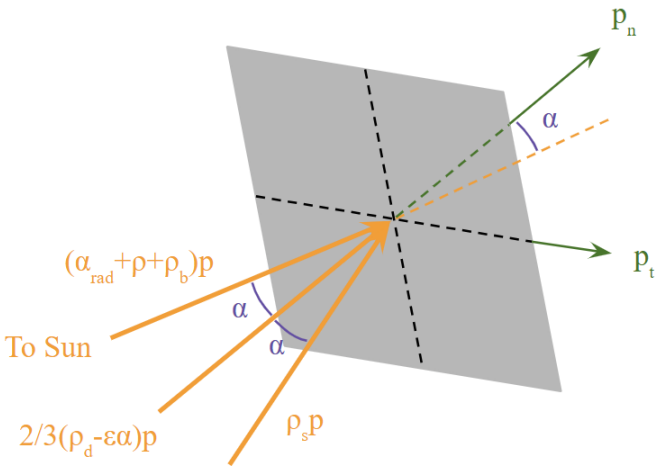

Figure 5.2: Radiation components on the sail

The distribution of the energy of the incident radiation among the transmitted, absorbed, and reflected components is defined by three optical properties of the sail material: transmittance τ, absorptance α_{rad} and reflectance ρ. Assuming energy conservation, the sum of these coefficients must equal 1:

$$\tau + \alpha_{rad} + \rho = 1 \tag{5.6}$$

The reflected radiation can be further divided into three components: specular reflection, backward reflection, and diffuse reflection. Each component is reflected according to a coefficient: ρ_s for specular reflectance, ρ_b for backward reflectance and ρ_d for diffuse reflectance, such that $\rho_s + \rho_b + \rho_d = \rho$. The portion of energy flux absorbed by the sail, αp, is re-emitted in accordance with the emittance coefficients on the front (ε_f) and back (ε_b) surfaces of the sail. The thrust acting on the sail is generated by the variation in momentum caused by the radiation.
The momentum transfer responsible for the thrust generation is calculated as the vector difference between the incident and emitted momentum fluxes. The transmitted portion of the incident flux, which is τp, results in zero net contribution to the force, as the momentum carried by the incoming and outgoing fluxes is equal. The remaining portion of the incident flux, composed of the absorbed and reflected components, is intercepted by the sail and exerts a radiation pressure equal to $(\alpha_{rad} + \rho)p$ in the direction of the incident light. The energy collected by the sail, as previously discussed, is either reflected or absorbed and then re-emitted by the sail, resulting in an additional contribution to the thrust, directed in the opposite direction. The back-reflected radiation produces a pressure force of magnitude $\rho_b p$ in the direction of the incident radiation. The specular reflection is rotated by an angle of 2α with respect to the sail-sun direction and the corresponding pressure on the sail $\rho_s p$ is rotated by the same angle away from the Sun-sail direction. For the diffuse component, the radiation pattern is assumed to be Lambertian, meaning the emitted flux is proportional to the cosine of the angle away from the surface normal. The resulting net radiation pressure force is equal to two-thirds ([67]) of the total diffuse reflected flux, i.e., $\rho_d p$, and it is directed along the sail normal. The same reasoning applies to the emitted component. In the most general case, the energy re-emitted from the front and rear sides of the sail is not equal. Assuming a Lambertian emission pattern, the net force along the normal to the front side of the sail is given by $\frac{2}{3}\varepsilon\alpha p$, where ε is defined as:

$$\varepsilon = \frac{\varepsilon_b - \varepsilon_f}{\varepsilon_b + \varepsilon_f} \tag{5.7}$$

The different contributes are represented in Figure 5.2. The net pressure exerted by the solar radiation on the sail can be divided into a component normal to the sail, given by:

$$p_n = p[(\rho + \alpha_{rad} + \rho_b + \rho_s)\cos(\alpha) + \frac{2}{3}(\rho_d - \varepsilon\alpha_{rad})] \tag{5.8}$$

and a component tangential to the sail surface, given by:

$$p_t = p(\rho + \alpha_{rad} + \rho_b + \rho_s)\sin(\alpha) \tag{5.9}$$

As illustrated in Figure 5.2. With the aim of simplifying Equations 5.8 and 5.9, three new coefficients are introduced:

$$\omega = \rho + \alpha_{rad} + \rho_b \qquad \eta = \frac{\rho_s}{\omega} \qquad \delta_{rad} = \frac{2}{3}\frac{\rho_d - \epsilon\alpha_{rad}}{\omega} \tag{5.10}$$

These terms allow the equations to be rewritten in the form:

$$p_n = \omega p\left[(1+\eta)\cos(\alpha) + \delta_{\text{rad}}\right] \tag{5.11}$$

$$p_t = \omega p(1-\eta)\sin(\alpha) \tag{5.12}$$

The forces exerted on the sail by the solar pressure are defined in the local reference frame as:

$$F_u = F_n \tag{5.13}$$

$$F_v = F_t\cos(\delta) \tag{5.14}$$

$$F_w = F_t\sin(\delta) \tag{5.15}$$

Where F_r and F_t represent the forces acting in the normal and tangential directions. When the normal to the sail is rotated by an angle α with respect to the Sun-sail direction, the surface area of the sail exposed to the radiation is reduced and becomes equal to $A\cos\alpha$. Thus, the forces are expressed as:

$$F_n = A\cos(\alpha)p_n \qquad F_n = A\cos(\alpha)p_t \tag{5.16}$$

By applying the fundamental law of dynamics, $F = ma$, the accelerations in the local frame are given by:

$$a_u = \frac{A}{m}\cos(\alpha)\left(p_n\cos(\alpha) + p_t\sin(\alpha)\right) \tag{5.17}$$

$$a_v = \frac{A}{m}\cos(\alpha)\cos(\delta)\left(p_n\sin(\alpha) - p_t\cos(\alpha)\right) \tag{5.18}$$

$$a_w = \frac{A}{m}\cos(\alpha)\sin(\delta)\left(p_n\sin(\alpha) - p_t\cos(\alpha)\right) \tag{5.19}$$

Where m is the total mass of the spacecraft.
The characteristic acceleration of the sail is defined as the acceleration produced when a perfectly reflective sail is oriented normal to the direction of sunlight, i.e., $\alpha = 0$, at a distance of 1 AU from the Sun. A perfectly reflective sail is characterized by the following optical properties: $\alpha_{rad} = \tau = 0, \rho_s = \rho = 1$. The characteristic acceleration is expressed as:

$$a_c = \frac{2p_1 A}{m} \tag{5.20}$$

By rearranging the terms and by substituting the definition of characteristic acceleration, the sail accelerations in their adimensional form are given by:

$$a_u = \omega\frac{a_c}{2r^2}\cos(\alpha)\left(1 + \eta\cos(2\alpha) + \delta_{\text{rad}}\cos(\alpha)\right) \tag{5.21}$$

$$a_v = \omega\frac{a_c}{2r^2}\cos(\alpha)\cos(\delta)\left(\eta\sin(2\alpha) + \delta_{\text{rad}}\sin(\alpha)\right) \tag{5.22}$$

$$a_w = \omega\frac{a_c}{2r^2}\cos(\alpha)\sin(\delta)\left(\eta\sin(2\alpha) + \delta_{\text{rad}}\sin(\alpha)\right) \tag{5.23}$$

5.4 Non-dimensionalization Parameters

The problem variables are non-dimensionalised using reference values based on Earth's characteristics. Distances are scaled with respect to the Earth's average distance from the Sun, i.e., the astronomical unit (AU):

$$r_{conv} = r_{\oplus} = 1.49597870691 \cdot 10^8 \, km \tag{5.24}$$

Velocities are scaled with respect to the Earth's mean orbital velocity, or circular velocity, around the Sun:

$$v_{conv} = v_{\oplus} = \sqrt{\frac{\mu_{\odot}}{r_{\oplus}}} = \sqrt{\frac{1.32712440018 \cdot 10^{11} \, km^3/s^2}{1.49597870691 \cdot \, 10^8 km}} = 29.58 \, km/s \tag{5.25}$$

Accelerations are scaled with respect to the Sun's gravitational acceleration at 1 AU, which is the centripetal acceleration corresponding to Earth's circular motion:

$$a_{conv} = a_{\oplus} = \frac{\mu_{\odot}}{r_{\oplus}^2} = \frac{1.32712440018 \cdot 10^{11} \, km^3/s^2}{(1.49597870691 \cdot 10^8 \, km)^2} = 5.93 \cdot 10^{-6} \, km/s^2 \tag{5.26}$$

Finally, time is non-dimensionalized with respect to the sidereal year, defined as the time required for Earth to complete a full orbit around the Sun relative to the fixed stars:

$$t_{conv} = \frac{v_{conv}}{a_{conv} \cdot 86400} = \frac{365 \, days}{2\pi} = 58.13244088 \, days \tag{5.27}$$

The time is measured starting from J2000.

5.5 Dimensionless form of the motion equations

The motion equations in dimensionless and extended form are:

$$\frac{dr}{dt} = u \tag{5.28}$$

$$\frac{d\vartheta}{dt} = \frac{v}{r} \frac{1}{\cos\varphi} \tag{5.29}$$

$$\frac{d\varphi}{dt} = \frac{w}{r} \tag{5.30}$$

$$\frac{du}{dt} = -\frac{1}{r^2} + \frac{v^2}{r} + \frac{w^2}{r} + a_u \tag{5.31}$$

$$\frac{dv}{dt} = -\frac{uv}{r} + \frac{vw}{r} \tan\varphi + a_v \tag{5.32}$$

$$\frac{dw}{dt} = -\frac{uw}{r} - \frac{v^2}{r} \tan\varphi + a_w \tag{5.33}$$

$$\frac{dm}{dt} = 0 \tag{5.34}$$

The dimensionless form of the sail accelerations, previously presented in Equations (5.21), (5.22), and (5.23), is derived by applying the non-dimensional definition of the characteristic acceleration and by substituting the normal (Equation 5.8) and tangential (Equation 5.9)

components of the radiation pressure, as explained in Appendix A:

$$a_u = \omega \frac{a_c}{2r^2} \cos(\alpha) \left(1 + \eta \cos(2\alpha) + \delta_{\text{rad}} \cos(\alpha)\right) \tag{5.35}$$

$$a_v = \omega \frac{a_c}{2r^2} \cos(\alpha) \cos(\delta) \left(\eta \sin(2\alpha) + \delta_{\text{rad}} \sin(\alpha)\right) \tag{5.36}$$

$$a_w = \omega \frac{a_c}{2r^2} \cos(\alpha) \sin(\delta) \left(\eta \sin(2\alpha) + \delta_{\text{rad}} \sin(\alpha)\right) \tag{5.37}$$

By substituting the dimensionless form of the accelerations into the equations of motion, the following expressions are obtained:

$$\frac{dr}{dt} = u \tag{5.38}$$

$$\frac{d\vartheta}{dt} = \frac{v}{r} \frac{1}{\cos\varphi} \tag{5.39}$$

$$\frac{d\varphi}{dt} = \frac{w}{r} \tag{5.40}$$

$$\frac{du}{dt} = \frac{a_c}{2r^2} cos(\alpha)(1 + \eta \cos(2\alpha) + \delta_{rad} \cos(\alpha)) - \frac{1}{r^2} + \frac{v^2}{r} + \frac{w^2}{r} \tag{5.41}$$

$$\frac{dv}{dt} = \frac{a_c}{2r^2} cos(\alpha) \cos(\delta)(\eta \sin(2\alpha) + \delta_{rad} \sin(\alpha)) - \frac{uv}{r} + \frac{vw}{r} \tan\varphi \tag{5.42}$$

$$\frac{dw}{dt} = \frac{a_c}{2r^2} cos(\alpha) \sin(\delta)(\eta \sin(2\alpha) + \delta_{rad} \sin(\alpha)) - \frac{uw}{r} - \frac{v^2}{r} \tan\varphi \tag{5.43}$$

$$\frac{dm}{dt} = 0 \tag{5.44}$$

The analysis is carried out by considering the simplified case with $\omega = 1$ and $\delta_{rad} = 0$. The simplified motion equations are given by:

$$\frac{dr}{dt} = u \tag{5.45}$$

$$\frac{d\vartheta}{dt} = \frac{v}{r} \frac{1}{\cos\varphi} \tag{5.46}$$

$$\frac{d\varphi}{dt} = \frac{w}{r} \tag{5.47}$$

$$\frac{du}{dt} = \frac{a_c}{2r^2} cos(\alpha)(1 + \eta \cos(2\alpha)) - \frac{1}{r^2} + \frac{v^2}{r} + \frac{w^2}{r} \tag{5.48}$$

$$\frac{dv}{dt} = \frac{a_c}{2r^2} cos(\alpha) \cos(\delta)(\eta \sin(2\alpha)) - \frac{uv}{r} + \frac{vw}{r} \tan\varphi \tag{5.49}$$

$$\frac{dw}{dt} = \frac{a_c}{2r^2} cos(\alpha) \sin(\delta)(\eta \sin(2\alpha)) - \frac{uw}{r} - \frac{v^2}{r} \tan\varphi \tag{5.50}$$

$$\frac{dm}{dt} = 0 \tag{5.51}$$

5.6 Trajectory Optimization

Trajectory optimization is performed using optimal control theory, as described in chapter 3. In this case, the objective of the optimization procedure is to minimize the trip time of the mission. The problem is reformulated as a maximization problem by introducing a new time-related

performance index $\phi = -t_f$. According to Pontryagin's Maximum Principle, the control value that optimizes the trajectory at each point is the one that maximizes the Hamiltonian H. The Hamiltonian was previously defined in Equation 3.11. An adjoint variable is associated with each state variable and the Hamiltonian is rewritten for the problem as:

$$H = \lambda_r u + \lambda_\varphi \frac{w}{r} + \frac{\lambda_u}{r}(-\frac{1}{r} + v^2 + w^2) + \frac{\lambda_v}{r}(-uv + vw\tan(\varphi)) + \\ + \frac{\lambda_w}{r}(-uw - v^2\tan(\varphi)) + \lambda_\vartheta \frac{v}{r\cos(\varphi)} + \lambda_u a_u + \lambda_v a_v + \lambda_w a_w \tag{5.52}$$

The acceleration terms are the ones that include the control variables α and δ. The terms λ_u, λ_v and λ_w are the adjoint variables to the velocity components in the radial direction, eastward, and northern direction, respectively. These are the components of the primer vector $\boldsymbol{\lambda}_V$, which is the adjoint variable associated with the spacecraft's velocity vector $\boldsymbol{V}$. Finding the maximum value of Equation 5.52 with respect to the control variables is equivalent to maximizing the dot product $\boldsymbol{\lambda}_V \cdot \boldsymbol{a}$ between the primer vector and the sail acceleration. The differential equations for the adjoint variables, in the simplified case $\omega = 1$ and $\delta_{rad} = 0$, are obtained from the Euler-Lagrange Equation (3.12), defined in chapter 3:

$$\frac{d\lambda_r}{dt} = -\frac{\partial H}{\partial r} = \left(\frac{\lambda_\vartheta v}{r\cos\varphi} + \lambda_\varphi \frac{w}{r} - \lambda_u\left(\frac{2}{r^2} - \frac{v^2}{r} - \frac{w^2}{r}\right) - \lambda_v\left(\frac{uv}{r} - \frac{vw}{r}\tan\varphi\right)\right. \\ \left. -\lambda_w\left(\frac{uw}{r} + \frac{v^2}{r}\tan\varphi\right)\right)\frac{1}{r} + 2\frac{\lambda_u a_u + \lambda_v a_v + \lambda_w a_w}{r} \tag{5.53}$$

$$\frac{d\lambda_\vartheta}{dt} = -\frac{\partial H}{\partial \vartheta} = 0 \tag{5.54}$$

$$\frac{d\lambda_\varphi}{dt} = -\frac{\partial H}{\partial \varphi} = \frac{v}{(\cos\varphi)^2}\left(\lambda_w\frac{v}{r} - \lambda_v\frac{w}{r} - \frac{\lambda_\vartheta}{r}\sin\varphi\right) \tag{5.55}$$

$$\frac{d\lambda_u}{dt} = -\frac{\partial H}{\partial u} = \lambda_u\frac{v}{r} + \lambda_v\frac{w}{r} - \lambda_r \tag{5.56}$$

$$\frac{d\lambda_v}{dt} = -\frac{\partial H}{\partial v} = \lambda_v\left(\frac{u}{r} - \frac{w}{r}\tan\varphi\right) - \frac{2v}{r}\left(\lambda_u - \lambda_w\tan\varphi\right) - \frac{\lambda_\vartheta}{r\cos\varphi} \tag{5.57}$$

$$\frac{d\lambda_w}{dt} = -\frac{\partial H}{\partial w} = \lambda_w\frac{u}{r} - \frac{\lambda_\varphi}{r} - 2\lambda_u\frac{w}{r} - \lambda_v\frac{v}{r}\tan\varphi \tag{5.58}$$

$$\frac{d\lambda_m}{dt} = -\frac{\partial H}{\partial m} = 0 \tag{5.59}$$

The application of optimal control theory leads to a BVP involving the state and adjoint variables. As previously discussed in chapter 3, this BVP is solved using a numerical approach based on Newton's method.

5.7 Optimal Control Law

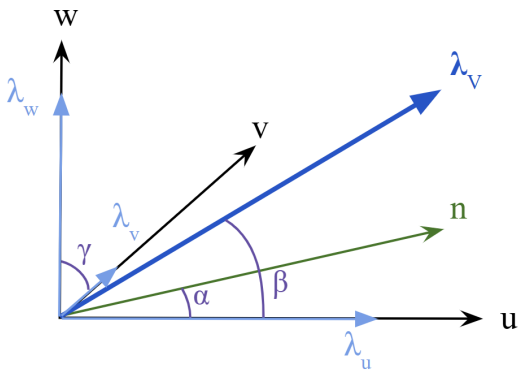

Figure 5.3: Definition of γ and β angles

In order to characterize the orientation of the adjoint variables to the velocity vector, two angles are introduced, as illustrated in Figure 5.3. The angle γ is defined as the angle between the vectors λ_w and λ_v and is given by:

$$\gamma = atan2(\lambda_w, \lambda_v) \tag{5.60}$$

The angle β is defined as the angle between the primer vector $\boldsymbol{\lambda}_V$ and the normal direction to the sail $\boldsymbol{n}$ and is given by:

$$\beta = atan2(\sqrt{\lambda_v^2 + \lambda_w^2}, \lambda_u) \tag{5.61}$$

The admissible values of β range from $-\pi$ to π. Both angles are considered positive when measured counterclockwise, in accordance with the direction of Earth's motion on the Ecliptic Plane. This convention is consistent with that adopted for the definition of the control angles of the sail α and δ. The angles are defined such that the components of the primer vector can be expressed as follows:

$$\lambda_u = \boldsymbol{\lambda}_V \cos(\beta) \tag{5.62}$$
$$\lambda_v = \boldsymbol{\lambda}_V \sin(\beta)\cos(\gamma) \tag{5.63}$$
$$\lambda_w = \boldsymbol{\lambda}_V \sin(\beta)\sin(\gamma) \tag{5.64}$$

By adopting the new definition for the components of the primer vector, given in Equations 5.62, 5.63 and 5.64, and by considering the simplified case with $\omega = 1$ and $\delta_{rad} = 0$, the Hamiltonian can be reformulated as:

$$H = \lambda_r u + \lambda_\varphi \frac{w}{r} + \lambda_\vartheta \frac{v}{r\cos(\varphi)} + \frac{\lambda_u}{r}(-\frac{1}{r} + v^2 + w^2) + \frac{\lambda_v}{r}(-uv + vw\tan(\varphi)) + \\ + \frac{\lambda_w}{r}(-uw - v^2\tan(\varphi)) + \lambda_V \frac{a_c}{2r^2} H' \tag{5.65}$$

Where H' is defined as:

$$H' = \cos(\alpha)[\cos(\beta)(1 + \eta\cos(2\alpha)) + \cos(\delta)\sin(\beta)\cos(\gamma)\eta\sin(2\alpha) + \\ + \sin(\delta)\sin(\beta)\sin(\gamma)\eta\sin(2\alpha)] \tag{5.66}$$

It is important to note that $H'(\alpha, \delta, \beta, \gamma) = H'(-\alpha, -\delta, -\beta, -\gamma)$, therefore the analysis is carried out assuming positive values of β, but the extension to negative angles is straightforward. Since H' contains all the terms involving the control variables, the maximization of the Hamiltonian H with respect to these variables is equivalent to maximizing the simpler function H'. The local maxima of H' are found by setting its partial derivatives with respect to the control angles, α and δ, equal to zero. This procedure is detailed in Appendix B and leads to the following expression:

$$\sin(\beta - 2\alpha) = \frac{\frac{1-\eta}{\eta}\cos(\beta)\tan(\alpha) + \sin(\beta)}{3} \tag{5.67}$$

By isolating α in Equation 5.67, the expression for α can be derived:

$$\alpha = \frac{1}{2}[\beta - \sin^{-1}((\frac{1-\eta}{3\eta})\cos(\beta)\tan(\alpha)) + \frac{\sin(\beta)}{3})] \tag{5.68}$$

In the simplified case of unit reflectivity (i.e. $\eta = 1$, $\delta_{rad} = 0$), the expression assumes a significant form:

$$\alpha = \frac{1}{2}[\beta - \sin^{-1}(\frac{\sin(\beta)}{3})] \tag{5.69}$$

This corresponds to the global maximum of the Hamiltonian. In the other cases. Equation 5.67 can be numerically solved using Newton's method, as described in chapter 3, using the value of Equation 5.69 as the starting point.

5.8 Boundary Conditions

The boundary conditions complete the BVP definition. The total number of boundary conditions must be equal to the dimension of the problem, which is 17 [section 6.1] for a single-phase mission. As introduced in chapter 3, these conditions can be either explicit or implicit. Explicit boundary conditions are directly specified, while implicit boundary conditions are evaluated through associated error functions. A solution is considered valid when all errors associated with the implicit boundary conditions are below a tolerance value, set to 10^{-6}.
The explicit boundary conditions are related to the mass. The first condition is imposed on the adjoint variable associated with the mass, which is set to one:

$$\lambda_{m_0} = 1 \tag{5.70}$$

The second one on the initial mass:

$$m_0 = m_{\text{inital}} \tag{5.71}$$

At the departure (t_0) and arrival (t_f) times, boundary conditions are imposed on the position vector $\boldsymbol{r} = [r, \vartheta, \varphi]$ and the velocity vector $\boldsymbol{V} = [u, v, w]$, requiring that these variables match the corresponding values of the departure and arrival bodies, respectively:

$$\boldsymbol{r}(t_0) = \boldsymbol{r}_{\oplus}(t_0) \tag{5.72}$$
$$\boldsymbol{V}(t_0) = \boldsymbol{V}_{\oplus}(t_0) \tag{5.73}$$
$$\boldsymbol{r}(t_f) = \boldsymbol{r}_{Asteroid}(t_f) \tag{5.74}$$
$$\boldsymbol{V}(t_f) = \boldsymbol{V}_{Asteroid}(t_f) \tag{5.75}$$
$$\tag{5.76}$$

The corresponding errors associated with these boundary conditions are defined as follows:

$$\text{err}_1 = r_0 - r_\oplus \tag{5.77}$$
$$\text{err}_2 = \vartheta_0 - \vartheta_\oplus \tag{5.78}$$
$$\text{err}_3 = \varphi_0 - \varphi_\oplus \tag{5.79}$$
$$\text{err}_4 = u_0 - u_\oplus - \frac{\lambda_u}{\lambda_V} V_\infty \tag{5.80}$$
$$\text{err}_5 = v_0 - v_\oplus - \frac{\lambda_v}{\lambda_V} V_\infty \tag{5.81}$$
$$\text{err}_6 = w_0 - w_\oplus - \frac{\lambda_w}{\lambda_V} V_\infty \tag{5.82}$$
$$\text{err}_7 = r_f - r_\oplus \tag{5.83}$$
$$\text{err}_8 = \vartheta_f - \vartheta_\oplus \tag{5.84}$$
$$\text{err}_9 = \varphi_f - \varphi_\oplus \tag{5.85}$$
$$\text{err}_{10} = u_f - u_\oplus \tag{5.86}$$
$$\text{err}_{11} = v_f - v_\oplus \tag{5.87}$$
$$\text{err}_{12} = w_f - w_\oplus \tag{5.88}$$
$$\tag{5.89}$$

A boundary condition is also imposed on the initial time, which must be equal to the assigned departure time:

$$\text{err}_{13} = t_{0_{\text{assigned}}} - t_0 \tag{5.90}$$
$$\tag{5.91}$$

The spacecraft leaves the Earth with zero hyperbolic excess velocity ($v_\infty = 0$). Therefore a condition is set for this quantity:

$$\text{err}_{15} = \frac{V_\infty}{V_{\text{conv}}} - V_\infty \tag{5.92}$$

Finally, the transversality condition, $H_f = 1$, defines an additional relation between the state variables, the adjoint variables, and the time. This condition arises from the application of the Pontryagin Maximum Principle and is necessary to fully specify the system of equations. The corresponding error is given by:

$$\text{err}_{14} = 1 - H_f \tag{5.93}$$

Chapter 6

Implementation of the Indirect Iterative Method

The indirect iterative method used for trajectory optimization is implemented in a FORTRAN code that will be briefly presented in this chapter. The code takes as inputs various data, including iteration settings, sail characteristics, the orbital elements of the departure and arrival bodies and the initial trial solution. The output consists of the errors on the boundary conditions, the arrival time and the final values of the parameters.

6.1 Vectors

The code employs different vectors to manage the variables involved in the optimization problem. The dimension of the problem, given by *N*=17 , can be determined in two equivalent ways: by summing the number of unknown terms K and the known variable λ_m, or by summing the number of problem variables N_Y*=13* and the number of constant parameters K_P*=4*:

$$N = K + 1 = N_Y + K_P \tag{6.1}$$

The values of these terms are contained in two vectors:

- *S*, which contains the problem variables;
- K_P, which contains the problem constants.

These vectors are defined as follows:

$$S = [r, \vartheta, \varphi, u, v, w, \lambda_r, \lambda_\varphi, \lambda_u, \lambda_v, \lambda_w, m, \lambda_m] \tag{6.2}$$

$$K_P = [t_0, t_f, \lambda_\vartheta, V_{\infty_0}] \tag{6.3}$$

6.2 Code

This section briefly describes the functioning of the code that implements the indirect method for trajectory optimization.
The user is prompted to enter the values of three parameters required to perform the iteration: `rmin`, `pbis` and `jmax`. These values were defined in chapter 3, during the explanation of the numerical method used to solve the problem. The variable `rmin` represents the iteration

step Δp; `pbis` is the multiplier K_2 introduced to prevent the iteration from diverging; and `jmax` defines the maximum number of iterations allowed. The values for `rmin` typically range between 0.0001 and 0.1. This parameter is initially set to 0.1; if convergence is not achieved, the value can be reduced accordingly. The value of `pbis` is set to 2, in accordance with the value assigned in chapter 3. The maximum number of iterations is set in the range of 2000 to 5000, ensuring a sufficient number of steps to reach convergence, without increasing the computational time. After defining the iteration parameters, the user must select the initial time `t0`, and the sail parameters: characteristic acceleration `acc` and η `eta`. The values are automatically set to `t0`=169, `acc=0.5` and `eta`=1, and can be modified manually. The trial solution is stored in an external file, which can be manually edited. This document contains:

- The number of phases considered for the mission, in this case only one;
- The values of the constant parameters: initial time `t0`, final time `tf`, and λ_ϑ;
- The unknown problem variables: $[v_{\infty_0}, r_0, \vartheta_0, \varphi_0, u_0, v_0, w_0, \lambda_{r_0}, \lambda_{\varphi_0}, \lambda_{u_0}, \lambda_{v_0}, \lambda_{w_0}, m_0]$.

After the trial solution is read, the user selects the departure and arrival bodies and their orbital parameters are retrieved. The orbital parameters for Earth are in the format: semi-major axis a, eccentricity e, inclination i, argument of periapsis ω, RAAN Ω and mean anomaly M. The angles are given in degrees. Since the orbital elements provided for asteroids are in a different format, they must be reprocessed to be consistent with the others. The boundary conditions are declared according to the formulas given in section 5.8. Once all the information are inserted, the numerical computation begins. The output consists of a number that indicates the result of the process (-4 when convergence is reached), the duration in non-dimensional time, the duration in days and the dates in the format day/month/year of the departure and arrival time. Data on the trajectory are provided in external files, which contain the time evolution of the problem variables, the control angles, α and β, and the orbital parameters. A flow chart of the process is illustrated in Figure 6.1.
The numerical solution is explored for different scenarios by progressively updating the boundary conditions as needed.

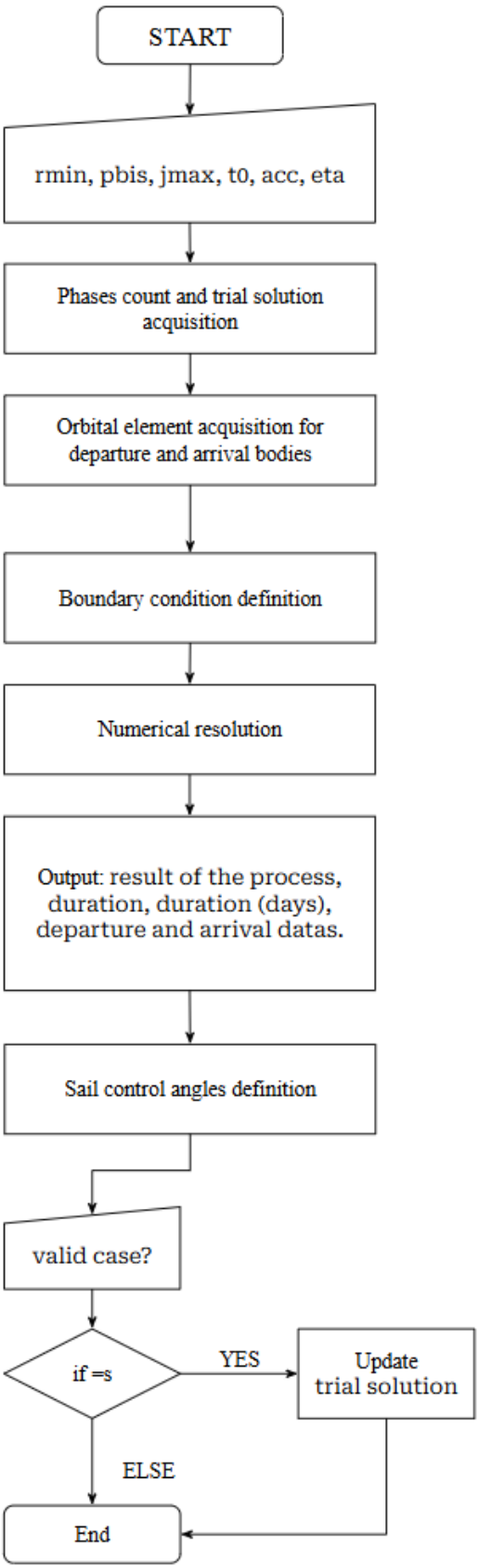

Figure 6.1: Flow Chart

Chapter 7

Results

In this chapter, the numerical results obtained with the indirect mathematical method are discussed. As anticipated in chapter 5, the trajectory optimization problem for a solar sail propelled spacecraft consists of minimizing the trip time of the mission.

The analysis is influenced by the three input parameters: departure time, characteristic acceleration, and η. The impact of each parameter on the mission duration is investigated. The analysis is repeated for the different asteroids presented in section 2.5.

7.1 2000 SG344

7.1.1 Effect of the variation of departure time on the solution

Table 7.1: Numerical results for departure times spaced one year apart, with fixed a_c and η

Departure time [adim]	**acc** $[mm/s^2]$	η	**Trip time [adim]**	**Trip time [days]**	θ_0 $[rad]$	$\Delta\theta$ $[rad]$
169	0.05	1	22.8071970260806	1325.83803246170	1.0766	16.8642
175	0.05	1	22.3097187815600	1296.91840782947	0.7871	16.6362
181	0.05	1	21.7962797288754	1267.07094246044	0.4999	16.3850
187	0.05	1	21.2810852201463	1237.12142814672	0.2153	16.1025
193	0.05	1	20.7884535311409	1208.48354561639	6.2165	15.7979
199	0.05	1	20.3303568829652	1181.85326930492	5.9371	15.4849
205	0.05	1	19.8967432817405	1156.64625227257	5.6599	15.1701
211	0.05	1	19.4601612635067	1131.26667391398	5.3843	14.8453
217	0.05	1	18.9796227172887	1103.33179529163	5.1099	14.4908
223	0.05	1	18.4075054487068	1070.07322200678	4.8359	14.0847
229	0.05	1	17.7303327079503	1030.70751769797	4.5610	13.6356
235	0.05	1	17.0566791840664	991.546394055919	4.2865	13.2286

To investigate the relationship between departure time and transfer duration, the solution is searched starting from departure time 169, which corresponds to the 24/11/2026, while maintaining characteristic acceleration and η constant ($a_c = 0.05 \quad mm/s^2$, $\eta = 1$). From this starting point, the transfer duration is searched multiple times by increasing the departure date by one year each time. Numerical results are displayed in Table 7.1.

The numerical results show a progressive decrease in the transfer duration. Upon further analysis, the minimum trip time is reached for a departure time of 352, corresponding to 7 March 2056. However, this date is considered too far in the future for the current mission scenario. Therefore, the analysis focuses on departure times between 199 (3 September 2031) and 229 (12 June 2036). To complete the study, additional results are computed at shorter intervals within this range. Numerical results are presented in Table 7.2, with the shortest trip times for each year emphasized in bold for clarity.

Results from Table 7.2 are summarized in Figure 7.1. The graph shows a sinusoidal trend in transfer duration, which tends to decrease over time. This behaviour can be attributed to the variation in the phase angle between the departure body (Earth) and the arrival body (asteroid). The phase angle is defined as the angle between the arrival and the departure bodies at the moment of launch. This angle governs the relative positioning of the celestial bodies and is directly related to the trajectory length and, consequently, to the transfer duration. Evaluating the effects of this parameter is of fundamental importance to properly program an interplanetary mission. Anticipating the departure makes it necessary for the spacecraft to rotate slower in order to achieve the correct phasing for the rendezvous. This is accomplished by increasing the semi-major axis, placing the spacecraft on a higher trajectory where its orbital speed is lower. The more the semi-major axis needs to be increased, the more orbits are required to insert the spacecraft into the correct trajectory, early departure times require a higher $\Delta\theta$, progressively increasing the mission duration. This phenomenon can be also observed in the trajectory plots of the missions presented for asteroid 2000 SG344. The sinusoidal trend is also a consequence of the variation of the phase angle, each year it can be observed a maximum value and a minimum value for the trip time, where the conditions for beginning of the mission are respectively the worst and the best.

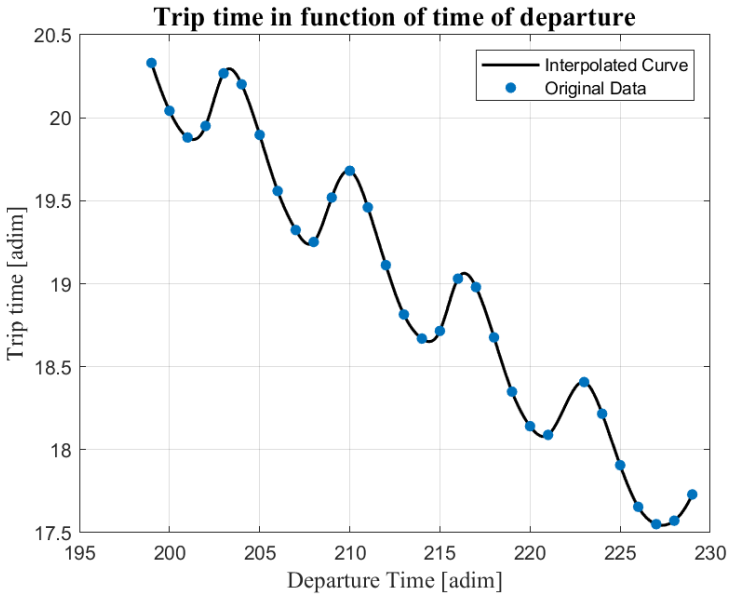

Figure 7.1: Numerical results for mission from 199 to 299

Table 7.2: Detailed mission data from day 199 to 229 with fixed acceleration and η

Departure time [adim]	**acc** $[mm/s^2]$	η	**Trip time [adim]**	**Trip time [days]**	θ_0 $[rad]$	$\Delta\theta$ $[rad]$
199	0.05	1	20.3303568829652	1181.85326930492	5.9371	15.4849
200	0.05	1	20.0417320614891	1165.07480393769	0.7871	16.6362
201	**0.05**	**1**	**19.8811932776096**	**1155.74229257695**	**0.4999**	**16.3850**
202	0.05	1	19.9505390870986	1159.77353374645	0.2153	16.1025
203	0.05	1	20.2675163508686	1178.20019578876	6.2165	15.7979
204	0.05	1	20.2017315125360	1174.37596256444	5.9371	15.4849
205	0.05	1	19.8967425508128	1156.64620978197	5.6599	15.1701
206	0.05	1	19.5587358614379	1136.99705589921	1.6784	15.0836
207	0.05	1	19.3235148744581	1123.32308578292	2.7084	15.0360
208	**0.05**	**1**	**19.2515641086020**	**1119.14041214145**	**3.7137**	**15.2833**
209	0.05	1	19.5192441856680	1134.70130839278	4.6904	15.3227
210	0.05	1	19.6805623225524	1144.07912544599	5.6599	15.1701
211	0.05	1	19.4601611277152	1131.26666602009	5.3843	14.8453
212	0.05	1	19.1121183018841	1111.03408702827	1.3858	14.7572
213	0.05	1	18.8146590875785	1093.74205684229	2.4182	14.6234
214	**0.05**	**1**	**18.6694238151141**	**1085.29917595394**	**3.4323**	**14.7682**
215	0.05	1	18.7156317355361	1087.98535515546	4.4157	14.9379
216	0.05	1	19.0302842353931	1106.27687299707	5.3843	14.8453
217	0.05	1	18.9796208785654	1103.33168840216	5.1099	14.4908
218	0.05	1	18.6767007838427	1085.72220390825	1.0944	14.4299
219	0.05	1	18.3494184030204	1066.69648025827	2.1265	14.2919
220	0.05	1	18.1415276091142	1054.61128097471	3.1483	14.2526
221	**0.05**	**1**	**18.0890826254074**	**1051.56252606061**	**4.1398**	**14.4781**
223	0.05	1	18.4075031177109	1070.07308650030	4.8359	14.0847
224	0.05	1	18.2164794208666	1058.96841273929	6.0851	14.3145
225	0.05	1	17.9064283279826	1040.94438591645	0.8048	14.1065
226	0.05	1	17.6557249370665	1026.37038586885	1.8338	13.9680
227	**0.05**	**1**	**17.5511532808677**	**1020.29138024850**	**2.8616**	**13.8934**
228	0.05	1	17.5720441008606	1021.50581460641	4.8359	14.0847
229	0.05	1	17.7303421715814	1030.70806784195	4.5610	13.6356

In the considered time interval for the departure of the mission the best option is to start the mission on 17 February 2036, which corresponds to 277. In this case, the trip time wold be around 1020 days, guaranteeing the arrival on the asteroid for the 3 December 2038. This mission would last almost 3 years. The same condition will occur again after a synodic period has passed. A synodic period is the time interval it passes before the departure and arrival bodies find each other in the same relative position. It can be calculated as:

$$\tau = \frac{2\pi}{|\omega_{\oplus} - \omega_{asteroid}|} \qquad \omega = \sqrt{\frac{1}{a^3}} \tag{7.1}$$

For Earth and asteroid 2000 SG344 $\tau = 180.4113$, measured in non-dimensional time.

7.2 Effect of the variation of the parameter η on the solution

The parameter η is defined in chapter 5 as a function of various optical properties of the sail:

$$\eta = f(\rho_s, \rho, \alpha_{rad}, \rho_b) \tag{7.2}$$

In the simplified case considered for the formulation of the equations (i.e., $\omega = 1$, $\delta_{rad} = 0$), η is equal to the specular reflectance coefficient ρ_s. This index can therefore be interpreted as an efficiency parameter for the reflectivity of the sail. To assess the influence of η on the solution, a set of simulations is carried out by varying η, while keeping the characteristic acceleration and the departure time constant. The chosen departure time is the one that guarantees the minimum trip time among the cases presented in the previous paragraph, i.e., 227. The characteristic acceleration is kept equal to the trial value of 0.05. Numerical results for cases with η ranging from 1 to 0.5 are presented in Table 7.3. For improved visualization, the non-dimensional trip time is plotted as a function of η in Figure 7.2.
From the numerical results, it is clear that a decrease in the parameter η, representing the specular reflectance coefficient of the sail, leads to an increase in the trip duration. This outcome is intuitive, as a lower reflectivity results in a reduced momentum variation and, consequently, a lower thrust magnitude.

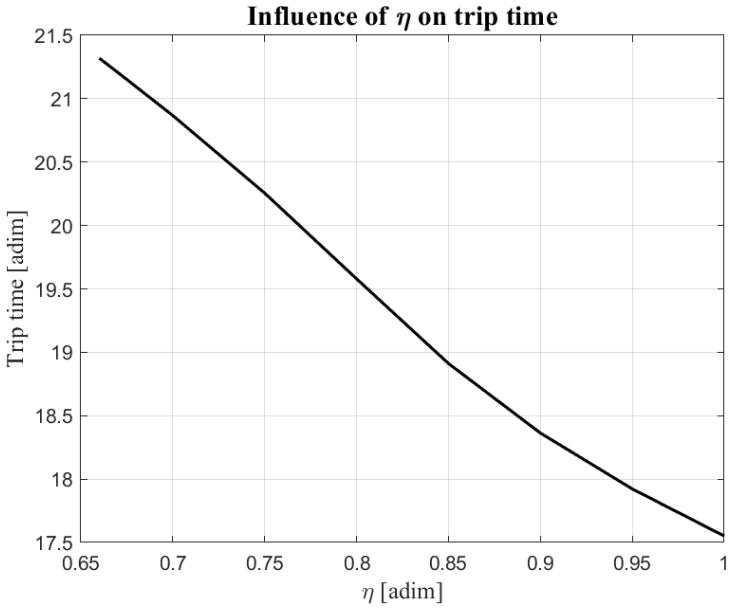

Figure 7.2: Effect of η on trip time

Table 7.3: Numerical results for varying η with fixed departure time $T_0 = 227$ and characteristic acceleration $a = 0.05$

Departure time [adim]	**acc** $[mm/s^2]$	η	**Trip time [adim]**	**Trip time [days]**	θ_0 $[rad]$	$\Delta\theta$ $[rad]$
227	0.05	1.00	17.5511532808677	1020.29138024850	2.5725	13.9531
227	0.05	0.95	17.9221872521943	1041.86049064631	2.5725	14.3728
227	0.05	0.90	18.3632406072880	1067.49999873051	2.5725	14.8758
227	0.05	0.85	18.9113339411759	1099.36200205237	2.5725	15.4841
227	0.05	0.80	19.5791779306165	1138.18540327694	2.5725	16.1252
227	0.05	0.75	20.2554504585470	1177.49877601686	2.5725	16.7506
227	0.05	0.70	20.8672551622712	1213.06447677829	2.5725	17.1224
227	0.05	0.67	21.2081008520473	1232.87866868399	2.5725	17.2471
227	0.05	0.66	21.3191019826440	1239.33143534458	4.6807	134.0930

A similar same trend is obtained observed when repeating the analysis for a departure time of 169; the results are presented in section C.1.

7.3 Effect of the variation of the characteristic acceleration on the solution

Table 7.4: Numerical results for varying characteristic acceleration with fixed departure time $t_0 = 227$ and $\eta = 1$

Departure time [adim]	**acc** $[mm/s^2]$	η	**Trip time [adim]**	**Trip time [days]**	θ_0 $[rad]$	$\Delta\theta$ $[rad]$
227	0.070	1.00	15.2335506989224	885.563485200255	2.5725	10.9483
227	0.065	1.00	15.7325384740450	914.570862530950	2.5725	11.5251
227	0.060	1.00	16.2452113301237	944.373787021084	2.5725	12.1319
227	0.055	1.00	16.8244952207826	978.048973540042	2.5725	12.8025
227	0.050	1.00	17.5511532808677	1020.29138024850	2.5725	13.5831
227	0.045	1.00	18.5547523318785	1078.63304273561	2.5725	14.5502
227	0.040	1.00	20.0469031267203	1165.37541058147	2.5725	15.9229
227	0.035	1.00	21.4671057360376	1247.93525478683	2.5725	17.4157
227	0.030	1.00	22.8636829626912	1329.12169783154	2.5725	19.0489

The same process is repeated for the characteristic acceleration. This parameter is defined in chapter 5 by Equation 5.20 as a function of the sail area-to-mass ratio. In this case, the non-dimensional departure time and η values are kept constant, while the characteristic acceleration is varied. Numerical results are displayed in Table 7.4. The results displayed in the table are summed in a graph for a better visualization, Figure 7.3.

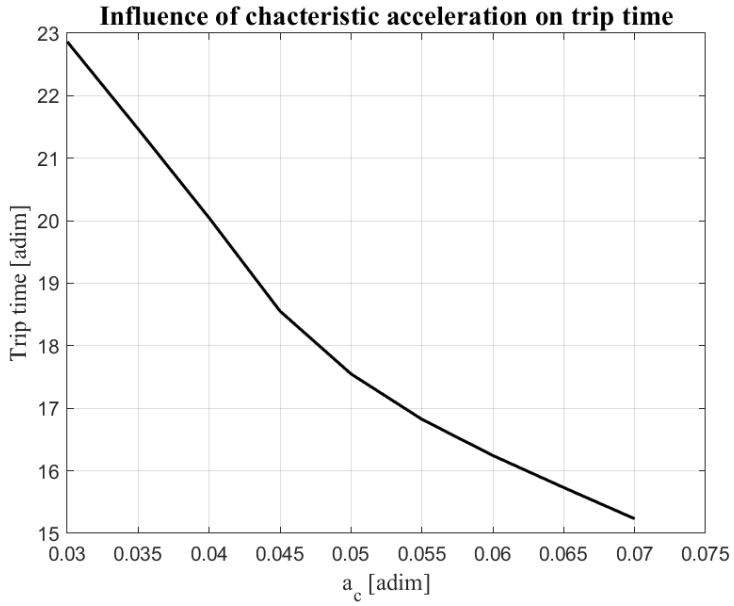

Figure 7.3: Effect of a_c on trip time

From the numerical results, it can be observed that the trip time decreases as the characteristic acceleration increases. This behaviour is consistent with the definition of characteristic acceleration, which depends on the area-to-mass ratio. A larger area enables the capture of more light, providing a greater thrust magnitude. Conversely, a larger mass requires a proportionally greater thrust to achieve the same characteristic acceleration.
The analysis is repeated for a departure time of 169. The numerical results are presented in section C.2. This second analysis reveals the same trend in the results as observed for departure time 227.

7.3.1 Trajectory Plots

In this section, the graphs for the trajectory are presented, along with the orbital parameters and the angles of the missions of minimum trip time for each year, emphasized in Table 7.2.

Mission departure time 201

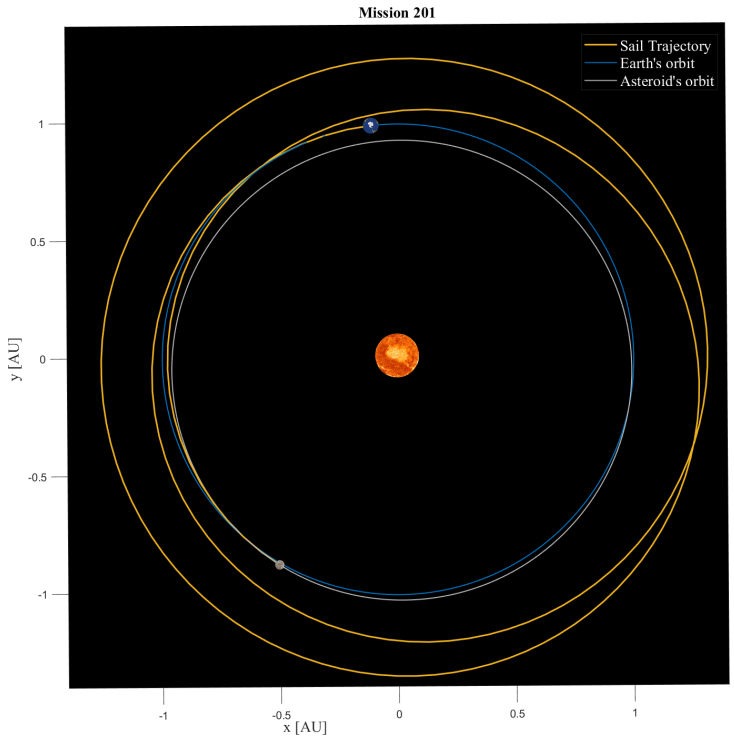

Figure 7.4: Mission trajectory for departure time 201

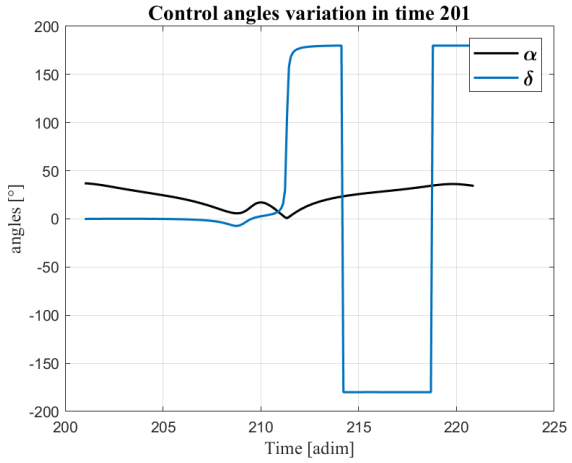

Figure 7.5: Control angles for departure time 201

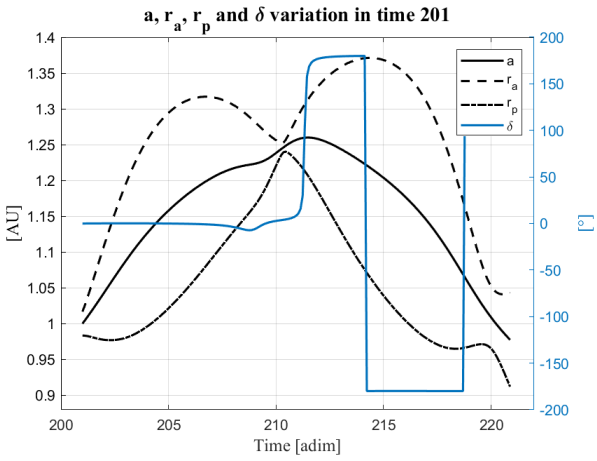

Figure 7.6: Semi-major axis, periapsis, apoapsis and δ variation in time for departure time 201

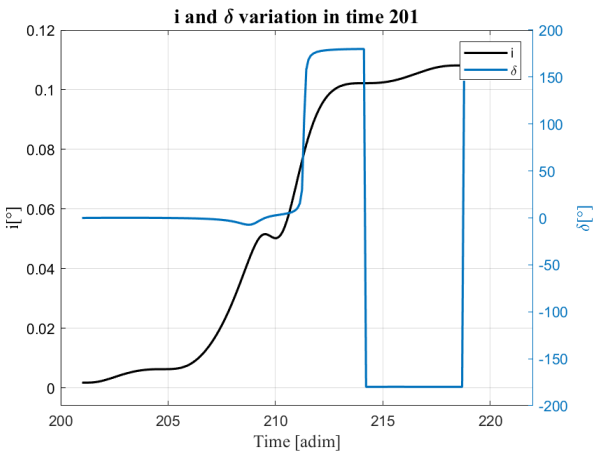

Figure 7.7: Inclination variation in time for departure time 201

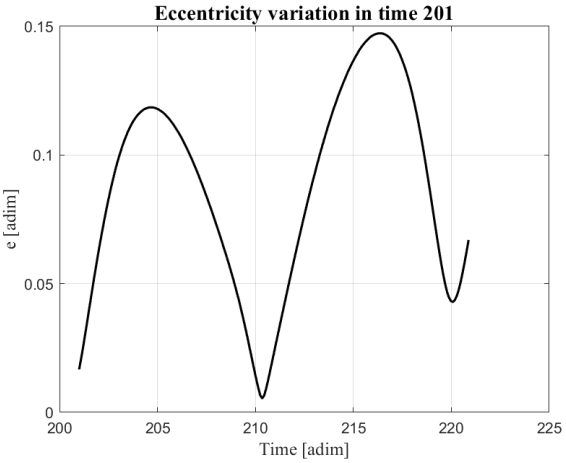

Figure 7.8: Eccentricity variation in time for departure time 201

Mission departure time 208

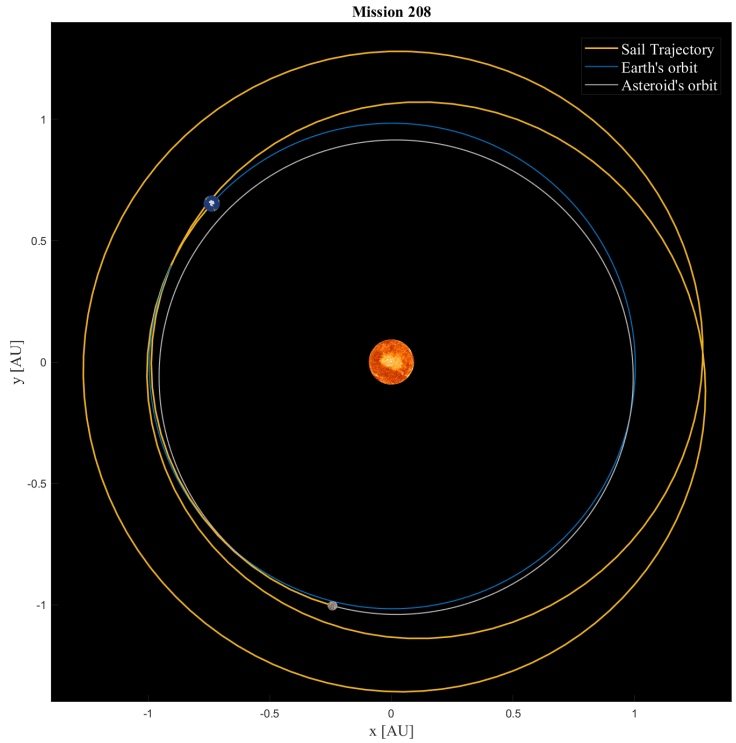

Figure 7.9: Mission trajectory for departure time 208

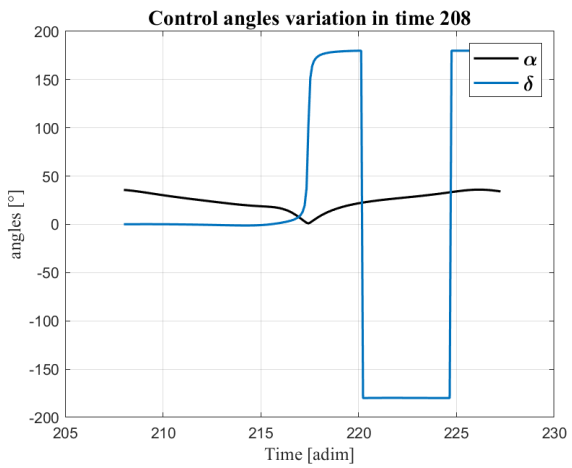

Figure 7.10: Control angles for departure time 208

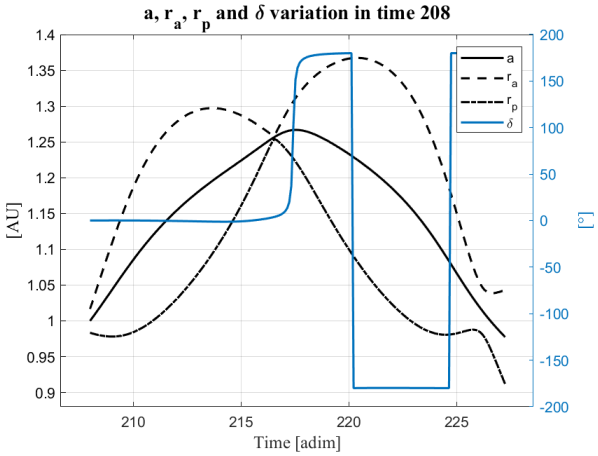

Figure 7.11: Semi-major axis, periapsis, apoapsis and δ variation in time for departure time 208

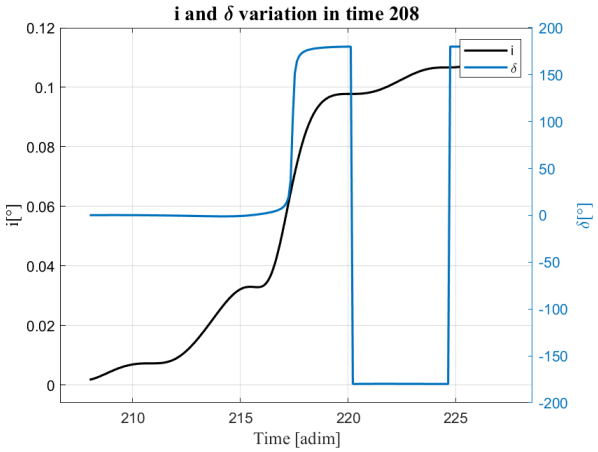

Figure 7.12: Inclination variation in time for departure time 208

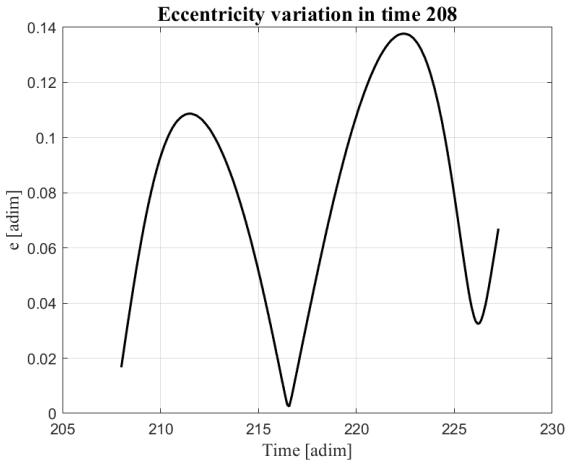

Figure 7.13: Eccentricity variation in time for departure time 208

Mission departure time 214

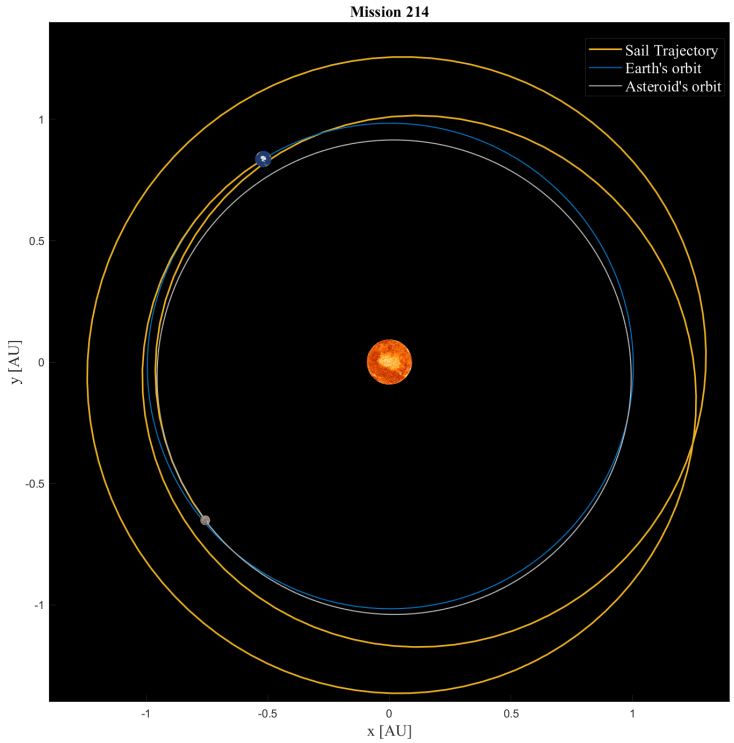

Figure 7.14: Mission trajectory for departure time 214

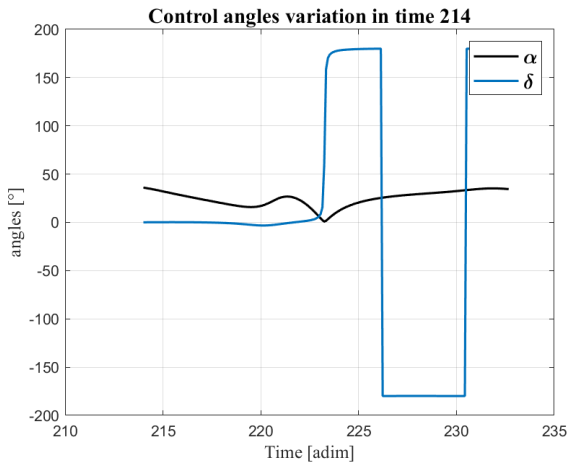

Figure 7.15: Control angles for departure time 214

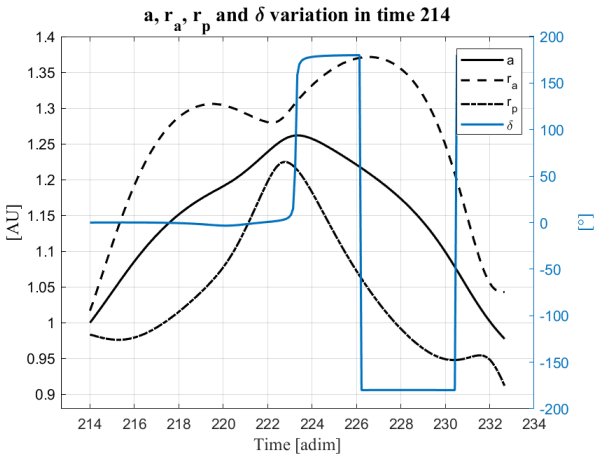

Figure 7.16: Semi-major axis, periapsis, apoapsis and δ variation in time for departure time 214

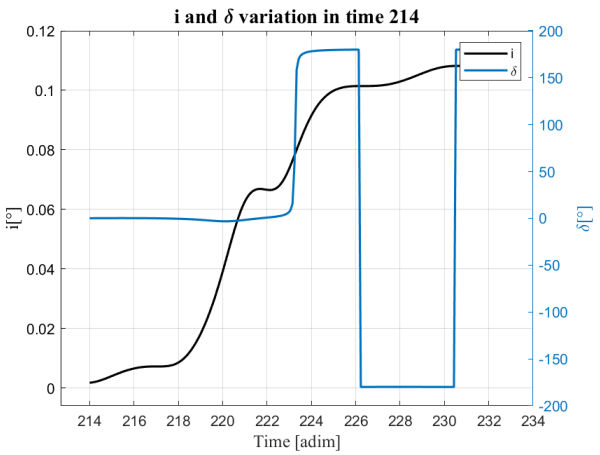

Figure 7.17: Inclination variation in time for departure time 214

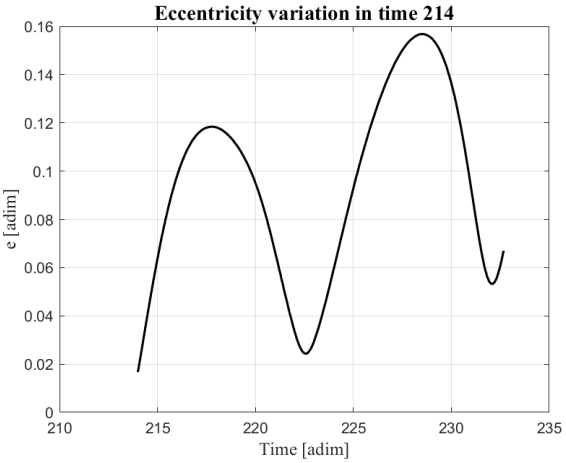

Figure 7.18: Eccentricity variation in time for departure time 214

Mission departure time 221

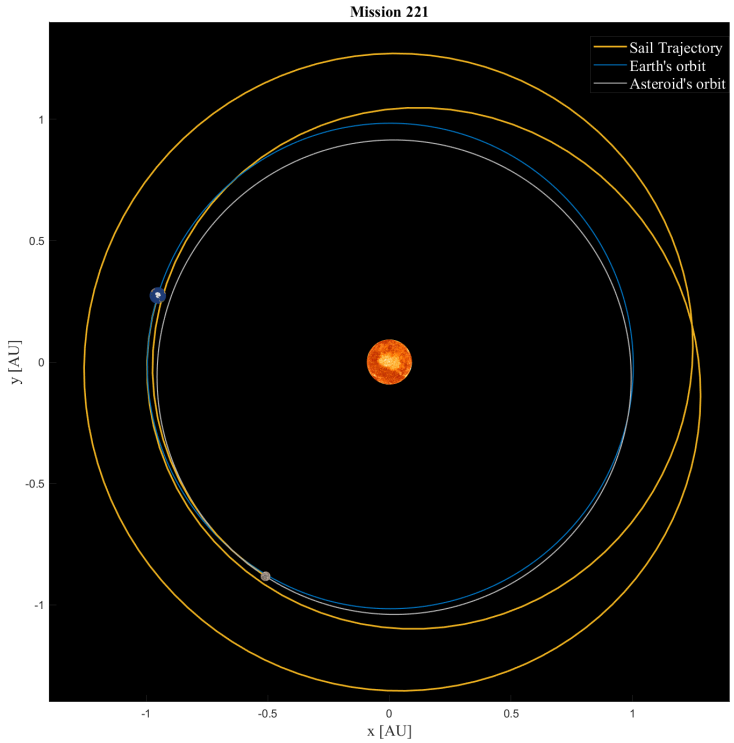

Figure 7.19: Mission trajectory for departure time 221

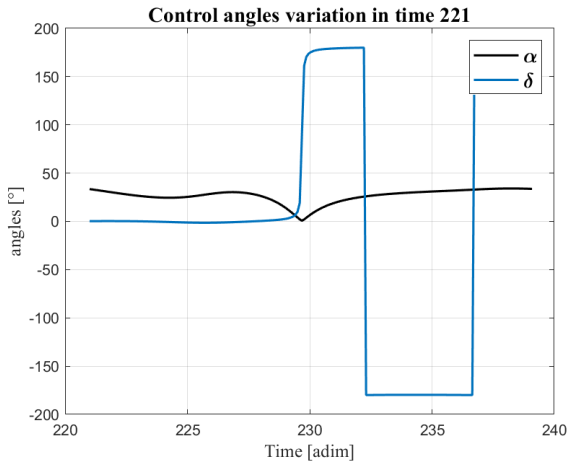

Figure 7.20: Control angles for departure time 221

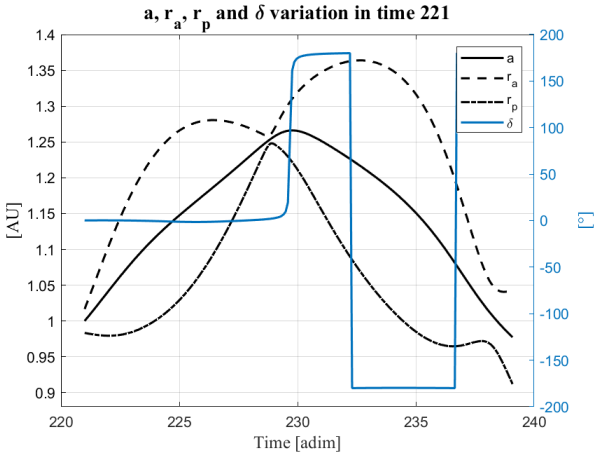

Figure 7.21: Semi-major axis, periapsis, apoapsis and δ variation in time for departure time 221

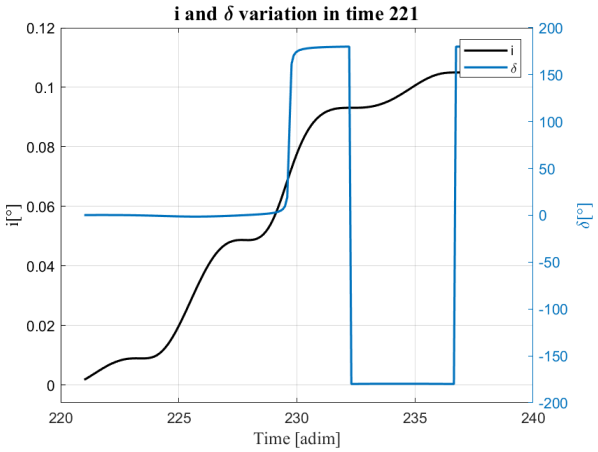

Figure 7.22: Inclination variation in time for departure time 221

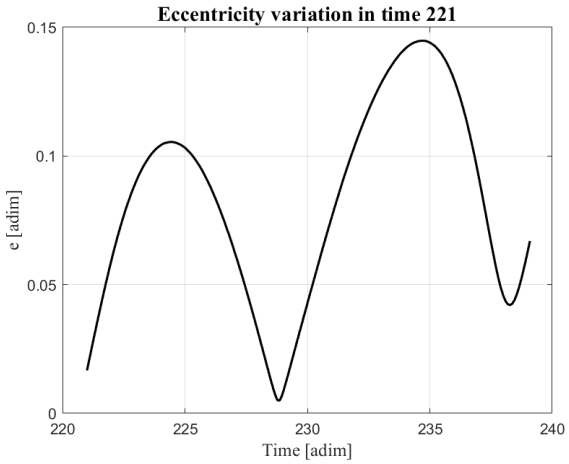

Figure 7.23: Eccentricity variation in time for departure time 221

Mission departure time 227

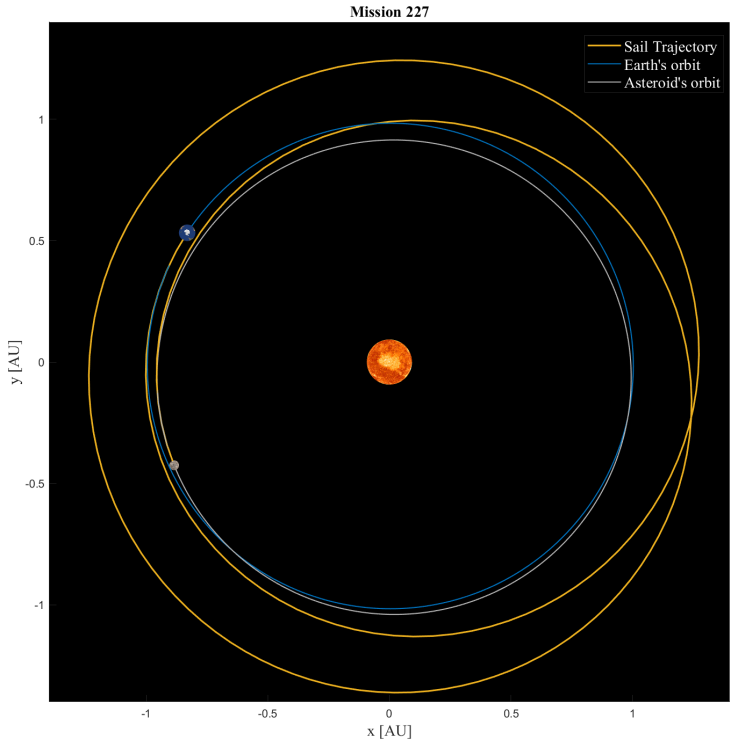

Figure 7.24: Mission trajectory for departure time 227

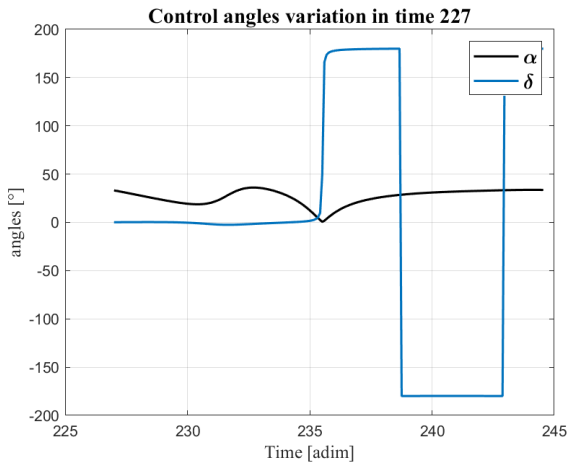

Figure 7.25: Control angles for departure time 227

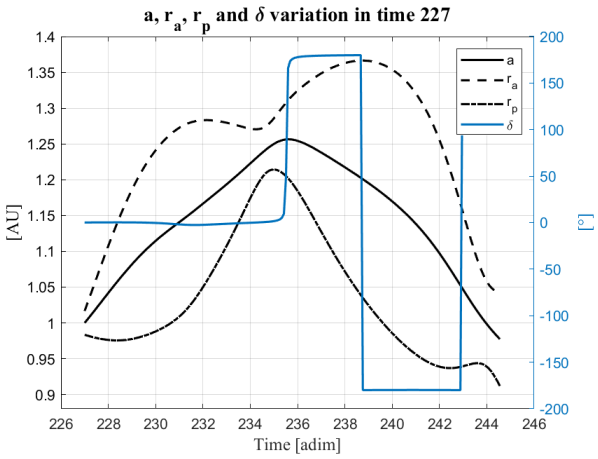

Figure 7.26: Semi-major axis, periapsis, apoapsis and δ variation in time for departure time 227

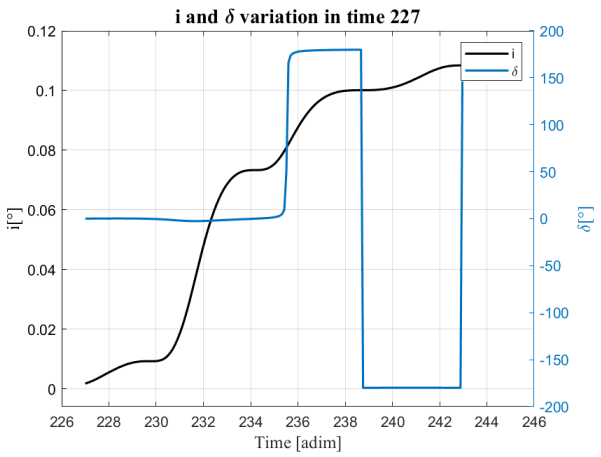

Figure 7.27: Inclination variation in time for departure time 227

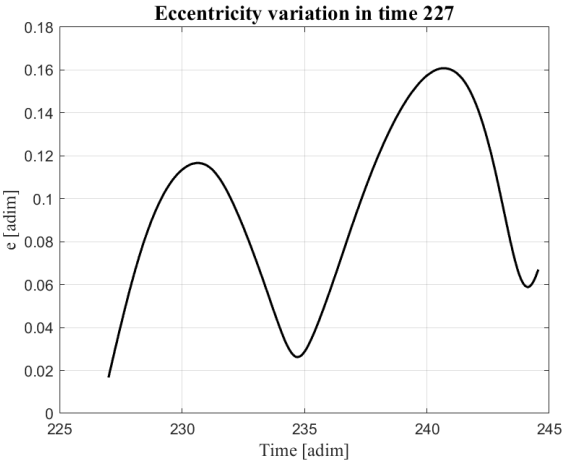

Figure 7.28: Eccentricity variation in time for departure time 227

Comment on the plots

The spacecraft departs from Earth and is directed toward the designated asteroid. To rendezvous with the asteroid, the spacecraft needs to lower the periapsis r_p and increase the apoapsis r_a. The Earth's perihelion is $r_{p_\oplus} = 0,98329134\,\text{AU}$ and the asteroid perihelion is $r_{p_a} = 0.91199\,\text{AU}$, while Earth's aphelion is $r_{a_\oplus} = 1,01671388\,\text{AU}$ and the asteroid's aphelion is $r_{a_a} = 1.0429\,\text{AU}$. The increase of the apoapsis is achieved by accelerating the sail. The cone angle α shows a decreasing trend, approaching zero, which corresponds to the inclination that provides the maximum thrust. This allows an increase of the semi-major axis. An increased semi-major axis allows the spacecraft to slow down the spacecraft and achieve the correct phase angle for the rendezvous with the asteroid, as previously explained. In this phase the clock angle δ is equal to zero. When the spacecraft reaches the appropriate position to complete the rendezvous, the sail begins to decelerate, and the cone angle starts to increase again. This manoeuvre allows decreasing the periapsis to the desired value. The semi-major axis decreases until it reaches the same value of the semi-major axis of the asteroid. The clock angle δ, which remains at zero during the first phase, in the second phase becomes equal to $\pm 180°$ indicating that the spacecraft is decelerating. Depending on whether the spacecraft is near the ascending or descending node, the sign of δ changes to either $+180°$ or $-180°$, indicating a change in the component of the thrust outside the ecliptic plane which is directed northward in the first case and southward in the second. The behaviour of the periapsis and apoapsis shows a general increase during the first part of the mission and a general decrease during the second part, in line with the trend of the semi-major axis. However, neither the periapsis nor the apoapsis increases or decreases consistently. This is due to changes in the shape of the orbit. This variation can be observed in the eccentricity graph, which follows the same trend as the apoapsis and the opposite trend of the periapsis. Regarding the inclination, an increasing trend can be observed. This is justified by the difference between the inclination of the Earth's and asteroid's orbits. Earth's inclination is $i_\oplus = 0.001748°$ and asteroid's is $i_a = 0.11220°$. The plane change manoeuvre is performed around $\delta = \pm 90°$, which corresponds to the spacecraft passing through the apoapsis, the point along the trajectory where the cost of the plane change is minimized.

7.4 2014 QN266

In this section numerical results for asteroid 2014 QN266 are presented. The same procedure as the one adopted for asteroid 2000 SG344 is used. Different departure times are considered beginning on 10 December 2025 and delaying the departure by one year each time. Numerical results are presented in Table 7.5:

Table 7.5: Numerical results for departure times spaced one year apart, with fixed a_c and η

Departure time [adim]	**acc** $[mm/s^2]$	η	**Trip time [adim]**	**Trip time [days]**	θ_0 $[rad]$	$\Delta\theta$ $[rad]$
163	0.05	1	24.4623180803485	1422.05425927673	1.3679	17.3815
169	0.05	1	25.6988795875237	1493.93859797106	1.0766	18.0451
175	0.05	1	26.8506021934836	1560.89104425726	0.7871	18.6248
181	0.05	1	27.9398696773959	1624.21282185419	0.4999	19.1480
187	0.05	1	28.9846378079953	1684.94774342604	0.2153	19.6330
193	0.05	1	29.9975420919856	1743.83034181908	6.2166	20.0908
199	0.05	1	30.9873162540921	1801.36832976947	5.9371	20.5300
205	0.05	1	31.9599606976745	1857.91052537068	5.6599	20.9552
211	0.05	1	32.9194169744208	1913.68606064315	5.3844	21.3703
217	0.05	1	33.8680674794849	1968.83343003229	5.1099	21.7781
223	0.05	1	34.8071689060739	2023.42568818163	4.8359	22.1800
229	0.05	1	35.7372966064537	2077.49628172276	4.5617	22.5770

It is observed in Figure 7.29, that in this case the mission duration tends to increase over time. For this reason it was decided to analyse in detail the time period from 10 December 2025 to 19 September 2030. Numerical results are presented in Table 7.6.

The minimum mission duration is achieved by departing on 5 May 2026 (165) and it corresponds to a trip time of 1418.20992005544 days or approximately 3.88 years. The same condition will occur again after a synodic period, which is equal to $\tau = 84.8576$ for asteroid 2014 QN266.

In the following section, the trajectories and the graphs of the parameters of the missions with the shortest duration, highlighted in bold in the table, are presented.

Table 7.6: Numerical results for mission departing between 163 and 193

Departure time [adim]	**acc** $[mm/s^2]$	η	**Trip time [adim]**	**Trip time [days]**	θ_0 $[rad]$	$\Delta\theta$ $[rad]$
163	0.05	1	24.4623180803485	1422.05425927673	1.3679	17.3815
164	0.05	1	24.3982384368953	1418.32915319291	2.4004	17.1043
165	**0.05**	**1**	**24.3961873766665**	**1418.20992005544**	**3.4149**	**16.8660**
166	0.05	1	25.1174159555607	1460.13669776963	4.3989	17.4125
167	0.05	1	25.4067072490599	1476.95390678233	5.3675	17.8491
168	0.05	1	25.5890061038738	1487.55138417992	0.0653	18.0946
169	0.05	1	25.6988795875237	1493.93859797106	1.0766	18.0451
170	0.05	1	25.6378729173158	1490.39213132270	2.1085	17.7477
171	**0.05**	**1**	**25.5838360985879**	**1487.25083915336**	**3.1307**	**17.4750**
172	0.05	1	26.1454510622247	1519.89888781702	4.1228	17.9400
173	0.05	1	26.4289955339514	1536.38202005285	5.0931	18.3840
174	0.05	1	26.6820740105804	1551.09408963021	6.0679	18.6580
175	0.05	1	26.8506021934836	1560.89104425726	0.7871	18.6248
176	0.05	1	26.7814811443091	1556.87286895346	1.8158	18.3185
177	**0.05**	**1**	**26.6635977737157**	**1550.02002088323**	**2.8439**	**18.0092**
178	0.05	1	27.1202602869577	1576.56692743047	3.8449	18.4201
179	0.05	1	27.4121045462979	1593.53254657895	4.8190	18.8709
180	0.05	1	27.7278359481524	1611.84678362713	5.7897	19.1646
181	0.05	1	27.9398696773959	1624.21282185419	0.4999	19.1480
182	0.05	1	27.8590830216970	1619.51649636893	1.5230	18.8423
183	**0.05**	**1**	**27.6780932035850**	**1608.99511646999**	**2.5546**	**18.4984**
184	0.05	1	28.0622499591095	1631.32708634420	3.5647	18.8707
185	0.05	1	28.3700677194850	1649.22128409706	4.5447	19.3266
186	0.05	1	28.7408437731461	1670.77540111142	5.5134	19.6335
187	0.05	1	28.9846378079953	1684.94774342604	0.2153	19.6330
188	0.05	1	28.8935076985389	1679.65012772685	1.2310	19.3357
189	**0.05**	**1**	**28.6566532483403**	**1665.88120040659**	**2.2635**	**18.9638**
190	0.05	1	28.9872559863323	1685.09994452339	3.2819	19.3073
191	0.05	1	29.3141713605359	1704.10433318281	4.2695	19.7645
192	0.05	1	29.7316513046833	1728.37346134914	5.2385	20.0774
193	0.05	1	29.9975420919856	1743.83034181908	6.2166	20.0908

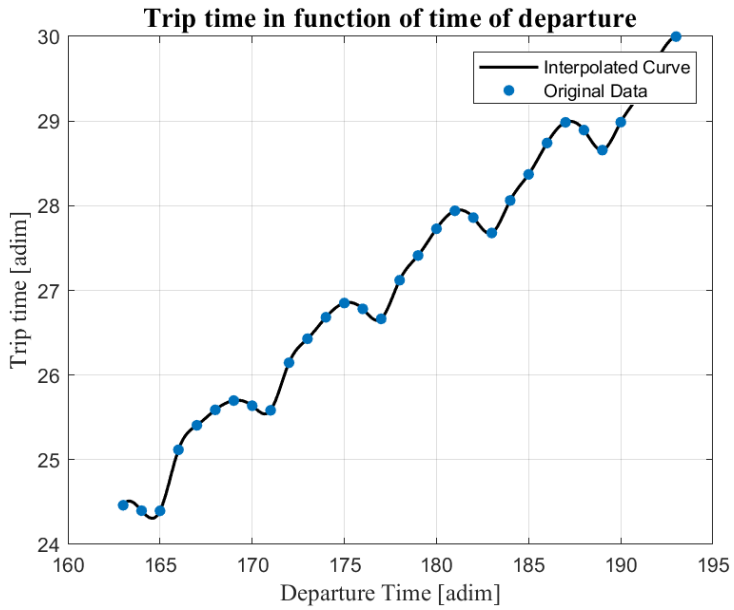

Figure 7.29: Numerical results for mission from 163 to 193

Mission departure time 165

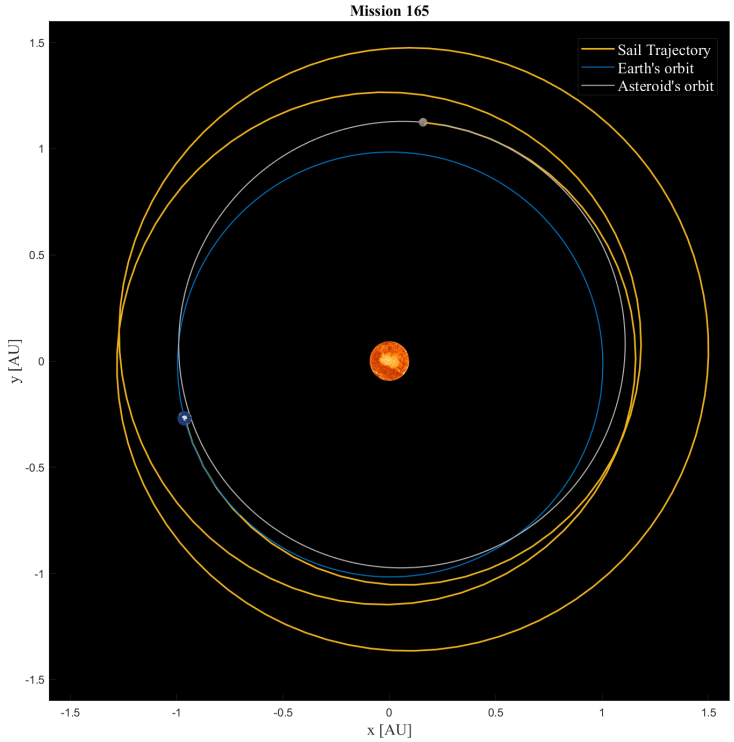

Figure 7.30: Mission trajectory for departure time 165

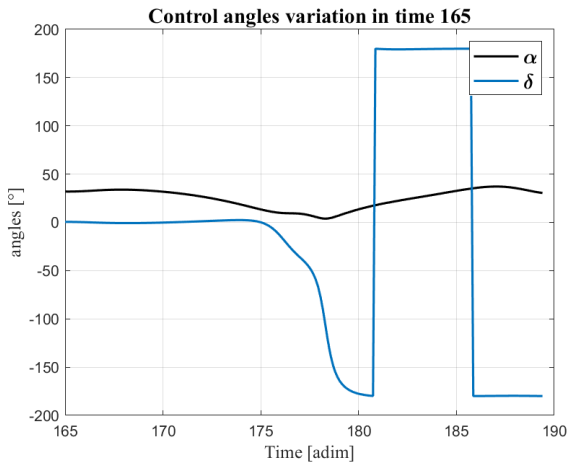

Figure 7.31: Control angles for departure time 165

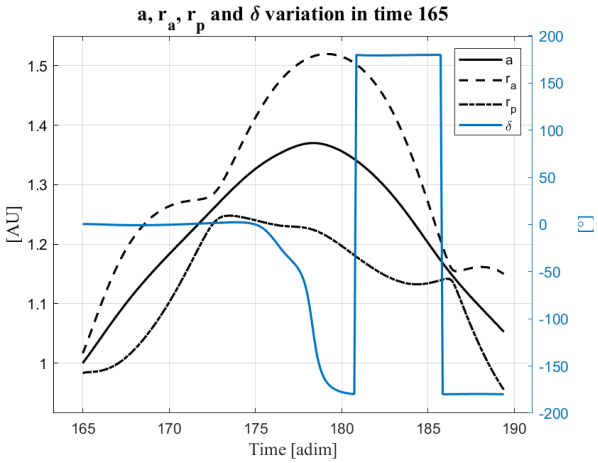

Figure 7.32: Semi-major axis, periapsis, apoapsis and δ variation in time for departure time 165

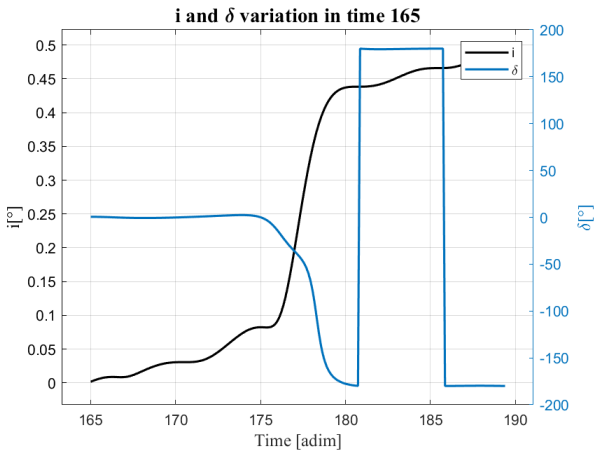

Figure 7.33: Inclination variation in time for departure time 165

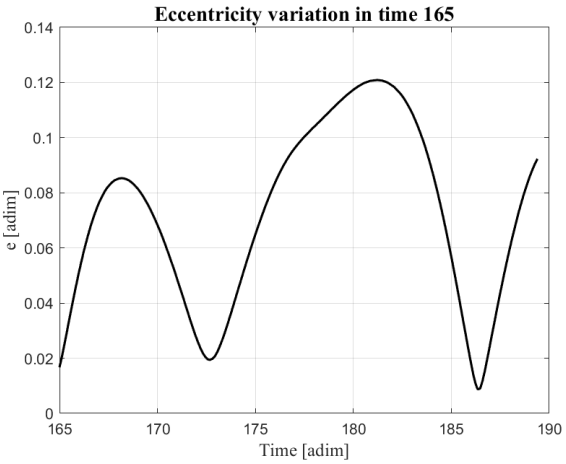

Figure 7.34: Eccentricity variation in time for departure time 165

Mission departure time 171

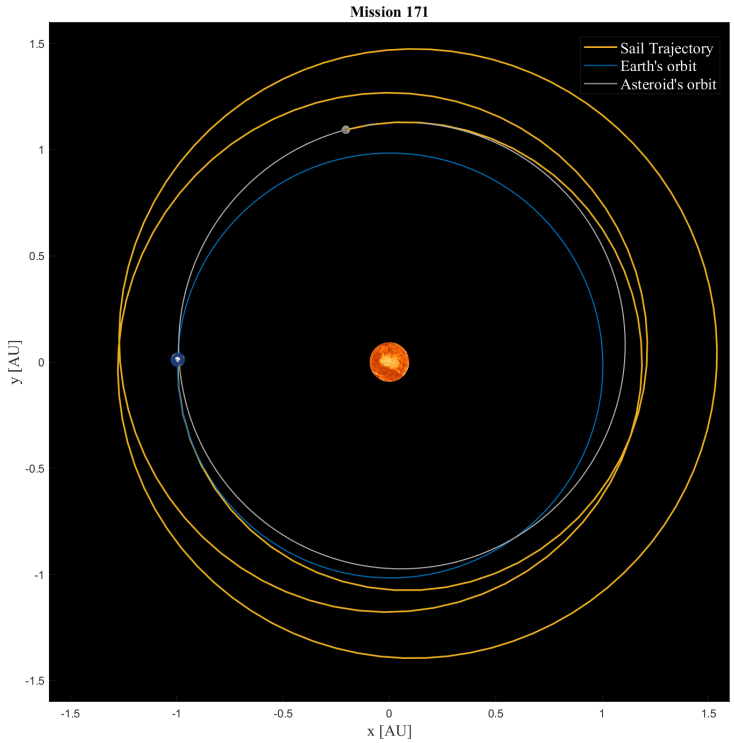

Figure 7.35: Mission trajectory for departure time 171

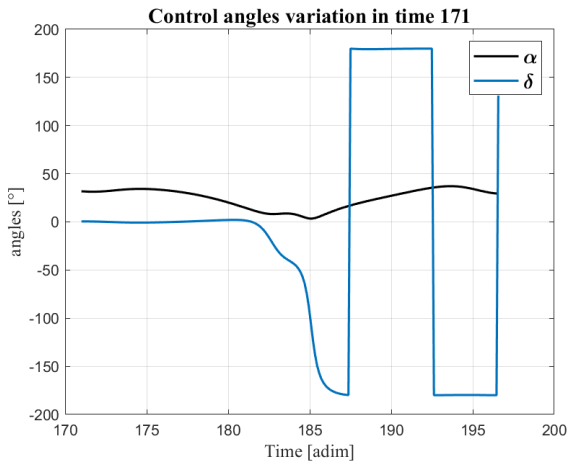

Figure 7.36: Control angles for departure time 171

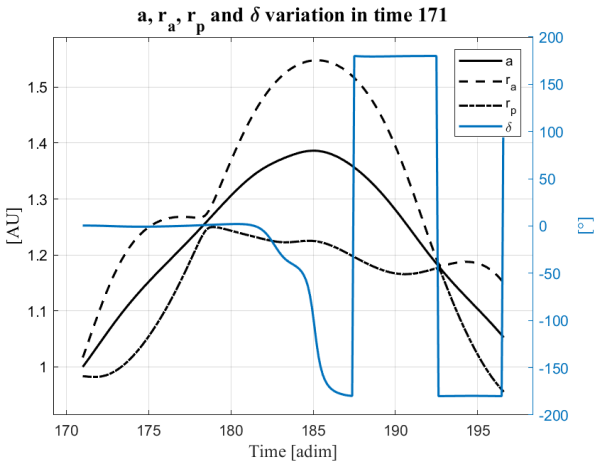

Figure 7.37: Semi-major axis, periapsis, apoapsis and δ variation in time for departure time 171

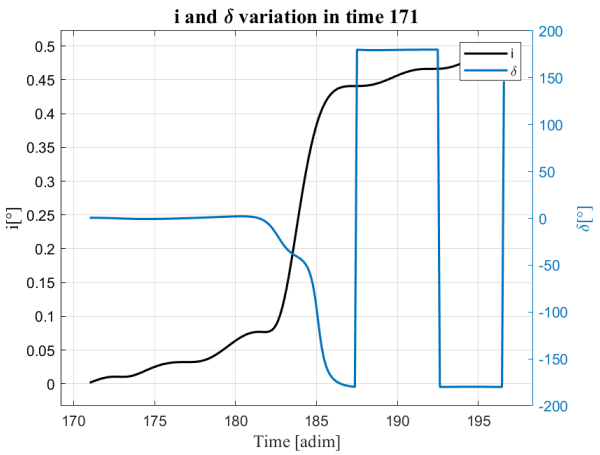

Figure 7.38: Inclination variation in time for departure time 171

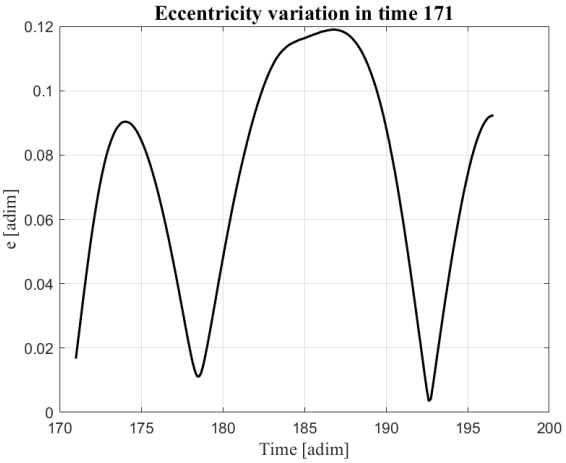

Figure 7.39: Eccentricity variation in time for departure time 171

Mission departure time 177

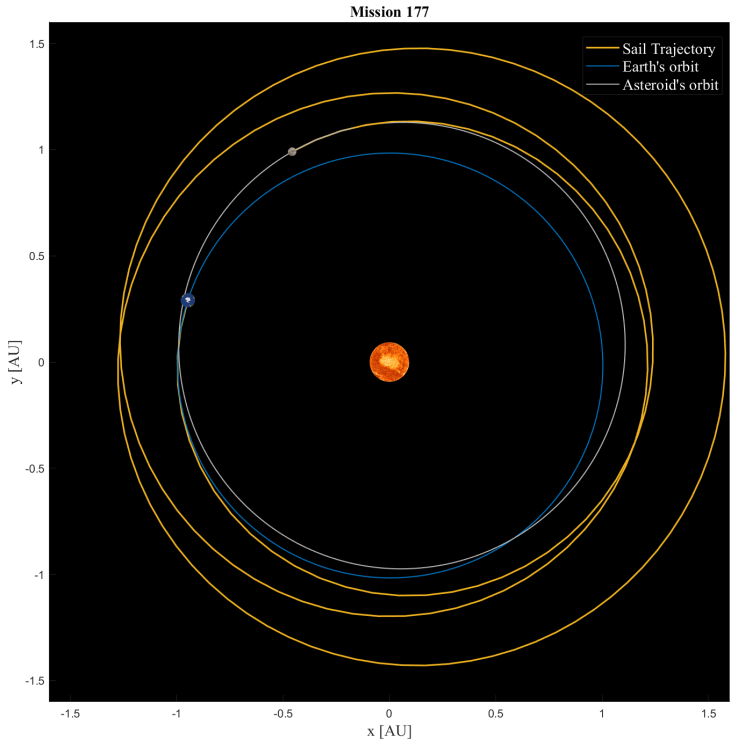

Figure 7.40: Mission trajectory for departure time 177

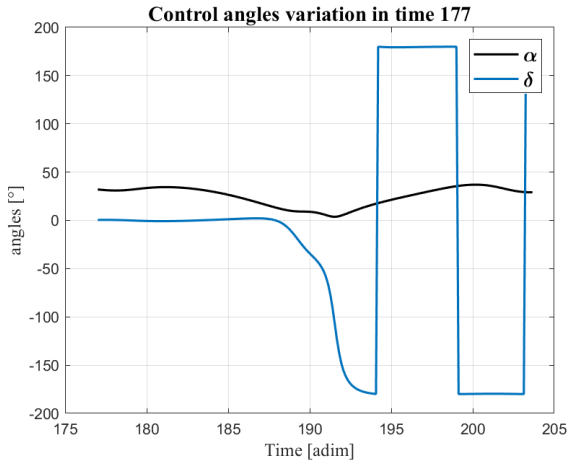

Figure 7.41: Control angles for departure time 177

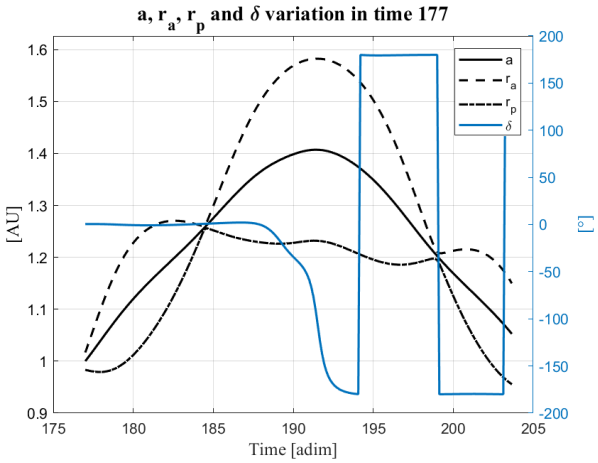

Figure 7.42: Semi-major axis, periapsis, apoapsis and δ variation in time for departure time 177

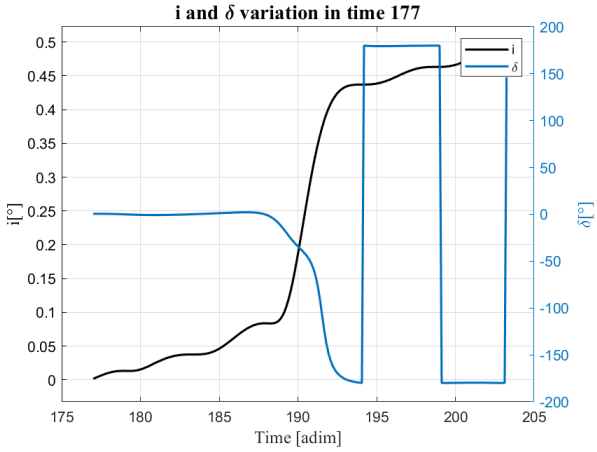

Figure 7.43: Inclination variation in time for departure time 177

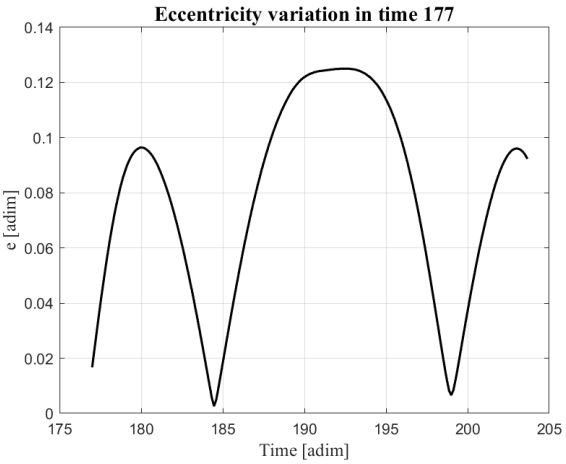

Figure 7.44: Eccentricity variation in time for departure time 177

Mission departure time 183

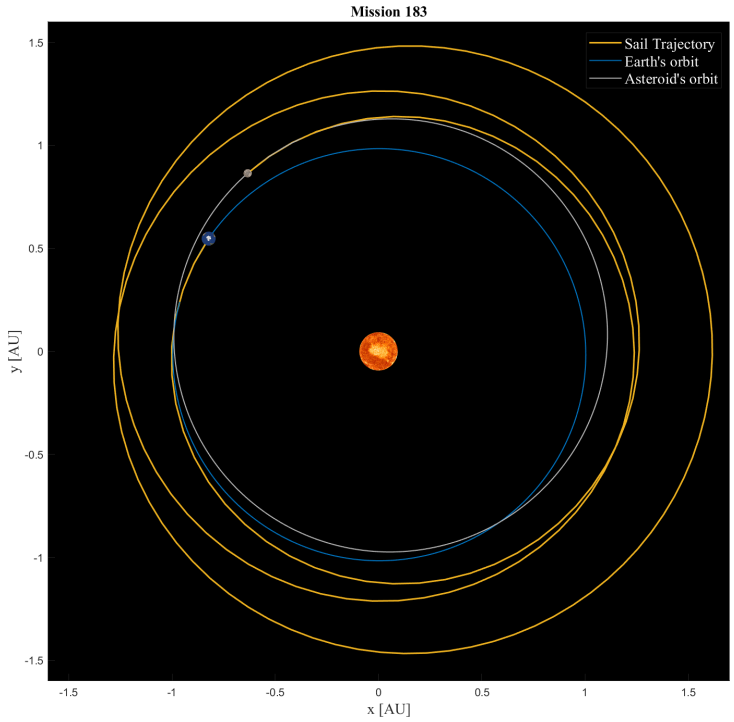

Figure 7.45: Mission trajectory for departure time 183

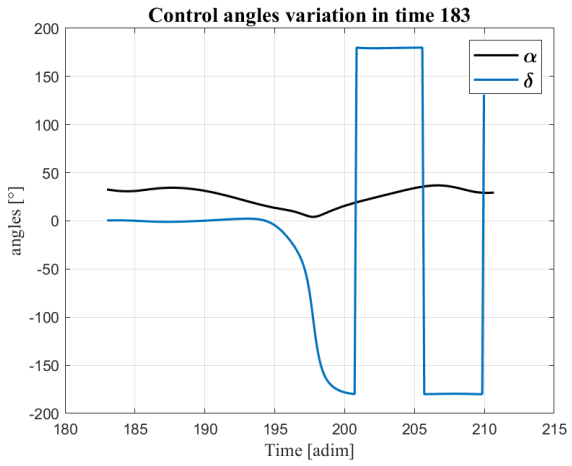

Figure 7.46: Control angles for departure time 183

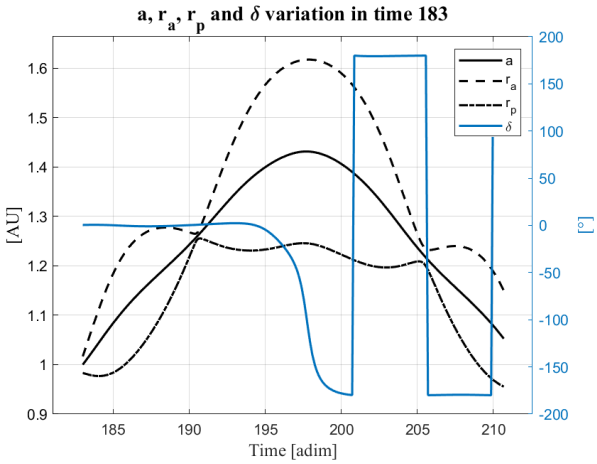

Figure 7.47: Semi-major axis, periapsis, apoapsis and δ variation in time for departure time 183

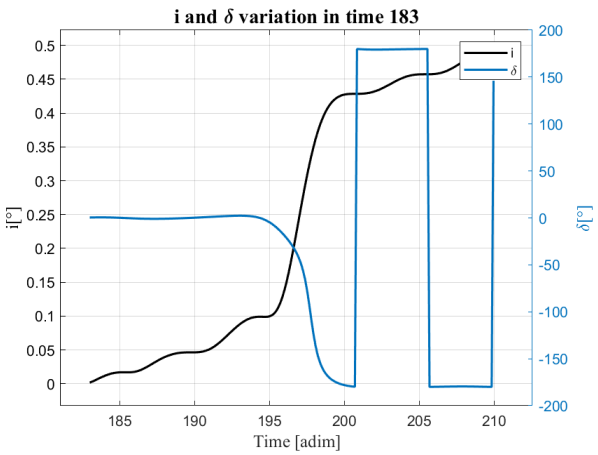

Figure 7.48: Inclination variation in time for departure time 183

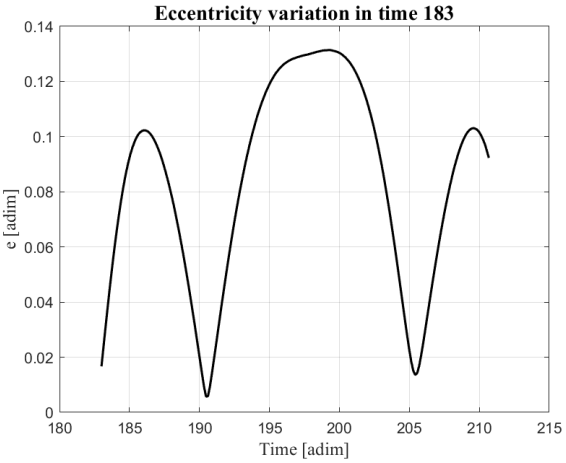

Figure 7.49: Eccentricity variation in time for departure time 183

Mission departure time 189

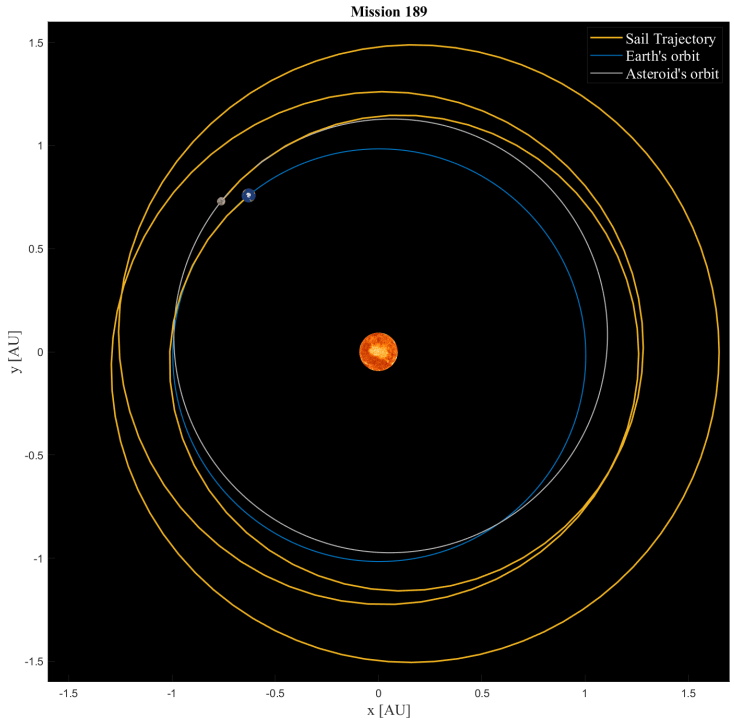

Figure 7.50: Mission trajectory for departure time 189

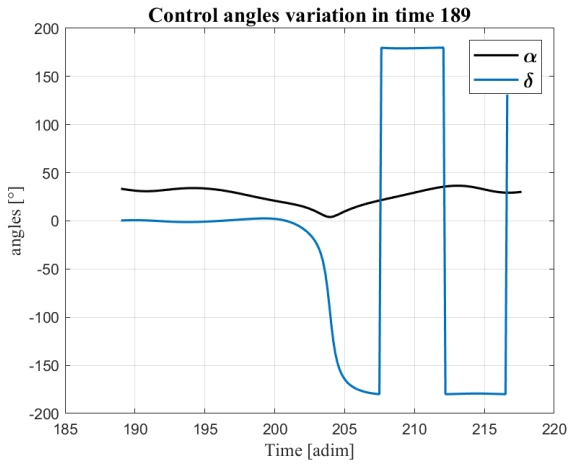

Figure 7.51: Control angles for departure time 189

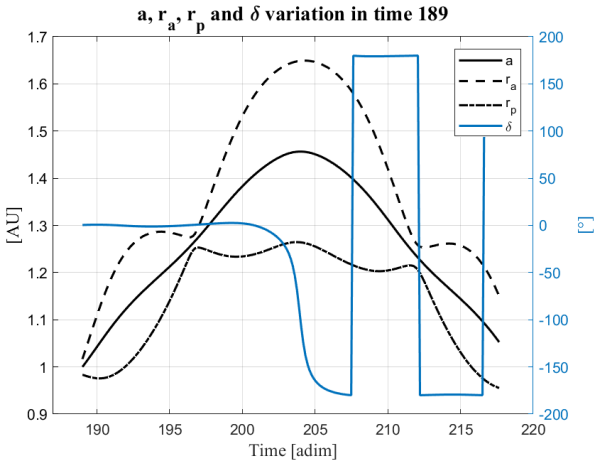

Figure 7.52: Semi-major axis, periapsis, apoapsis and δ variation in time for departure time 189

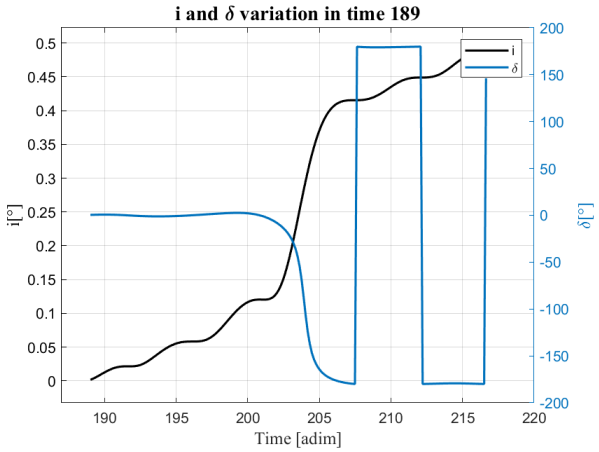

Figure 7.53: Inclination variation in time for departure time 189

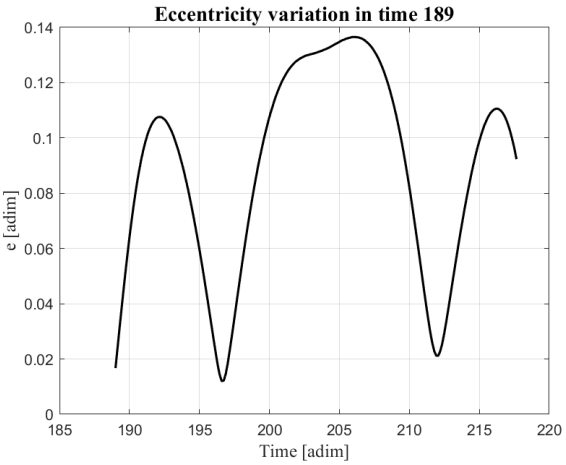

Figure 7.54: Eccentricity variation in time for departure time 189

Comment on the plots

The behaviour of the different parameters, as shown in the graphs for asteroid 2014 QN266, is consistent with what was observed for asteroid 2000 SG344. The objective of the first part is to increase the aphelion from $r_{a_\oplus} = 1,01671388\,\text{AU}$ to $r_{a_{asteroid}} = 1.149800632\,\text{AU}$. During the second part of the mission the objective is to lower the periapsis from $r_{p_\oplus} = 0,98329134\,\text{AU}$, which is the perihelion of Earth's orbit, to $r_{p_{asteroid}} = 0.955456167\,\text{AU}$. The inclination varies from $i_\oplus = 0.001748°$ to $i_{asteroid} = 0.48842°$.

7.5 2020 PJ6

In this section, numerical results are presented for asteroid 2020 PJ6. The procedure used to obtain these results is the same as that described for the previous asteroids. Numerical results are displayed in Table 7.7:

Table 7.7: Numerical results for departure times spaced one year apart, with fixed a_c and η

Departure time [adim]	**acc** $[mm/s^2]$	η	**Trip time [adim]**	**Trip time [days]**	θ_0 $[rad]$	$\Delta\theta$ $[rad]$
169	0.05	1	28.5697708938022	1660.83051706901	1.0766	20.0198
175	0.05	1	27.9949938584577	1627.41732505011	0.7871	19.6290
181	0.05	1	27.4628720336366	1596.48378453463	0.4999	19.2943
187	0.05	1	26.9775322577617	1568.26979871316	0.2153	19.0509
193	0.05	1	26.5348436387290	1542.53522874473	6.2165	18.8940
199	0.05	1	26.0850269979724	1516.38628947493	5.9371	18.7620
205	0.05	1	25.5843280810195	1487.27943929297	5.6599	18.6096
211	0.05	1	25.0049660795741	1453.59971200334	5.3843	18.4086
217	0.05	1	24.3401799342609	1414.95407072168	5.1099	18.1387
223	0.05	1	23.6215686291337	1373.17944151999	4.8359	17.7922
229	0.05	1	22.9086850065380	1331.73777648436	4.5617	17.3796
235	0.05	1	22.2407058360014	1292.90651685272	4.2865	16.9247

It can be observed that the trip time tends to decrease over time. The solution is therefore examined in detail for the time period between 3 September 2031 (199) and 12 June 2036 (299). Numerical results are displayed in Table 7.8, where the solutions of minimum trip time are highlighted in bold. Numerical results are summarised in Figure 7.55:

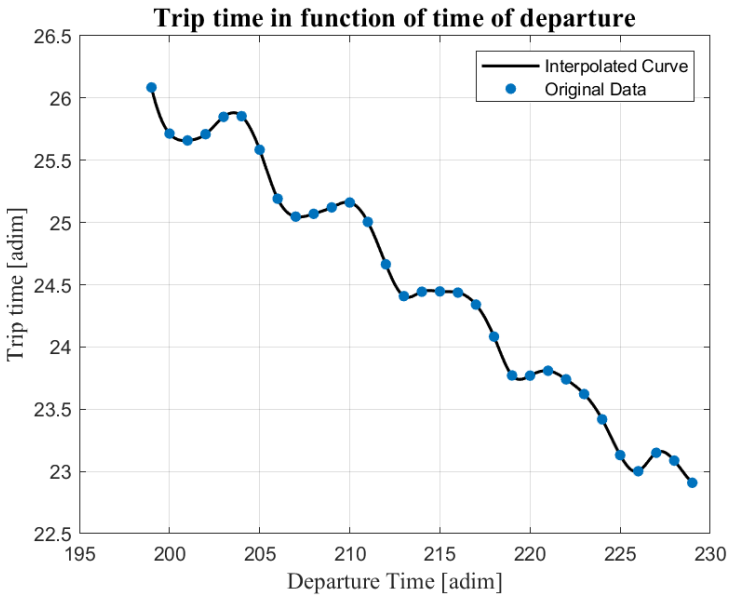

Figure 7.55: Numerical results for mission from 199 to 299

Table 7.8: Numerical results for mission departing between 199 and 299

Departure time [adim]	**acc** $[mm/s^2]$	η	**Trip time [adim]**	**Trip time [days]**	θ_0 $[rad]$	$\Delta\theta$ $[rad]$
199	0.05	1	26.0850269979724	1516.38628947493	1.0766	20.0198
200	0.05	1	25.7141807637178	1494.82809269136	0.7871	19.6290
201	**0.05**	**1**	**25.6589808413385**	**1491.61918646778**	**0.4999**	**19.2943**
202	0.05	1	25.7095616568535	1494.55957273471	0.2153	19.0509
203	0.05	1	25.8482804857845	1502.62363685469	6.2165	18.8940
204	0.05	1	25.8540199805019	1502.95728769196	5.9371	18.7620
205	0.05	1	25.5843280810195	1487.27943929297	0.6520	18.4134
206	0.05	1	25.1908621636740	1464.40630511969	1.6784	18.5225
207	**0.05**	**1**	**25.0469215248089**	**1456.03868444250**	**2.7084**	**18.8144**
208	0.05	1	25.0694364363355	1457.34753120544	3.7137	19.0100
209	0.05	1	25.1211848750530	1460.35579425915	4.6904	18.9342
210	0.05	1	25.1605314961705	1462.64310938458	5.6599	18.6096
211	0.05	1	25.0049660795741	1453.59971200334	0.3660	18.1956
212	0.05	1	24.6643356132201	1433.79803156049	1.3859	18.1084
213	**0.05**	**1**	**24.4083778060308**	**1418.91857946961**	**2.4183**	**18.3649**
214	0.05	1	24.4438018665559	1420.97786657335	3.4323	18.6024
215	0.05	1	24.4460766795611	1421.11010700586	4.4158	18.6347
216	0.05	1	24.4365912605770	1420.55869644767	5.3843	18.4086
217	0.05	1	24.3401799342609	1414.95407072168	0.0826	18.0154
218	0.05	1	24.0830717035317	1400.00774170239	1.0944	17.7329
219	0.05	1	23.7712355466659	1381.87994475318	2.1265	17.9077
220	**0.05**	**1**	**23.7694433575347**	**1381.77576042449**	**3.1483**	**18.1596**
221	0.05	1	23.8086066093479	1384.05241584468	4.1398	18.2657
222	0.05	1	23.7394972913306	1380.03492250168	5.1099	18.1387
223	0.05	1	23.6215686291337	1373.17944151999	6.0851	17.8131
224	0.05	1	23.4182920438956	1361.36247744898	0.8048	17.4321
225	0.05	1	23.1307696675633	1344.64809990889	1.8338	17.4355
226	**0.05**	**1**	**23.0015766513343**	**1337.13779453252**	**2.8616**	**17.6947**
227	0.05	1	23.1496948472660	1345.74826679885	3.8621	17.8425
228	0.05	1	23.0866792704510	1342.08501750595	4.8359	17.7922
229	0.05	1	22.9086850065380	1331.73777648436	5.8068	17.5478

The graph shows a sinusoidal trend, similar to that observed for the other asteroids, which is due to the variation of the phase angle between Earth and 2020 PJ6. In this case the duration of the mission is minimized by departing on 20 December 2035 and is equal to 1337.13779453252 days. The synodic period required before the same conditions are met again is equal to $\tau = 115.0473$. The decreasing trend of trip time suggests that a later departure could further reduce the mission duration. However, as was done for asteroid 2000 SG344, it was chosen to consider a departure date not too far in the future.

Graphs showing the trajectories and the variation of the parameters are presented in the following section for the missions with the minimum trip time.

Mission departure time 201

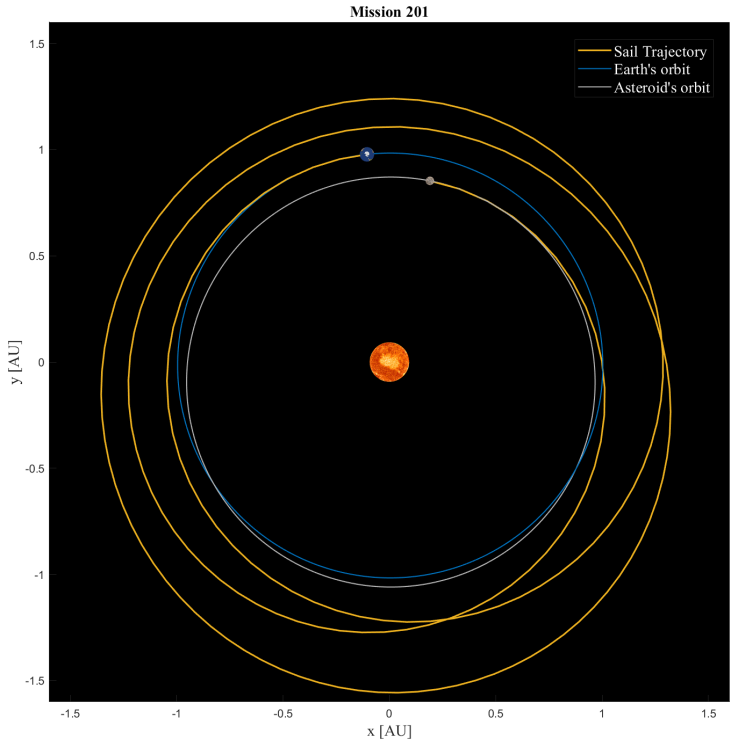

Figure 7.56: Mission trajectory for departure time 201

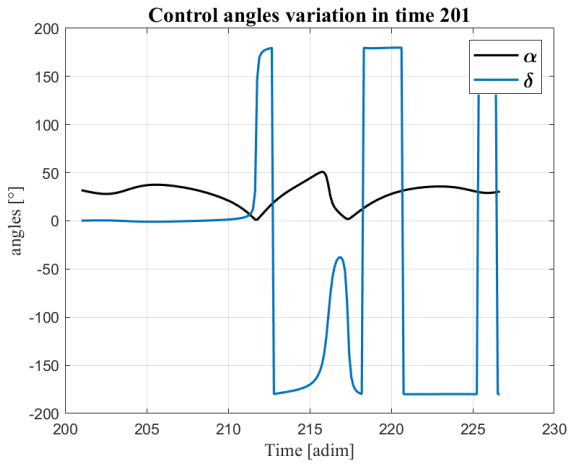

Figure 7.57: Control angles for departure time 201

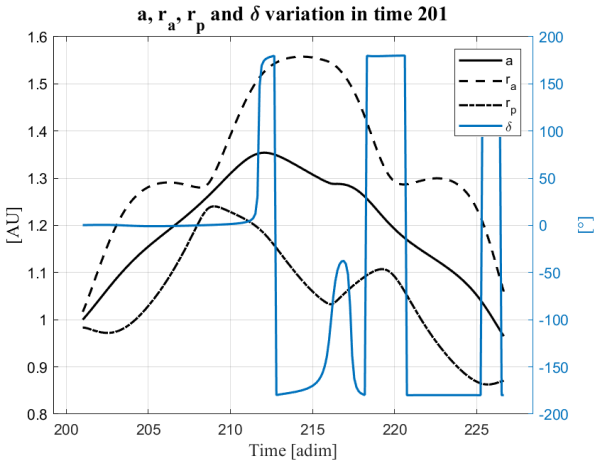

Figure 7.58: Semi-major axis, periapsis, apoapsis and δ variation in time for departure time 201

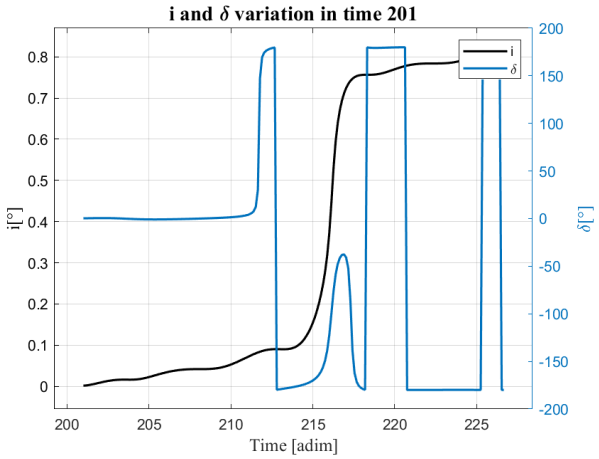

Figure 7.59: Inclination variation in time for departure time 201

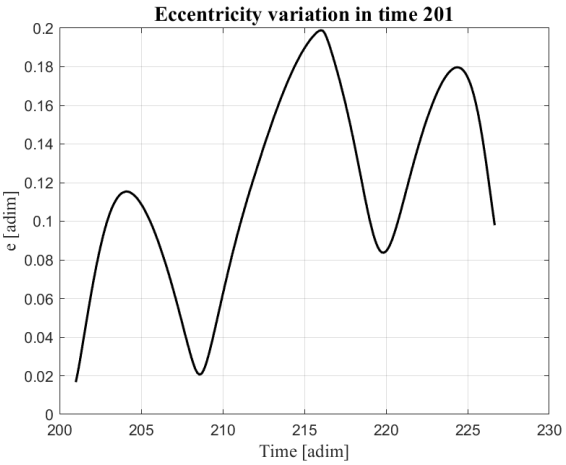

Figure 7.60: Eccentricity variation in time for departure time 201

Mission departure time 207

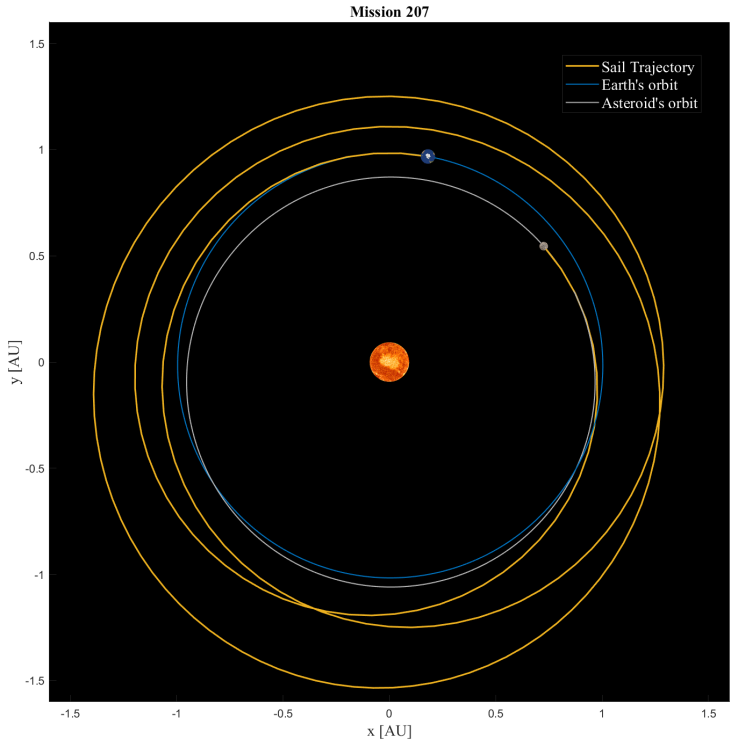

Figure 7.61: Mission trajectory for departure time 207

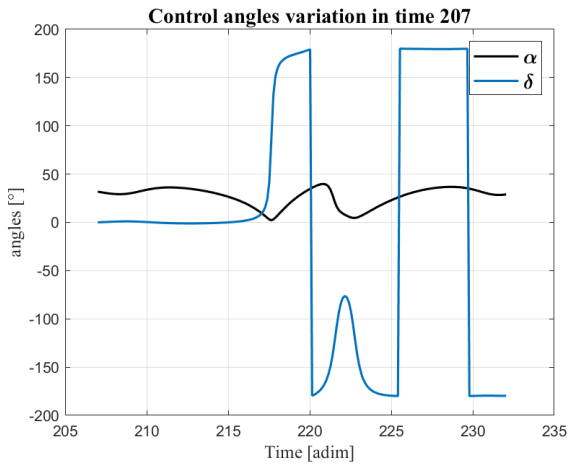

Figure 7.62: Control angles for departure time 207

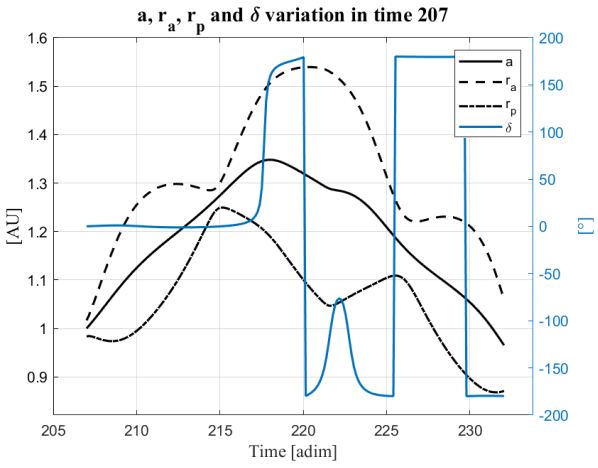

Figure 7.63: Semi-major axis, periapsis, apoapsis and δ variation in time for departure time 207

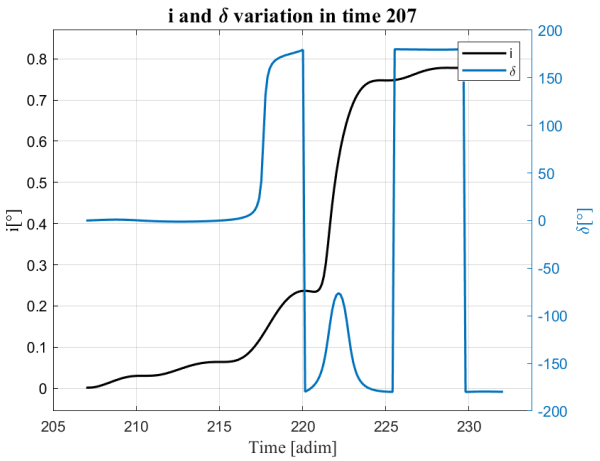

Figure 7.64: Inclination variation in time for departure time 207

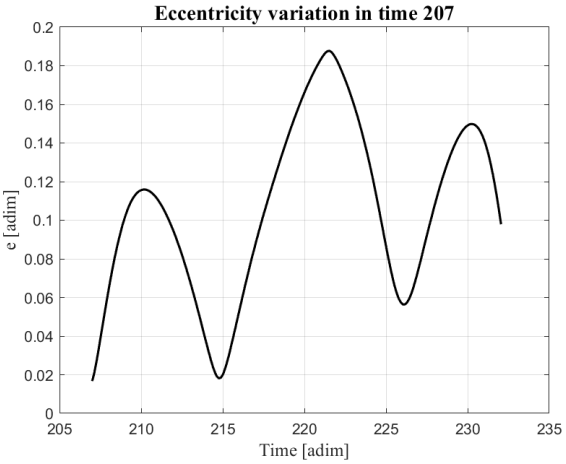

Figure 7.65: Eccentricity variation in time for departure time 207

Mission departure time 213

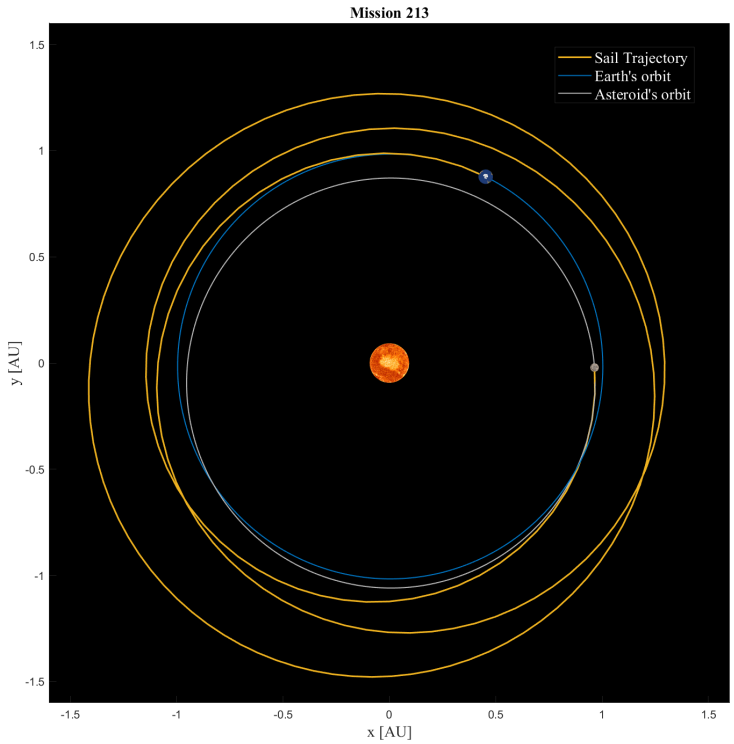

Figure 7.66: Mission trajectory for departure time 213

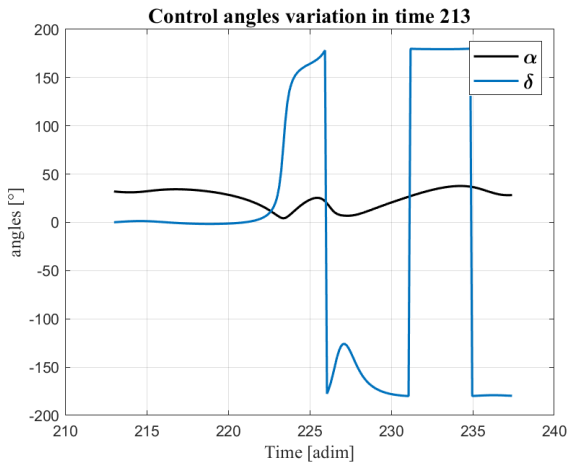

Figure 7.67: Control angles for departure time 213

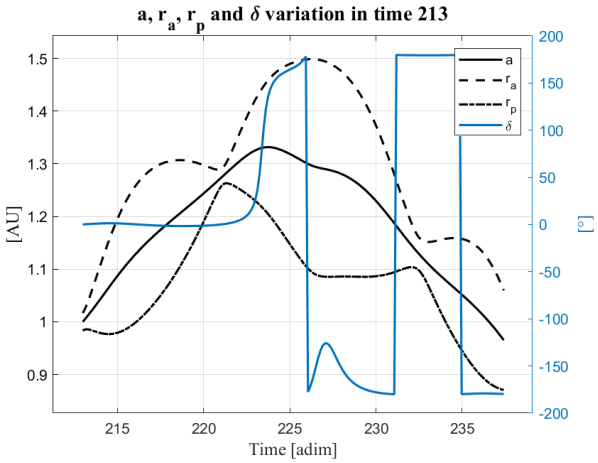

Figure 7.68: Semi-major axis, periapsis, apoapsis and δ variation in time for departure time 213

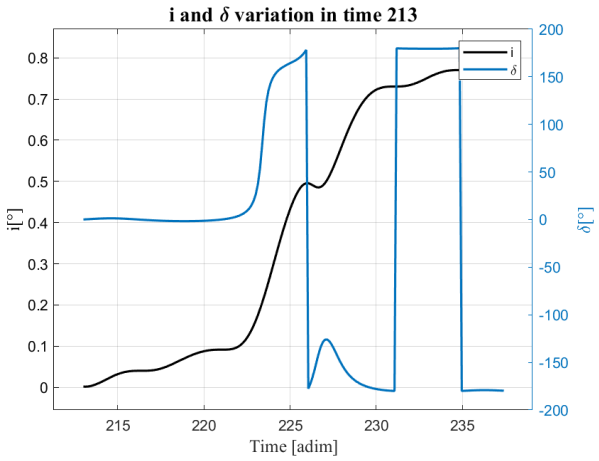

Figure 7.69: Inclination variation in time for departure time 213

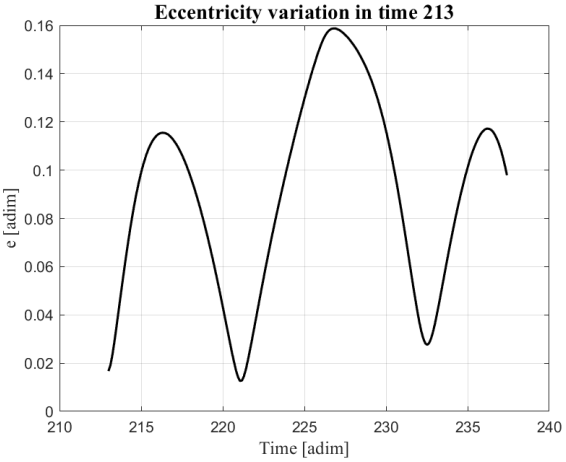

Figure 7.70: Eccentricity variation in time for departure time 213

Mission departure time 220

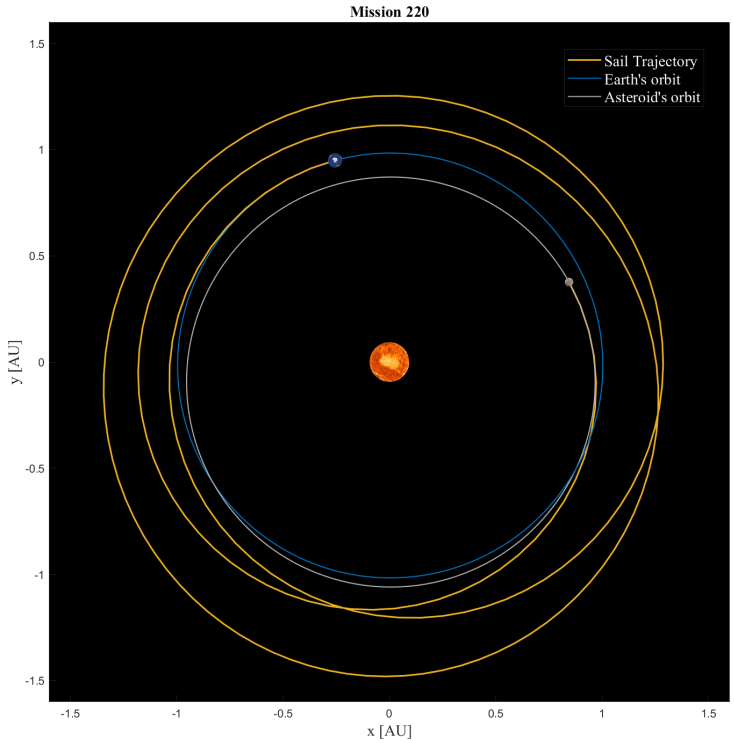

Figure 7.71: Mission trajectory for departure time 220

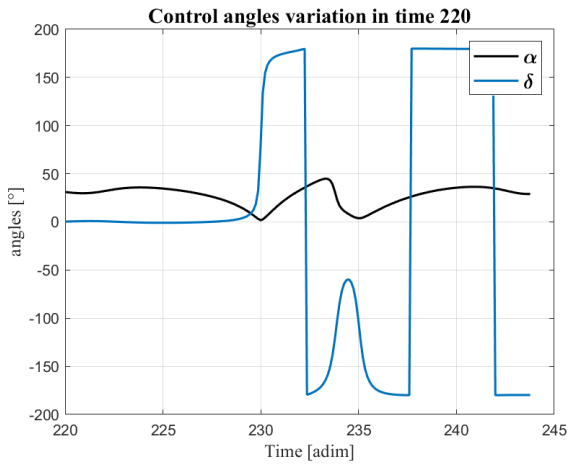

Figure 7.72: Control angles for departure time 220

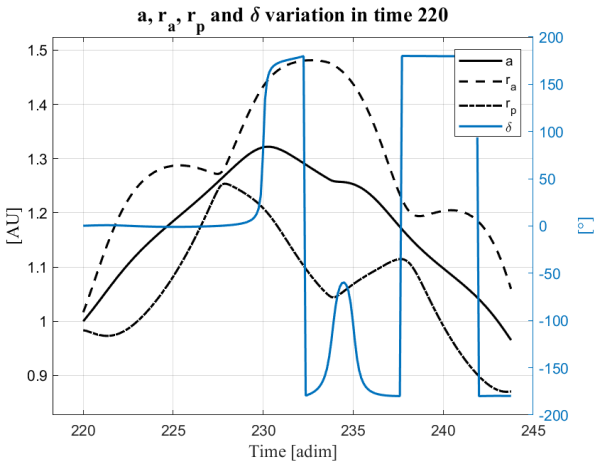

Figure 7.73: Semi-major axis, periapsis, apoapsis and δ variation in time for departure time 220

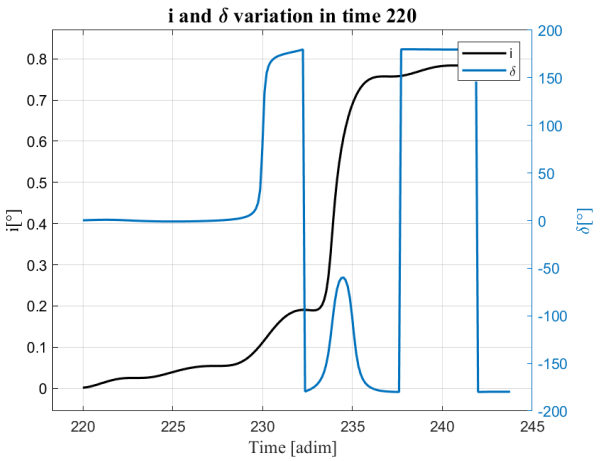

Figure 7.74: Inclination variation in time for departure time 220

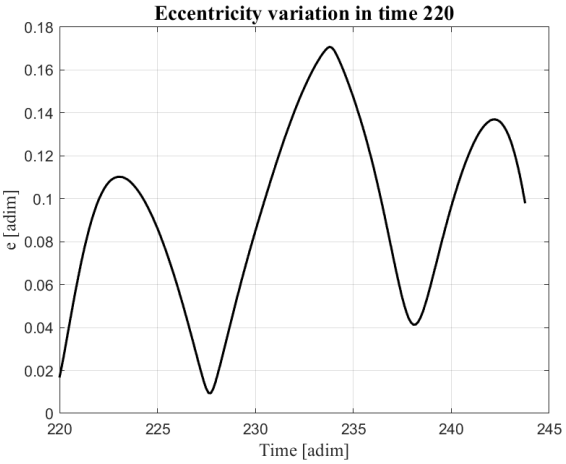

Figure 7.75: Eccentricity variation in time for departure time 220

Mission departure time 226

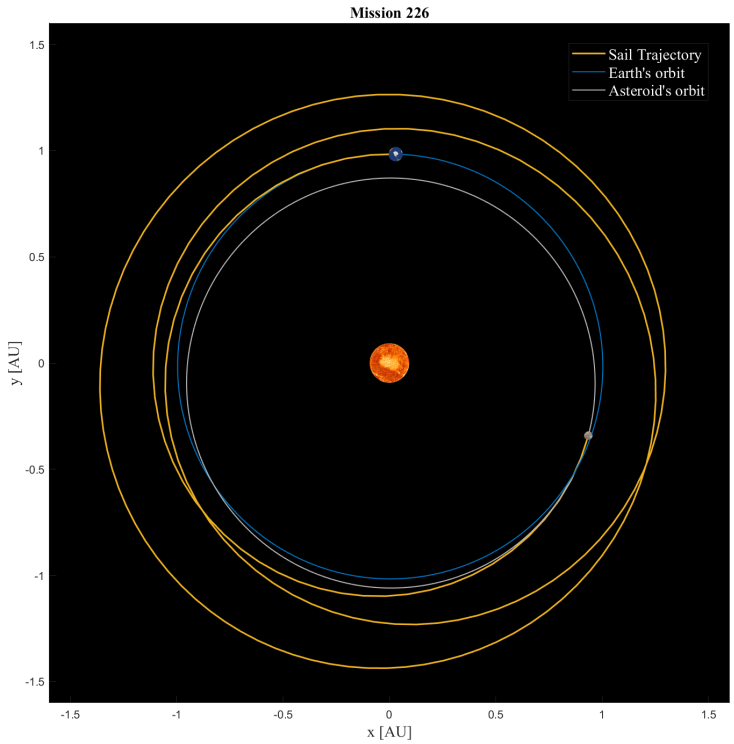

Figure 7.76: Mission trajectory for departure time 226

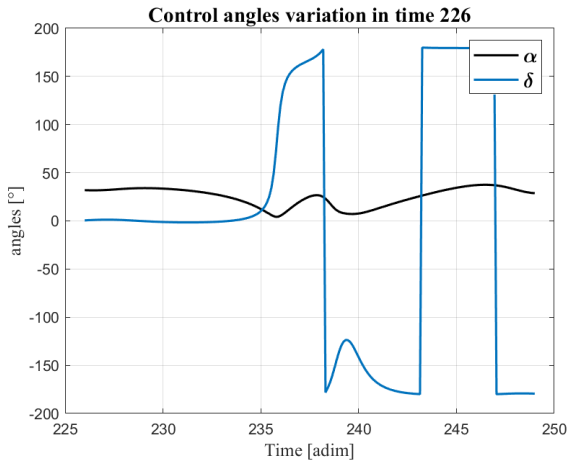

Figure 7.77: Control angles for departure time 226

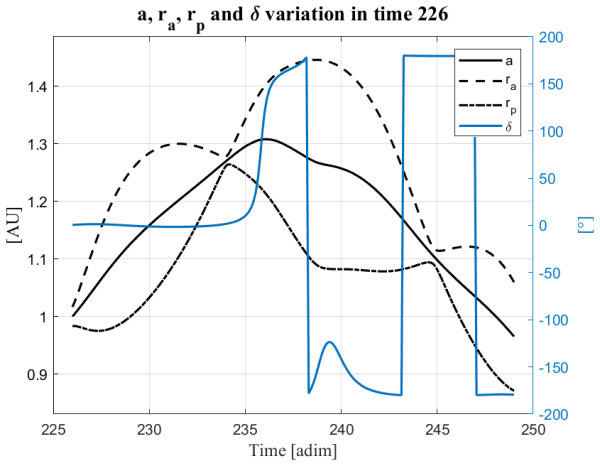

Figure 7.78: Semi-major axis, periapsis, apoapsis and δ variation in time for departure time 226

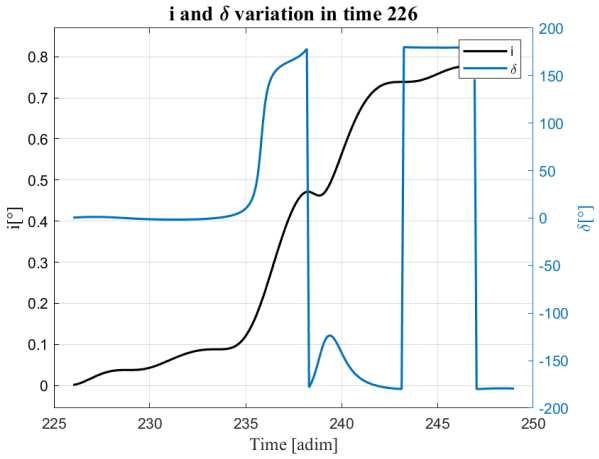

Figure 7.79: Inclination variation in time for departure time 226

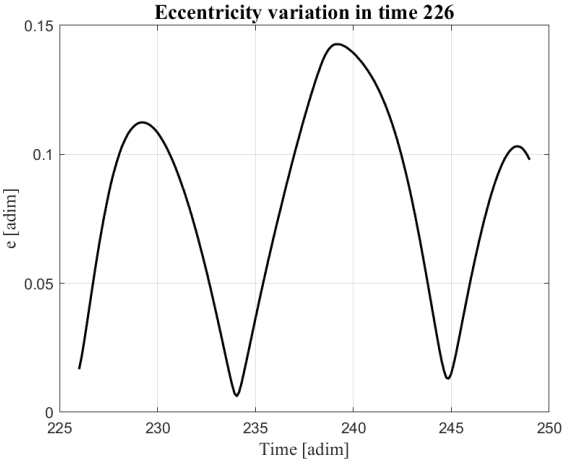

Figure 7.80: Eccentricity variation in time for departure time 226

Comment on the plots

The behaviour of the different parameters is consistent with what was observed for the other asteroids. In this case, perihelion decreases from $r_{p_\oplus} = 0,98329134\,\text{AU}$ to $r_{p_{asteroid}} = 0.8707139\,\text{AU}$ and the aphelion increases from $r_{a_\oplus} = 1,01671388\,\text{AU}$ to $r_{a_{asteroid}} = 1.0596362948\,\text{AU}$. The inclination increases from $i_\oplus = 0.001748°$ to $i_{asteroid} = 0.81270°$.

Chapter 8

Conclusions

This thesis focuses on optimizing the orbit of a solar sail-propelled spacecraft.This was achieved by applying the optimal control theory to the problem and by solving the boundary value problem, through the implementation of an indirect mathematical method. The analysis concentrated on three near-Earth asteroids 2000 SG344, 2014 QN266, and 2020 JPG. The objective of the project was to find viable trajectories for missions towards the aforementioned asteroids,that would allow for each asteroid to be reached in the minimum time. In order to accomplish this objective, a comprehensive search was conducted for each asteroid, encompassing a one-year time span between 24 November 2026 and 12 December 2036 for asteroids 2000 SG344 and 2020 PJ6, and between 10 December 2025 and 12 December 2036 for asteroid 2014 QN266. The results shown a decreasing trend in the mission duration of asteroids 2000 SG344 and 2020 PJ6, and an increasing trend for asteroid 2014 QN266. an investigation was conducted into the behaviour of the various parameters within each year, to acquire detailed information on the mission. From the considerations made on the transfer duration associated with the study-year missions, it was decided that the search for missions should be conducted over shorter intervals of time each year in the period between 3 September 2031 (199) and 12 June 2036 (299) for asteroids displaying an increasing trend, specifically 2000 SG344 and 2020 PJ6. And between 20 December 2025 and 19 September 2030 for asteroid 2014 QN266, which exhibited an increasing trend. The results of the study are as follows:

- **Asteroid 2000 SG344**: the minimum duration mission is found on departure date 17 February 2036 and the estimated trip duration is of approximately 1020 days, equivalent to almost three years;
- **Asteroid 2014 QN266**: the minimum duration is achieved by departing on 5 May 2026.The duration of the trip would be approximately 1418 or 3.88 years;
- **Asteroid 2020 PJ6**: the minimum trip time is calculated to be 1337 days, or approximately 3.66 years, with the mission scheduled to depart on 20 December 2035.

The results of the study reveal that the mission is divided into two phases in the three cases under consideration. In the initial phase, the objective is to increase the apoapsis altitude. During this phase, the clock angle is fixed at zero, and the cone angle decreases until it reaches zero, accelerating the spacecraft. In the second phase, the objective is to lower the periapsis. The clock angle would be equal to $\pm 180^{\circ}$ and the cone angle would increase, decelerating the sail. The change of inclination manoeuvre is performed when the clock angle is approximately equal to 90°, near the point of periapsis, where the cost of the plane change in terms of thrust required is minimised.

The duration of the mission was found to be dependent on the phase angle between the departure and arrival bodies. This angle would determine the rate at which the spacecraft should orbit in order correct relative position with the asteroid to complete the rendezvous. This would determine the length and duration of the transfer. The results obtained demonstrated a sinusoidal trend, indicating that for each year there is a minimum corresponding to the departure date that guarantees the shortest trip time.

Achieving superior results with regard to mission durations is possible through the variation of sail parameters. It has been demonstrated that an increase in the characteristic acceleration of the sail results in a decrease in transfer duration. Conversely, a decrease in the parameter η leads to an increase in transfer duration.
It is evident that the sail characteristics are significantly constrained by the design parameters. Programming the mission's departure time,with the objective of ensuring optimal phasing is essential to perform a successful mission, in a convenient interval of time.

In consideration of the results obtained, it can be concluded that the objective of identifying feasible trajectories for an interplanetary transfer departing from Earth and arriving at a near-Earth asteroid, considering solar sailing as the propulsion system for the spacecraft, has been accomplished.

Further development of the project would involve incorporating perturbations, such third bodies gravitational influence, into the model. This will enable the attainment of a more precise solution. Moreover, the analysis could be expanded to encompass other near-Earth asteroids. This extension would result in the acquisition of a more precise and comprehensive depiction of the dynamics of the transfer.

Appendix A

Non-dimensionalisation of acceleration

By substituting the normal [Equation 5.8] and tangential [Equation 5.9] pressure expressions into Equation 5.21, the following expression is obtained:

$$a_u = \frac{A}{m}\cos(\alpha)\omega p[((1+\eta)\cos(\alpha)+\delta_{rad})\cos(\alpha)+(1-\eta)\sin^2(\alpha)] \tag{A.1}$$

By expanding the terms and substituting the definition of the characteristic acceleration, provided in Equation 5.20, into its dimensionless form, the following equation is obtained:

$$a_u = \omega\frac{a_c}{2r^2}\cos(\alpha)\omega[\cos^2(\alpha)+\sin^2(\alpha)+\delta_{rad}cos(\alpha)+\eta(\cos^2(\alpha)-\sin^2(\alpha))] \tag{A.2}$$

By applying the fundamental trigonometric identity $\cos^2(x)+\sin^2(x)=1$ and the double angle formula $\cos^2(x)-\sin^2(x)=\cos(2x)$, Equation A.2 simplifies to:

$$a_u = \omega\frac{a_c}{2r^2}\cos(\alpha)[1+\eta\cos(2\alpha)+\delta_{rad}cos(\alpha)] \tag{A.3}$$

A similar procedure is applied to Equation A.2. By substituting the expressions for p_n and p_t, a new expression for a_v is obtained:

$$a_v = \frac{A}{m}\cos(\alpha)\cos(\delta)\omega p[((1+\eta)\cos(\alpha)+\delta_{rad})\sin(\alpha)-(1-\eta)\sin(\alpha)\cos(\alpha)] \tag{A.4}$$

After expanding the terms and substituting the definition of the characteristic acceleration, the new expression is:

$$a_v = \omega\frac{a_c}{2r^2}\cos(\alpha)\cos(\delta)[2\eta\cos(\alpha)\sin(\alpha)+\delta_{rad}\sin(\alpha)] \tag{A.5}$$

By using the he double-angle identity for sin $2\sin(x)\cos(x)=\sin(2x)$, the expression becomes:

$$a_v = \omega\frac{a_c}{2r^2}\cos(\alpha)\cos(\delta)[\eta\sin(2\alpha)+\delta_{rad}\sin(\alpha)] \tag{A.6}$$

An analogous expression is obtained for a_w, starting from Equation 5.23:

$$a_w = \omega\frac{a_c}{2r^2}\cos(\alpha)\sin(\delta)[\eta\sin(2\alpha)+\delta_{rad}\sin(\alpha)] \tag{A.7}$$

Appendix B

Control law

To determine the maximum value of H' with respect to δ, its first derivative is computed and set equal to zero:

$$\frac{\partial H'}{\partial \delta} = \cos(\alpha)[-\sin(\delta)\sin(\beta)\cos(\gamma)\eta\sin(2\alpha) + \cos(\delta)\sin(\beta)\sin(\gamma)\eta\sin(2\alpha)] = 0 \quad \text{(B.1)}$$

The result of this procedure is given by:

$$\cos(\delta)\sin(\gamma) - \sin(\delta)\cos(\gamma) = 0 \quad \text{(B.2)}$$

By applying the sine difference identity, $\sin(x-y) = \sin(x)\cos(y) - \sin(y)\cos(x)$, the equation can be rewritten in the following form:

$$\cos(\delta)\sin(\gamma) - \sin(\delta)\cos(\gamma) = \sin(\delta - \gamma) = 0 \quad \text{(B.3)}$$

From Equation B.3, the following expression is obtained:

$$\delta = \gamma \quad \text{(B.4)}$$

By substituting the angle γ with δ, Equation 5.66 can be rewritten as:

$$\begin{aligned} H' = \cos(\alpha)[\cos(\beta)(1 + \eta\cos(2\alpha)) + \eta\cos^2(\delta)\sin(\beta)\sin(2\alpha) + \\ + \eta\sin^2(\delta)\sin(\beta)\sin(2\alpha)] \end{aligned} \quad \text{(B.5)}$$

By collecting and rearranging the terms, the following expression is obtained:

$$H' = \cos(\alpha)[\cos(\beta) + \eta[\cos(\beta)\cos(2\alpha) + sin(\beta)sin(2\alpha)]] \quad \text{(B.6)}$$

By applying the cosine difference identity, $\cos(x - y) = \cos(x)\cos(y) + \sin(x)\sin(y)$, the equation can be rewritten as:

$$H' = \cos(\alpha)[\cos(\beta) + \eta\cos(\beta - 2\alpha)] \quad \text{(B.7)}$$

To find the local maximum with respect to α, the first derivative of H' is computed and set equal to zero, as previously done for δ:

$$\frac{\partial H'}{\partial \alpha} = -\sin(\alpha)\cos(\beta) + \eta[-\sin(\alpha)\cos(\beta - 2\alpha) + 2\cos(\alpha)\sin(\beta - 2\alpha)] = 0 \quad \text{(B.8)}$$

By rearranging the terms, the following expression is obtained:

$$-\sin(\alpha)\cos(\beta) - \eta\sin(\alpha)\cos(\beta - 2\alpha) + 2\eta\cos(\alpha)\sin(\beta - 2\alpha) = 0 \tag{B.9}$$

With reference to Equation B.9, it is observed that:

$$\sin(\beta - \alpha) = \sin[\alpha + (\beta - 2\alpha)] = \cos(\alpha)\sin(\beta - 2\alpha) + \sin(\alpha)\cos(beta - 2\alpha) \tag{B.10}$$

Thus, the following expression is obtained:

$$-\sin(\alpha)\cos(\beta - 2\alpha) = \cos(\alpha)\sin(\beta - 2\alpha) - \cos(\alpha)\sin(\beta) + \sin(\alpha)\cos(\beta) \tag{B.11}$$

By substituting Equation B.10 into Equation B.9, the following expression is obtained:

$$\begin{aligned} &-\sin(\alpha)\cos(\beta) + \eta\cos(\alpha)\sin(\beta - 2\alpha) - \eta\cos(\alpha)\sin(\beta) + \eta\sin(\alpha)\cos(\beta) + \\ &+ 2\eta\cos(\alpha)\sin(\beta - 2\alpha) = 0 \end{aligned} \tag{B.12}$$

By rearranging the terms and isolating the term $\sin(\beta - 2\alpha)$, the expression becomes:

$$\sin(\beta - 2\alpha) = \frac{\frac{1-\eta}{\eta}\cos(\beta)\sin(\alpha) + sin(\beta)\cos(\alpha)}{3\cos(\alpha)} \tag{B.13}$$

By removing $\cos(\alpha)$, the term $\sin(\beta - 2\alpha)$ is obtained:

$$\sin(\beta - 2\alpha) = \frac{\frac{1-\eta}{\eta}\cos(\beta)\tan(\alpha) + sin(\beta)}{3} \tag{B.14}$$

Appendix C

Additional Numerical results

C.1 Effect of the variation of the parameter η on the solution, departure time 169

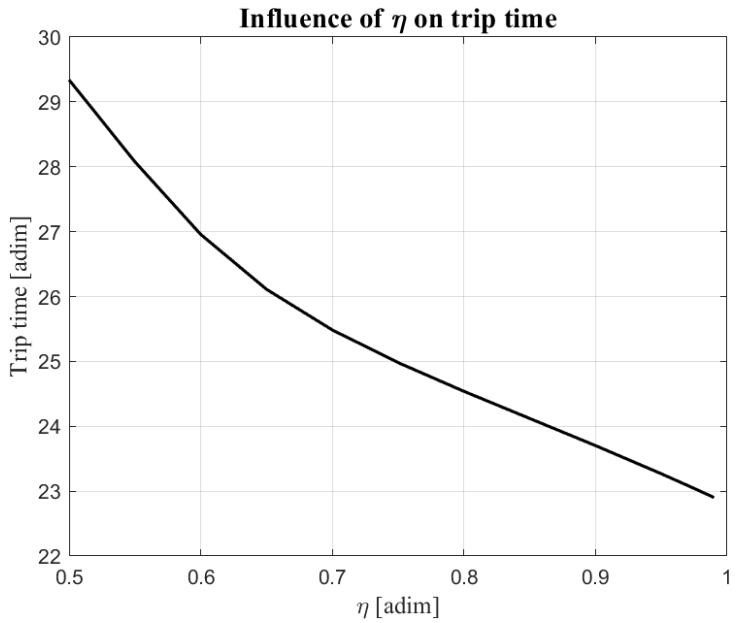

Figure C.1: Effect of η on trip time

Table C.1: Numerical result for $\eta = 0.5 \div 1$

Departure time [adim]	**acc**	η	**Trip time [adim]**	**Trip time [days]**	θ_0 $[rad]$	$\Delta\theta$ $[rad]$
169	0.05	0.99	22.9017109743872	1331.33235897274	1.0766	16.9509
169	0.05	0.98	22.9950028097691	1336.75564107646	1.0766	17.0370
169	0.05	0.97	23.0870870182937	1342.10872088331	1.0766	17.1225
169	0.05	0.95	23.2677513713972	1352.61118070688	1.0766	17.2920
169	0.05	0.90	23.7018175941400	1377.84450973286	1.0766	17.7122
169	0.05	0.85	24.1200594997935	1402.15793258138	1.0766	18.1393
169	0.05	0.80	24.5387086335884	1426.49502859575	1.0766	18.5922
169	0.05	0.75	24.9812131587557	1452.21889673844	1.0766	19.0966
169	0.05	0.70	25.4844899409809	1481.47560452091	1.0766	19.6901
169	0.05	0.65	26.1113561823045	1517.91686922620	1.0766	20.4238
169	0.05	0.60	26.9574017322272	1567.09956212790	1.0766	21.3421
169	0.05	0.55	28.0771825906619	1632.19515666491	1.0766	22.4179
169	0.05	0.50	29.3398230044369	1705.59552585503	1.0766	23.5755

C.2 Effect of the variation of the parameter a_c on the solution, departure time 169

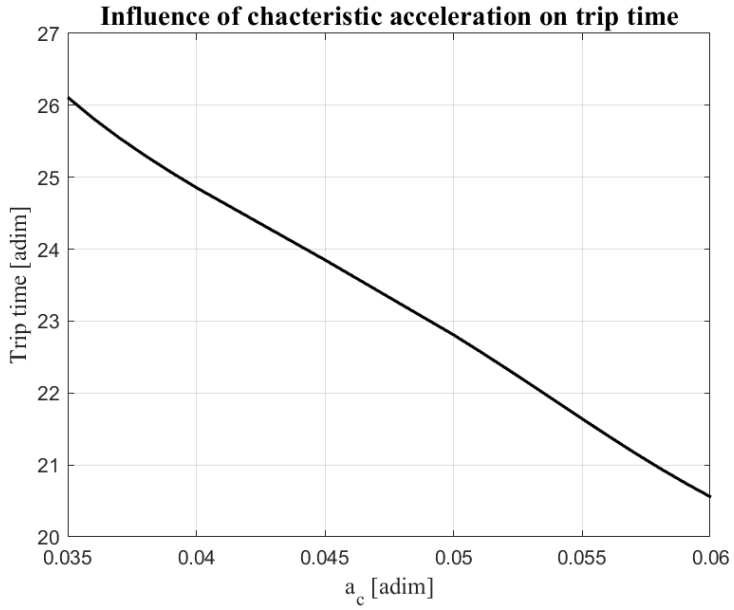

Figure C.2: Effect of a_c on trip time

Table C.2: Effect of varying characteristic acceleration on the solution, with fixed departure time and η

Departure time [adim]	**acc**	η	**Trip time [adim]**	**Trip time [days]**	θ_0 $[rad]$	$\Delta\theta$ $[rad]$
169	0.060	1	20.5517705332677	1194.72458523828	1.0766	14.7089
169	0.059	1	20.7478868651688	1206.12530630559	1.0766	14.9165
169	0.058	1	20.9562255138165	1218.23654047842	1.0766	15.1309
169	0.057	1	21.1757951763861	1231.00066090394	1.0766	15.3505
169	0.056	1	21.4046105024562	1244.30225431619	1.0766	15.5730
169	0.055	1	21.6398280818792	1257.97602634289	1.0766	15.7962
169	0.054	1	21.8781440836306	1271.82991722237	1.0766	16.0178
169	0.053	1	22.1163282724548	1285.67614549466	1.0766	16.2361
169	0.052	1	22.3516899257354	1299.35829288637	1.0766	16.4500
169	0.051	1	22.5823350905073	1312.76625928874	1.0766	16.6593
169	0.050	1	22.8071970260806	1325.83803246170	1.0766	16.8642
169	0.045	1	23.8494596700650	1386.42730398106	1.0766	17.8602
169	0.040	1	24.8557289169822	1444.92419147380	1.0766	18.9513
169	0.039	1	25.0730234661742	1457.55605400543	1.0766	19.2039
169	0.038	1	25.3025281359949	1470.89772065250	1.0766	19.4744
169	0.037	1	25.5484780420820	1485.19538902436	1.0766	19.7659
169	0.036	1	25.8160507526630	1500.75004379984	1.0766	20.0816
169	0.035	1	26.1114180945134	1517.92046833402	1.0766	20.4239

Bibliography

[1] William Andrew Hollerman. “The physics of solar sails”. In: *The 2002 NASA Faculty Fellowship Program Research Reports* (2003).

[2] L. S. Varanini. “LA “DISSERTATIO CUM NUNCIO SIDEREO” FRA GALILEO E BRUNO”. In: *Bruniana & Campanelliana* 9.1 (2003), pp. 207–215. URL: http://www.jstor.org/stable/24333113.

[3] Planetary Society. *The Story of LightSail, Part 1*. 2024. URL: https://www.planetary.org/sci-tech/the-story-of-lightsail-part-1.

[4] F. A. Tsander. *From a Scientific Heritage*. Trans. by Unknown. NASA TT F-541. Washington, DC: National Aeronautics and Space Administration, 1969, pp. 1–92.

[5] Arthur C. Clarke. “The Wind From the Sun”. In: *Project Solar Sail*. Ed. by Arthur C. Clarke. New York, NY: Penguin Books, 1990, pp. 9–31.

[6] Les Johnson. *Solar sail propulsion for interplanetary small spacecraft*. Tech. rep. 2018.

[7] NASA. *Chapter 6-3: The Mariner Mars 71 Project*. https://solarviews.com/history/SP-4212/ch6-3.html. Accessed: 2025-05-18. 1984.

[8] Kaushik Patowary. *The Znamya Space Mirror*. Accessed: 2025-05-20. Feb. 2020. URL: https://www.amusingplanet.com/2020/02/the-znamya-space-mirror.html.

[9] Les Johnson et al. “Status of solar sail technology within NASA”. In: *Advances in Space Research* 48.11 (2011), pp. 1687–1694.

[10] Les Johnson, Roy M. Young, and Edward E. Montgomery IV. “Recent advances in solar sail propulsion systems at NASA”. In: *Acta Astronautica* 61.1 (2007). Bringing Space Closer to People, Selected Proceedings of the 57th IAF Congress, Valencia, Spain, 2-6 October, 2006, pp. 376–382. ISSN: 0094-5765. DOI: https://doi.org/10.1016/j.actaastro.2007.01.047. URL: https://www.sciencedirect.com/science/article/pii/S0094576507000574.

[11] Institute of Space and Astronautical Science (ISAS). *ISAS Deployed Solar Sail Film in Space*. Accessed: 2025-05-20. Aug. 2004. URL: https://www.isas.jaxa.jp/e/snews/2004/0809.shtml.

[12] Phys.org. *A History of Solar Sailing*. 2008. URL: https://phys.org/news/2008-08-history-solar.html.

[13] The Planetary Society. *Cosmos 1 Spacecraft*. Accessed: 2025-05-20. 2025. URL: https://www.planetary.org/space-images/cosmos-1-spacecraft.

[14] The Planetary Society. *LightSail 2 completes mission*. 2022. URL: https://www.planetary.org/articles/lightsail-2-completes-mission.

[15] Hirotaka Sawada et al. “Mission report on the solar power sail deployment demonstration of IKAROS”. In: *52nd AIAA/ASME/ASCE/AHS/ASC Structures, Structural Dynamics and Materials Conference 19th AIAA/ASME/AHS Adaptive Structures Conference 13t*. 2011, p. 1887.

[16] Dean Alhorn et al. “Nanosail-d: The small satellite that could!” In: (2011).

[17] NASA. *NEA Scout - NASA Science*. Pagina ufficiale della missione NEA Scout. NASA. 2022. URL: https://science.nasa.gov/mission/nea-scout/ (visited on 05/21/2025).

[18] The Planetary Society. *NEA Scout*. 2025. URL: https://www.planetary.org/space-missions/nea-scout.

[19] Keats Wilkie. “The NASA advanced composite solar sail system (ACS3) flight demonstration: A technology pathfinder for practical smallsat solar sailing”. In: (2021).

[20] Erik Pranckh. *Focusing on Large Spacecraft to Carry Out Exploration Plans*. Articolo della rubrica ”Year in Review”. Dec. 1, 2021. URL: https://aerospaceamerica.aiaa.org/year-in-review/focusing-on-large-spacecraft-to-carry-out-exploration-plans/ (visited on 05/21/2025).

[21] Robert Miller. *The Different Types of Solar Sail Designs*. Progetto del corso PHYS 212, primavera 2015. University of Alaska Fairbanks, Department of Physics. 2015. URL: https://ffden-2.phys.uaf.edu/webproj/212_spring_2015/robert_miller/phone/types.html (visited on 05/21/2025).

[22] Bo Fu, Evan Sperber, and Fidelis Eke. “Solar sail technology—A state of the art review”. In: *Progress in Aerospace Sciences* 86 (2016), pp. 1–19.

[23] Robert Miller. *Types of Spacecraft Propulsion*. 2015. URL: https://ffden-2.phys.uaf.edu/webproj/212_spring_2015/Robert_Miller/phone/types.html.

[24] Pengyuan ZHAO, Chenchen WU, and Yangmin LI. “Design and application of solar sailing: A review on key technologies”. In: *Chinese Journal of Aeronautics* 36.5 (2023), pp. 125–144. ISSN: 1000-9361. DOI: https://doi.org/10.1016/j.cja.2022.11.002. URL: https://www.sciencedirect.com/science/article/pii/S1000936122002564.

[25] Colin R McInnes. “Solar sail mission applications for non-Keplerian orbits”. In: *Acta Astronautica* 45.4 (1999). Third IAA International Conference on Low-Cost Planetary Missions, pp. 567–575. ISSN: 0094-5765. DOI: https://doi.org/10.1016/S0094-5765(99)00177-0. URL: https://www.sciencedirect.com/science/article/pii/S0094576599001770.

[26] Roy Young. “Updated heliostorm warning mission: enhancements based on new technology”. In: *48th AIAA/ASME/ASCE/AHS/ASC Structures, Structural Dynamics, and Materials Conference*. 2007, p. 2249.

[27] Guglielmo S Aglietti et al. “RemoveDEBRIS: An in-orbit demonstration of technologies for the removal of space debris”. In: *The Aeronautical Journal* 124.1271 (2020), pp. 1–23.

[28] PengYuan Zhao, JinGuo Liu, and ChenChen Wu. “Survey on research and development of on-orbit active debris removal methods”. In: *Science China Technological Sciences* 63.11 (2020), pp. 2188–2210.

[29] Matteo Ceriotti and Colin R. McInnes. “Systems design of a hybrid sail pole-sitter”. In: *Advances in Space Research* 48.11 (2011). SOLAR SAILING: CONCEPTS, TECHNOLOGY, AND MISSIONS, pp. 1754–1762. ISSN: 0273-1177. DOI: https://doi.org/10.1016/j.asr.2011.02.010. URL: https://www.sciencedirect.com/science/article/pii/S0273117711001384.

[30] Les Johnson et al. “Multiple NEO rendezvous using solar sail propulsion”. In: *Global Space Exploration Conference*. M12-1796. 2012.

[31] Les Johnson. *Solar sail propulsion*. Tech. rep. 2011.

[32] Malcolm Macdonald, Colin R McInnes, and Bernd Dachwald. “Heliocentric solar sail orbit transfers with locally optimal control laws”. In: *Journal of Spacecraft and Rockets* 44.1 (2007), pp. 273–276.

[33] NASA. *What Are SmallSats and CubeSats?* 2024. URL: https://www.nasa.gov/what-are-smallsats-and-cubesats/.

[34] B. Carry. “Density of asteroids”. In: *Planetary and Space Science* 73.1 (2012). Solar System science before and after Gaia, pp. 98–118. ISSN: 0032-0633. DOI: https://doi.org/10.1016/j.pss.2012.03.009. URL: https://www.sciencedirect.com/science/article/pii/S0032063312000773.

[35] European Space Agency. *Small objects in the Solar System*. Accessed: 2025-05-18. European Space Agency. Nov. 2023. URL: https://www.esa.int/ESA_Multimedia/Images/2023/11/Small_objects_in_the_Solar_System.

[36] NASA. *Asteroid Facts*. NASA Science – Solar System Exploration. 2024. URL: https://science.nasa.gov/solar-system/asteroids/facts/.

[37] NASA. *Asteroid Belts (Illustration)*. Accessed: 2025-05-20. NASA/ESA/CSA. Nov. 2020. URL: https://webbtelescope.org/contents/media/images/2020/25/4663-Image.

[38] Encyclopædia Britannica. *Geography of the Asteroid Belt*. Encyclopædia Britannica, Inc. 2024. URL: https://www.britannica.com/science/asteroid/Geography-of-the-asteroid-belt.

[39] NASA Center for Near Earth Object Studies. *Near-Earth Object Groups*. Accessed on 2025-04-18. Jet Propulsion Laboratory, California Institute of Technology. 2024. URL: https://cneos.jpl.nasa.gov/about/neo_groups.html.

[40] NASA. *NASA’s OSIRIS-REx Spacecraft Arrives at Asteroid Bennu*. Accessed: 2025-05-20. NASA. Dec. 2018. URL: https://www.nasa.gov/news-release/nasas-osiris-rex-spacecraft-arrives-at-asteroid-bennu/.

[41] Wikipedia contributors. *433 Eros*. Accessed: 2025-05-20. 2025. URL: https://en.wikipedia.org/wiki/433_Eros.

[42] NASA. *Asteroid Psyche*. Accessed: 2025-05-20. NASA Science. 2023. URL: https://science.nasa.gov/solar-system/asteroids/16-psyche/.

[43] Encyclopædia Britannica. *Physical Characteristics of Asteroids*. Encyclopædia Britannica, Inc. 2024. URL: https://www.britannica.com/science/asteroid/Physical-characteristics-of-asteroids.

[44] The Planetary Society. *What Are Asteroids Made Of?* The Planetary Society. 2024. URL: https://www.planetary.org/articles/what-are-asteroids-made-of.

[45] M. Azadmanesh, J. Roshanian, and M. Hassanalian. “On the importance of studying asteroids: A comprehensive review”. In: *Progress in Aerospace Sciences* 142 (2023), p. 100957. ISSN: 0376-0421. DOI: https://doi.org/10.1016/j.paerosci.2023.100957. URL: https://www.sciencedirect.com/science/article/pii/S0376042123000738.

[46] Charles F Hall. “Pioneer 10”. In: *Science* 183.4122 (1974), pp. 301–302.

[47] J. Veverka et al. “Galileo’s Encounter with 951 Gaspra: Overview”. In: *Icarus* 107.1 (1994), pp. 2–17. ISSN: 0019-1035. DOI: https://doi.org/10.1006/icar.1994.1002. URL: https://www.sciencedirect.com/science/article/pii/S0019103584710025.

[48] Michael J.S. Belton et al. “Galileo’s Encounter with 243 Ida: An Overview of the Imaging Experiment”. In: *Icarus* 120.1 (1996), pp. 1–19. ISSN: 0019-1035. DOI: https://doi.org/10.1006/icar.1996.0032. URL: https://www.sciencedirect.com/science/article/pii/S0019103596900329.

[49] J Veverka et al. “NEAR’s flyby of 253 Mathilde: Images of a C asteroid”. In: *Science* 278.5346 (1997), pp. 2109–2114.

[50] L. Prockter et al. “The NEAR shoemaker mission to asteroid 433 eros”. In: *Acta Astronautica* 51.1 (2002), pp. 491–500. ISSN: 0094-5765. DOI: https://doi.org/10.1016/S0094-5765(02)00098-X. URL: https://www.sciencedirect.com/science/article/pii/S009457650200098X.

[51] LA Soderblom et al. “Deep Space 1 MICAS observations of 9969 Braille.” In: *Bulletin of the Astronomical Society, Vol. 31, No. 4, p. 1127, id. 34.03*. Vol. 31. 1999, p. 1127.

[52] Earle K Huckins et al. “CASSINI-HUYGENS MISSION”. In: *Science and Scientists* 1 (2006), p. 136.

[53] Donald E Brownlee et al. “Stardust: Comet and interstellar dust sample return mission”. In: *Journal of Geophysical Research: Planets* 108.E10 (2003).

[54] Makoto Yoshikawa et al. “Chapter 6 - The Hayabusa mission”. In: *Sample Return Missions*. Ed. by Andrea Longobardo. Elsevier, 2021, pp. 123–146. ISBN: 978-0-12-818330-4. DOI: https://doi.org/10.1016/B978-0-12-818330-4.00006-9. URL: https://www.sciencedirect.com/science/article/pii/B9780128183304000069.

[55] NASA. *New Horizons*. Accessed: 2025-05-20. NASA Science. 2025. URL: https://science.nasa.gov/mission/new-horizons/.

[56] R Schulz, M Küppers, and K Wirth. “The Rosetta Encounters with (2867) Steins and (21) Lutetia-An Overview”. In: *AGU Fall Meeting Abstracts*. Vol. 2010. 2010, P14B–01.

[57] CT Russell and CA Raymond. *The Dawn Mission to Minor Planets 4 Vesta and 1 Ceres Foreword*. 2011.

[58] Sei-ichiro Watanabe et al. “Hayabusa2 mission overview”. In: *Space Science Reviews* 208 (2017), pp. 3–16.

[59] DS Lauretta et al. “OSIRIS-REx: sample return from asteroid (101955) Bennu”. In: *Space Science Reviews* 212 (2017), pp. 925–984.

[60] Harold F Levison et al. “NASA’s Lucy mission to the Trojan asteroids”. In: *2021 IEEE Aerospace Conference (50100)*. IEEE. 2021, pp. 1–10.

[61] Harrison F Agrusa et al. “The excited spin state of Dimorphos resulting from the DART impact”. In: *Icarus* 370 (2021), p. 114624.

[62] Elisabetta Dotto et al. “LICIACube-the Light Italian Cubesat for Imaging of Asteroids in support of the NASA DART mission towards asteroid (65803) Didymos”. In: *Planetary and Space Science* 199 (2021), p. 105185.

[63] NASA Jet Propulsion Laboratory. *Eyes on Asteroids*. Accessed: 2025-05-20. NASA Jet Propulsion Laboratory. 2021. URL: https://eyes.nasa.gov/apps/asteroids/#/home.

[64] James Phillip McDanell and William Francis Powers. “Necessary conditions joining optimal singular and nonsingular subarcs”. In: *SIAM Journal on Control* 9.2 (1971), pp. 161–173.

[65] Lawrence F Shampine. “Computer solution of ordinary differential equations”. In: *The initial value problem* (1975).

[66] Lorenzo Casalino. “Ottimizzazione indiretta di traiettorie spaziali”. In: *Appunti concessi per elaborato* ().

[67] R. L. Forward. “Grey Solar Sails”. In: *The Journal of the Astronautical Sciences* 38.2 (1990), pp. 161–185.